Large scale water balance estimation from downscaled atmospheric moisture budgets and evaluation with global climatological data sets and the GRACE spaceborne gravimetry

Dissertation
zur Erlangung des Doktorgrades an der
Fakultät für Angewandte Informatik
der Universität Augsburg

vorgelegt von

Benjamin Fersch

Diplom Hydrologe

2011

Erstes Gutachten: Prof. Dr. Harald Kunstmann
Zweites Gutachten: Prof. Dr. András Bárdossy
Weiteres Gutachten: Prof. Dr. Jucundus Jacobeit

Tag der mündlichen Prüfung: 02.12.2011

Acknowledgment

This work would not have been possible without the support of various people.

First of all, my thanks go to Prof. Harald Kunstmann for proposing the topic, for his excellent supervision and all the suggestions that helped me finding an appropriate way.

My gratefulness to Prof. András Bárdossy, who provided many precious conceptions for the success of this work.

Thank you Prof. Nico Sneeuw for the sophisticated remarks on my work and for the nice cooperation within the research project.

I sincerely thank Prof. Hans-Peter Schmid for providing me the opportunity to work at the *KIT Institute of Meteorology and Climate Research* (IMK-IFU).

This work was funded by the *German Research Foundation* (DFG) as part of the project *Direct Water Balance* (DWB) that contributes to the Special Priority Program *Mass Transport and Mass Distribution in the System Earth* (SPP1257).

My credits go to all DWB project members of GIS and IWS Uni Stuttgart for their nice cooperation: Balaji Devaraju, Henry Kindt, Mohammad Tourian, and Johannes Riegger.

I'm very obliged to my colleagues, especially to Sven Wagner, Hans-Richard Knoche, Andreas Heckl, and Andreas Marx, for the fruitful discussions about dynamic downscaling and particularly the regional atmospheric model WRF, but also Johannes Werhahn and Edwin Haas for the administration of the high performance computing system at IMK-IFU and their sophisticated support for all the computational pitfalls.

Furthermore, I would like to thank Gianpaolo Balsamo and Pedro Viterbo from ECMWF for providing the atmospheric moisture flux fields for ERA-40, ERA-INTERIM, and the Operational Analysis.

I feel obliged to the Profs. Harald Kunstmann, András Bárdossy, Jucundus Jacobeit, and Karl-Friedrich Wetzel with respect to the review and defense of my thesis.

Last but not least, I thank my wife Enikő for her patience and motivation and also my parents and brothers for their continuous support.

Contents

List of Figures

List of Tables

List of Abbreviations and Symbols

Abbrevations and Acronyms

BMJ	Betts-Miller-Janjić cumulus scheme of WRF
CNES	Centre National d'Études Spatiales. French government space agency
CRUT	CRUTEM3
CRUTEM3	Gridded time series of air temperature, University of East Anglia
CSR	Center for Space Research, University of Texas at Austin
DELT	Gridded time series of air temperature, University of Delaware
DWD	National Meteorological Service of Germany
ECMWF	European Centre for Medium-Range Weather Forecasts, Reading, UK
EI	Regionally downscaled ERA-INTERIM reanalysis
EIGEN	European Improved Gravity model of the Earth by New techniques
ERA	ECMWF Reanalysis
FDDA	Four Dimensional Data Assimilation. Gridded nudging option for WRF
FES	Finite Element Solution – Global Tide (CNES, France)
GFZ	German Research Centre for Geosciences, Potsdam
GPS	Global Positioning System
GRACE	Gravity Recovery And Climate Experiment
IERS	International Earth Rotation an Reference Systems Service
IFS	Integrated forecast system of the ECMWF
JPL	Jet Propulsion Laboratory, Pasadena, California
KF	Kain-Fritsch cumulus scheme of WRF
LIDAR	Light detection and ranging. Detection of atmospheric parameters by Laser
MPI	Message Passing Interface. Parallel computation standard.

MVAPICH	Implementation of MPI for INFINIBAND networks.
NCAR	National Center for Atmospheric Research, Boulder, Colorado
NCEP	National Center for Environmental Prediction, Washington, D.C.
NCEP2	NCEP-DOE AMIP-II Reanalysis
NNRP	NCAR/NCEP Reanalysis Project
Noah-LSM	Noah Land Surface Model
NR	Regionally downscaled NCAR/NCEP reanalysis
NSA	Network Scaling Algorithm
NWP	Numerical weather prediction
OMCT	Ocean Model for Circulation an Tides (GFZ, Potsdam)
SST	Sea Surface Temperature
SVAT	Soil Vegetation Atmosphere Transport
UTC	Universal Time Coordinated
WRF	Weather Research and Forecast modeling system

Mathematical notations

$\nabla \cdot \vec{Q}$	Vertically integrated moisture flux convergence [kg/(m^2 s)]
$\vec{v}_h$	Horizontal wind vector [m/s]
$\vec{Q}$	Vertically integrated horizontal atmospheric moisture flux [kg/(m s)]
E	Evapotranspiration [mm]
g	Gravitational constant [m/s^2]
M	Terrestrial water storage from GRACE [mm]
P	Precipitation [mm]
p	Air pressure [Pa]
q	Specific humidity [kg/kg]
R	Discharge / Runoff [mm]
S	Terrestrial water storage [mm]
t	Time
W	Atmospheric water storage [mm]

Abstract

Since 2002, the *Gravity Recovery And Climate Experiment* GRACE provides global high resolution observations of the time variable gravity field of the Earth. Besides other fields of application, this information is used to derive spatio-temporal changes of the terrestrial water storage body. Due to the lack of suitable direct observations of large scale water storage changes, a validation of derived GRACE mass variations remains difficult.

In this study, an approach is presented that allows the appraisal of the quality of GRACE for assessing the terrestrial water storage variations of continental scale hydrological basins. This is done by comparing the GRACE products to aerologic water budgets that are derived from the vertically integrated atmospheric moisture flux divergence. Aerologic water budgets of global atmospheric reanalyses are explored, covering the products of the *European Centre for Medium-Range Weather Forecasts* (ECMWF) and the *National Centers for Environmental Prediction* (NCEP). Furthermore, dynamic downscaling is applied to obtain high-resolution refinements of the coarse global reanalysis fields. For that purpose, the *Weather Research and Forecast modeling system* (WRF) is chosen. Prior to the evaluation with GRACE, all aerologic products are validated against global gridded observations data sets of precipitation and 2m-temperature.

Atmosphere related uncertainty bounds for the terrestrial water storage variation are obtained from different configurations of the downscaling model WRF in combination with the two involved global reanalyses. The resulting atmospheric uncertainty ranges are opposed and compared with uncertainty ranges originating from three different GRACE products of the data centers *GeoForschungsZentrum Potsdam* (GFZ), *Center for Space Research* (CSR) and *Jet Propulsion Laboratory* (JPL). The results show that regional atmospheric downscaling is able to add value to the global reanalyses, depending on the geographical location of the considered catchments. In general, global and regional atmospheric water budgets are in reasonable agreement with GRACE derived terrestrial water storage variations (r=0.6–0.9). However, both atmospheric and satellite based approaches reveal significant uncertainties. In particular, for regions with minimal storage change rates, i.e. desert environments, the limitation of both methods is revealed.

The study encompasses six different climatic and hydrographic regions. They comprise the Amazonian Basin, the combined river catchments of Lena and Yenisei, the Central Australian Basin, the Saharan Desert, the Lake Chad depression, and the Niger river catchment.

Zusammenfassung

Seit dem Jahr 2002 stellt das *Gravity Recovery And Climate Experiment* GRACE globale, hoch aufgelöste Beobachtungen des zeitveränderlichen Schwerefelds der Erde zur Verfügung. Neben vielen anderen Anwendungsbereichen kann diese Information zur groben Bestimmung der räumlich-zeitlichen Variation des terrestrischen Wasserspeichers verwendet werden. Da jedoch die direkte Messung von großskaligen Wasserspeicheränderungen mit anderen Methoden nicht oder nur unzulänglich möglich ist, können die GRACE Beobachtungen nicht direkt validiert werden.

Im Rahmen dieser Studie wird eine alternative Methode verwendet um die Eignung von GRACE zur Bestimmung der terrestrischen Wasserpeichervariationen zu untersuchen. Unter Verwendung der aerologischen Wasserbilanz, die auf die vertikal integrierte Feuchtefluss-divergenz zurückgreift, kann bei bekanntem Abfluss die Speicheränderung für ein Gebiet bestimmt werden. Die aerologische Wasserbilanz wird hier aus den Feldern zweier globaler atmospherischer Reanalysen berechnet. Dazu werden Produkte des *European Centre for Medium-Range Weather Forecasts* (ECMWF) und des *National Centers for Environmental Prediction* (NCEP) verwendet. In einem weiteren Schritt wird untersucht, ob die globalen Reanalysen mittels dynamischem Downscaling verbessert werden können. Zu diesem Zweck wird das regionale atmospärische Modell *Weather Research and Forecast modeling system* (WRF) eingesetzt. Vor dem Vergleich mit GRACE werden alle globalen und regionalen aerologischen Datensätze anhand von globalen Rasterdaten für Niederschlag und 2m-Temperature validiert.

Aus den globalen und verfeinerten atmosphärischen Feldern werden atmosphärische Unsicherheitsspannen abgeleitet. Diese werden anschließend der Variabilität von drei verschiedenen GRACE Produkten gegenüber gestellt. Sie umfassen die Daten des *GeoForschungsZentrum Potsdam* (GFZ), des *Center for Space Research* (CSR) und des *Jet Propulsion Laboratory* (JPL). Für verschiedene untersuchte Gebiete stellt die regionale Verfeinerung eine Verbesserung der atmosphärischen Felder dar. Es zeigt sich hierbei jedoch eine Abhängigkeit von der geografischen Lage bzw. der Klimatologie der betrachteten Gebiete. Insgesamt resultiert aus dem Vergleich der aerologischen Wasserbilanz mit GRACE eine hohe Übereinstimmung (r=0.6–0.9). Allerdings existieren für den aerologischen Ansatz, als auch für GRACE erhebliche Unsicherheiten. Speziell für Regionen mit geringer Wasserspeicheränderung, wie zum Beispiel Wüsten oder semi-aride Gebiete, befinden sich die Signale im Bereich des Rauschen.

Sechs klimatisch und hydrografisch verschiedene Gebiete werden im Rahmen dieser Arbeit untersucht. Diese umfassen das Amazonasbecken, die Einzugsgebiete von Lena und Jenissei, das zentralaustralische Becken, die Sahara, die Senke des Tschadsees und das Einzugsgebiet des Niger.

1

Introduction

On seasonal to monthly timescales, the assessment of the different quantities of the hydrological cycle on a global to continental extent is limited by the lack of sophisticated methods for their measuring (Trenberth *et al.* , 2007) or by the low spatial resolution of the measuring networks. A reasonable number of studies exists on the climatological water balance of the globe (Oki & Kanae, 2006). For river basins, on the scale of several million square kilometers, solving the hydrological water budget equation

$$P = E + R + \frac{dS}{dt} \tag{1.1}$$

of precipitation P, evapotranspiration E, basin discharge R, and the water storage S is often not possible because of missing observations data. Discharge measurements are often unavailable due to technical or political reasons. Estimations of evapotranspiration are fraught with uncertainty and, so far, the terrestrial water storage term could only be assessed by solving the water budget equation for it.

With the introduction of the *Gravity Recovery and Climate Experiment* (GRACE) in 2002, space borne observations of the terrestrial water storage variations became available for the first time. Regrettably, this method cannot be understood as a direct measurement. The satellite mission covers the spatio-temporal variations in the global gravity field and accounts thereby for the total integral of mass variations in the Earth system. Hence, signal contributions that originate from e.g. atmospheric or oceanic dynamics have to be removed to conclude on the water storage variations. This procedure relies on global data assimilation models and thus introduces additional uncertainties.

With GRACE and observations of precipitation and discharge, the hydrological water budget equation can be solved. However, because of lacking evapotranspiration information, a validation of GRACE with independent hydrological observations is not possible; the correctness of the closed water balance cannot be determined. Besides the problem of separating the hydrological part of the GRACE signal, additional uncertainties emerge from the gravity field derivation process .

The use of aerological data provides a way to overcome the problem of unsatisfactory evapotranspiration data. Atmospheric water budgets, derived from the balance of horizontal moisture transport can be used as a proxy for precipitation minus evapotranspiration. Hence, if the discharge of a certain river catchment is known or if regions are chosen where no discharge leaves the surrounding boundary, the storage term of the water balance equation can be assessed and an evaluation with GRACE becomes possible.

Atmospheric water budgets rely on detailed information about variations in wind and humidity. Such measurements are usually derived from radiosondes. Globally, about 800 launch sites exist, a few even on ocean vessels or in the Antarctic. Nowadays, these observations are complemented by techniques of remote sensing, e.g. radio occultation between satellites or LIDAR. Despite of the different sounding methods, the data density varies with space and time. To obtain a steady global coverage, atmospheric analysis models are required. They combine interpolation methods with a physical representation of the atmospheric dynamics. Currently, the two prevalent global atmospheric models that cover the entire period of the GRACE mission are operated by NCAR/NCEP and ECMWF. The spatial resolution of the two is quite different. The NCAR/NCEP approach, since established in 1996, contains 28 vertical layers and a horizontal discretization of 2.5 °. The INTERIM reanalysis of ECMWF is a more recent development comprising 60 vertical layers and a horizontal resolution of $0.75\,^\circ \times 0.75\,^\circ$.

A direct assessment of the validity of the modeled atmospheric water budgets with observations is problematic because precipitation and evapotranspiration are computed from physical schemes that are usually not fully connected to the assimilation based atmospheric moisture budgets. E.g. E and P is computed by a forecast model that is only initialized once with the assimilation model. Hence, if the simulated rainfall does not agree with ground based measurements, the representation of moisture advection in the model is not necessarily wrong. An incorrect evapotranspiration can be compensated by an overestimation of precipitation while the atmospheric moisture budget remains reasonable. This factor can be avoided by deploying atmospheric moisture flux budgets instead of $P-E$.

The range between the different global models will provide uncertainty estimates for the atmospheric moisture budgets. The evaluation will show if GRACE and the atmospheric models agree well, or if one approach contains a higher amount of uncertainty.

Dynamic downscaling offers the opportunity to enhance the global fields in terms of spatial and temporal resolution. Regional atmospheric models use the global fields as driving boundary conditions. Within the model domain, all physical processes are simulated independent from the global input. By using driving data from different global models, the regional simulations should provide an additional estimate of uncertainty. The regional model contains a number of different physical schemes, e.g for surface exchange, convective, or radiation processes. This induces an additional source of uncertainty.

The computation of **atmospheric moisture fluxes** and surface water exchange is executed separately in the global model. Hence, feedback properties are of minor importance. In WRF, these processes are closely connected and thus, errors in precipitation or evapotranspiration can directly affect the moisture balances.

This study intends to assess the quality of GRACE derived observations of surface and subsurface water storage variations by an evaluation with global fields and regional simulations from different comprising the products of different institutions. The comparison is exercised for selected continental scale river basins and sink regions where no discharge leaves the outer boundaries. For the dynamic downscaling of the global fields, the *Weather Research and Forecast modeling system* WRF (Skamarock *et al.* , 2008) is applied. Besides the basin averaged time series, a special focus is set on the spatial distribution of precipitation and temperature. Unreasonable spatial patterns can also lead to good results when the over- and underestimations cancel out for the area of interest.

Study Domains Simulations with regional atmospheric models are computationally very demanding. Therefore, it is not possible to prepare simulations with a global coverage. For this study, in order to cover different climatic conditions, four globally distributed domains were selected, comprising the Amazonian tropics, Northern and Central Africa, Siberia, and Australia. Due to the coarse resolution of the GRACE products, for comparison a minimum size of 10^6 km^2 is considered for the minimum size of the hydrological basins. In addition to that, the availability of discharge data is mandatory, unless no runoff leaves the catchment boundaries. Figure 1.1 visualizes the different domains with the river basins and hydrological sinks that are selected for the comparison with GRACE in this study.

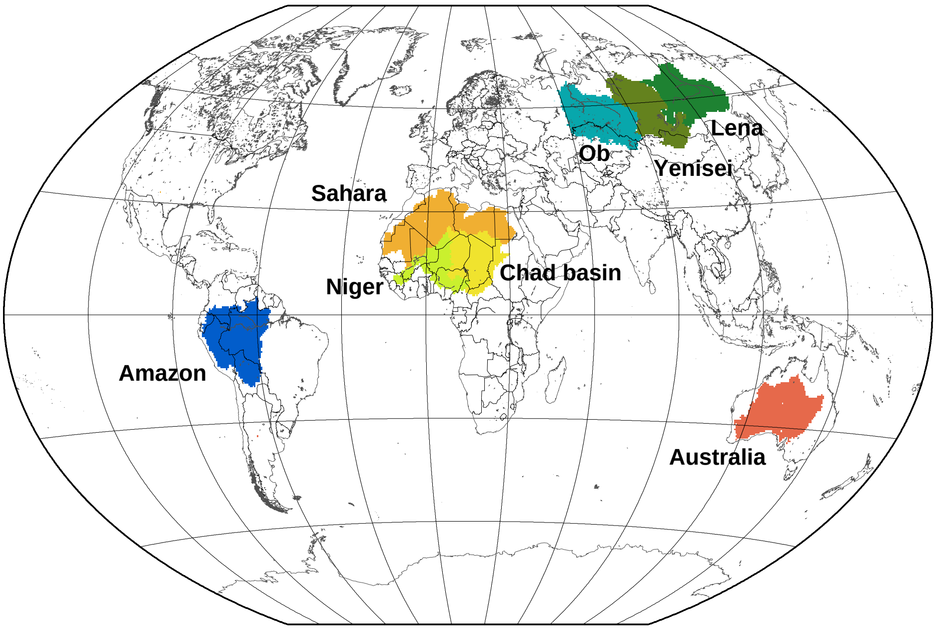

Figure 1.1.: Global distribution of the selected study domains. Sahara and Australia represent arid conditions. The Siberian domain reflects polar continental climates and the Amazon stands for humid and monsoonal properties.

The **Amazonian domain** represents tropically moist conditions with large amounts but also seasonal variation of precipitation and thus terrestrial water storage variation. The **North/Central African** domain is also characterized by tropical conditions in the southern part. Also monsoonal rainfall plays an important role for the water budget of the river **Niger** and the **Lake Chad basin**. Towards the north, the conditions change towards dry and hot. The **Saharan basin** is selected according to the surrounding watershed. It represents absolutely dry conditions, with only minor seasonal variations in the terrestrial water storage. The **Central Australian basin** is characterized by similar conditions. However, the intra annual water storage variations lie usually above those of the Sahara. The **Siberian domain** comprises the river basins of **Yenisei and Lena** and stands for winter cold, polar and tundra climates. During polar winter, surface runoff is immaterial and evapotranspiration comes almost to a standstill.

The selected study regions will convey a comprehensive overview on the applicability of GRACE and hydrometeorological water budgets in the quantitative hydrological sciences.

The following chapter provides an overview on the methods and models that are used and developed for this study. Furthermore, the different data products are explained. Consecutively, the results for each study region are presented in separate chapters. Chapter 7 contains some general findings that are valid for all or most of the study regions. In chapter 8 the methodologies and results summarized and debated. An finally the study ends with an overall conclusion and outlook statement.

2

Methods

2.1. Study Concept

Since very recently, the ***G**ravity **R**ecovery **A**nd **C**limate **E**xperiment* (GRACE) provides the opportunity to observe the large-scale terrestrial water storage variations (Wahr *et al.* , 1998). With GRACE, the spatio-temporal variations in the global water storage body are derived by a continuous observation of the gravity field of the earth from space. For the first time it is hoped to be able to close the water balance solely by further observation of P and R, so that evapotranspiration remains as the residual term:

$$E = P - R - \frac{dS}{dt} \equiv P - R - \underbrace{\frac{dM}{dt}}_{\text{GRACE}} \tag{2.1}$$

The spatial resolution of the satellite product can reach about 400 to 500 km^2 if the chosen timescale is one month (Tapley *et al.* , 2004). However, the variations in the gravity field that are measured by the satellites represent the integral of spatio-temporal mass variations on earth. The signal comprises low frequency processes like post-glacial rebound, mid frequency processes like polar ice melt, and high frequency mass variations like tides, ocean currents, hydrological storage variations, and atmospheric mass variations.

The separation of the hydrological storage variations requires the complete removal of all the overlaying signals that result from other compartments. With global coverage, usually, the necessary data is not available from measurements. Hence, geophysical models are required to substitute the lack of information. Unfortunately, these models contain errors that can accumulate within the hydrological GRACE products.

From this point of view, it becomes clear that GRACE derived water storage variations are not necessarily fields of high accuracy. If information about P, E and R is available, Equation1.1 can be solved for $\frac{dS}{dt}$. Most often, this approach fails because of lacking evapotranspiration data (Werth & Avissar, 2004). One solution to this problem is the restriction to regions where parts of Eq. 1.1 become zero or can be neglected. This is the case e.g. for the Siberian Tundra where evapotranspiration is negligible during winter (Fukutomi *et al.* , 2003). If the Central

Australian Plane or the Sahara desert are considered as basins with no outlet, the runoff term becomes eliminated.

However, the evaluation of GRACE at basins with restricted E or R can of course cover only a small portion of the global land masses and a certain time period in the seasonal signal of mass variations. An alternative way to overcome the problem of insufficient evapotranspiration information is the consideration and evaluation of atmospheric moisture budgets, as outlined in the following section.

Atmospheric Water Budget The terrestrial water balance equation (Eq. 1.1) contains two external sinks (E and R) and one source (P). While the discharge term can be measured at a single location with reasonable accuracy, the quantification of precipitation and especially evapotranspiration remains critical. For large scale areas of 10^6 km^2 or more and at monthly to seasonal time scales, the spatial averaged water budget of the atmosphere can be considered as a proxy for precipitation minus evapotranspiration. The atmospheric water budget is given by

$$\frac{\partial W}{\partial t} - \nabla \cdot \vec{Q} \quad = \quad P - ET \tag{2.2}$$

in units of mm month^{-1}, with W and $-\nabla \cdot \vec{Q}$ denoting the atmospheric water storage and the net balance of moisture flux, respectively. The vertical integral of moisture convergence is defined by

$$-\nabla \cdot \vec{Q} \equiv -\frac{1}{g} \nabla \cdot \int_{p=0}^{p=p_{sfc}} \vec{v}_h \, q \, dp \tag{2.3}$$

with air pressure p [Pa] and the gravitational acceleration g [m/s^2], the horizontal wind vector $\vec{v}_h$ [m/s], and the specific humidity q [kg/kg]. For the considered spatial and temporal scales, the variations of the atmospheric water storage W can be assumed to be negligible (Peixoto & Oort, 1992). Hence, the net atmospheric water balance $-\nabla \cdot \vec{Q}$ is directly linked to the vertical exchange terms of the terrestrial water balance. From equation 2.2 the combined atmospheric-terrestrial water budget follows as

$$-\nabla \cdot \vec{Q} - \frac{\partial S}{\partial t} \quad = \quad R \tag{2.4}$$

with discharge R and the water storage changes dS/dt.

$$-\nabla \cdot \vec{Q} - R = (P - E) - R = \frac{dS}{dt} \tag{2.5}$$

Atmospheric water budgets have been used in several hydrological and meteorological applications like e.g Palmén & Södermann (1966); Roads *et al.* (2002); Berbery *et al.* (1996); Famiglietti & Yeh (2008); Hirschi *et al.* (2007); Labraga *et al.* (2000).

Studies, that compare water budgets derived from prevalent global atmospheric models to GRACE can be found in Hirschi *et al.* (2006); Seitz *et al.* (2008); Syed *et al.* (2005, 2007, 2009). Most of these authors do not address the caveats and shortcomings contained in the global reanalysis fields of NCEP and ECMWF as described by Hagemann *et al.* (2005); Trenberth & Guillemot (1998); Trenberth *et al.* (2007). Moreover, the uncertainty bounds that arise from using either NCEP or ECMWF reanalyses are usually not evaluated.

The assessment of $-\nabla \cdot \vec{Q}$ requires three dimensional information about wind, specific humidity, pressure, and temperature. Such data is typically available from radio sounding profiles.

The global measuring network for that method is however rather coarse. Therefore, the information about the atmospheric state is complemented by airborne, spaceborne, and ocean vessel observations. To obtain spatially interpolated fields, the combined data is assimilated and processed with atmospheric analysis models. Depending on the available data density and the conceptual formulation of the analysis model, the resulting fields will be different. In order to get an estimation about the uncertainty of the atmospheric water budget approach, in this study, different prevalent analysis products will be compared for selected river basins and sinks.

Fields of vertically integrated atmospheric moisture fluxes can e.g. be obtained from global atmospheric reanalysis models like NCAR/NCEP NNRP (Kalnay *et al.* , 1996), ECMWF ERA-40 (Uppala *et al.* , 2005) and ERA-INTERIM (Uppala *et al.* , 2008). However, problems exist also with the reanalysis models. Cullather *et al.* (2000) found that $P-E$ values from NCEP and ECMWF forecast fields are about 60% below those obtained from the atmospheric moisture budgets. Hence, using atmospheric moisture budgets for substituting $P-E$ is not only a means for overcoming the problem with lacking observations of E. It also may avoid modeling errors and uncertainty that is associated with predicting P and E in a reanalysis model.

Both of the considered reanalysis products can imply erroneous water budgets. This leads to the question if dynamically downscaled fields of atmospheric moisture flux divergence are able to provide additional skill to regional water budget calculations. A regional atmospheric model cannot outperform the structural errors inherited from the global fields. Improvement is expected by a more detailed representation of orography and a higher temporal resolution (Castro *et al.* , 2005).

2.2. Atmospheric Water Budgets: Global Reanalyses

Although the relative concentration of water in the air is rather small ($10^{-5}-4$ %) (Jacobson, 1999), it strongly affects the dynamics and physical processes of the atmosphere. By absorbing long wave radiation, atmospheric moisture raises the global mean air temperature by about 20 °C. The water in the atmosphere has an equivalent height of about 25 mm. The long term global mean of precipitation is about 800 mm. Thus, the mean residence time can be calculated with 10 days (Häckel, 1999).

Global atmospheric models treat the lower boundary processes in a very simplified manner. Usually, only a small number of vertical soil layers is defined. Groundwater flow and storage is not taken into account. Infiltration excess leaves the system without the possibility of returning into the atmosphere or ocean. For the simulation of atmospheric processes, on a continental to global scale, this modeling concept may be sufficient. However, the closure of the water balance is usually not a subject to atmospheric simulations. E.g. open water bodies like oceans and lakes depict infinite sources for evaporation. On the other hand, in many of the known global atmospheric models, water is removed if it percolates through the lowest soil layer, without the possibility of returning.

Over the past three decades, accuracy, spatial resolution, and prediction periods of numerical weather prediction (NWP) improved substantially (Kalnay *et al.* , 1996; Uppala *et al.* , 2005; Trenberth *et al.* , 2007). Increasing computational power and the introduction of global satellite measurements are the reasons for this progress. For NWP two major fields of application exist, namely short term forecasting and long term simulations of past to present conditions. For forecasting immediate available data is essential. However, data sources with larger update intervals significantly improve atmospheric predictions. Therefore, analysis models with real-time data assimilation are used for weather predictions. In order to improve the forecast accuracy these models are continuously developed further. Long term trends should not be evaluated, because data sources, model resolution, and model physics can change with time. Retrospective analysis (reanalysis) models seek to avoid such inconsistencies. An atmospheric reanalysis relies on a consistent data assimilation. Model physics and resolution remain constant over time. For past periods, the amount of available assimilation data is vastly increased. The combination of elevated data ingestion and consistent model configuration qualifies the reanalysis concept for the evaluation of water budget quantities.

2.2.1. ECMWF

The *European Centre for Medium-Range Weather Forecasts* (ECMWF) is an international organization, currently supported by 31 membering nations. In 1979, ECMWF started producing operational weather forecasts. In 1985, the *Integrated Forecast System* (IFS) was introduced. Since then, the IFS has been developing further. Currently, it works with a T255 grid ($\approx 78\,\text{km}$) and 60 vertical layers. ECMWF has been using this model to produce their Operational Analysis and different Reanalysis products. Table 2.1 gives an overview of ECMWF's assortment.

In 1993 ECMWF started its ERA-15 reanalysis project. This consistent atmospheric simulation covers the 15 year period from 1979 to 1994. The spectral resolution is T106 ($\approx 125\,\text{km}$) with 31 vertical layers. According to Uppala *et al.* (2005), ERA-15 shows too cold winter surface temperatures, a serious drying of the western Amazonian land surface, negative precipitation minus evaporation values, and a problematic satellite data assimilation.

In 2000, the next reanalysis project was started by ECMWF. The considered time period was extended to 40 years. In fact, the simulation period spans from 1957 to mid 2002. ERA-40 has a spectral resolution of T159 ($\approx 100\,\text{km}$) and 60 vertical levels. Many shortcomings of ERA-15 were eliminated with the new system. However, in terms of the hydrological cycle, some severe deficiencies still exist with respect to the global water budget. Especially for the tropical regions, precipitation is overestimated i.e. ocean precipitation exceeds evaporation (Hagemann *et al.* , 2005; Trenberth *et al.* , 2007).

Recently, ECMWF started its new reanalysis project ERA-INTERIM. The simulation period starts in 1989. A specific ending date has not been defined. The spatial resolution further increased to T255 ($\approx 78\,\text{km}$) with 60 vertical layers. The humidity analysis part was renewed, the model physics were improved, and radio occultation information from satellites was introduced. Since ERA-INTERIM became available in late 2008, no publications concerning a detailed hydrological analysis of the reanalysis data could be found.

Currently, in terms of water budget analysis, ERA-INTERIM is the most sophisticated reanalysis product from ECMWF. Moreover, ERA-40 and ERA-15 do not interfere with the period of available GRACE satellite data. The Operational Analysis is inconsistent concerning data assimilation, model physics and resolution. Hence, for this study ERA-INTERIM is taken as one of the two global atmospheric simulation scenarios.

The atmospheric fields of ERA-INTERIM are available from ECMWF's website. The maximum available spatial resolution is $0.75\,^\circ \times 0.75\,^\circ$ (interpolated). The temporal storage interval

Table 2.1.: Atmospheric analysis and reanalysis products available from ECMWF.

Product	**Stretch**
Operational Analysis	1985–now
ERA-INTERIM	1989–now
ERA-15	1979–1994
ERA-40	1957–2002

is six hours at 00, 06, 12, and 18 UTC. The data can be obtained for model-, pressure-, and sigma levels.

ERA-40 fields of vertically integrated moisture flux divergence are also directly available from the data server. For ERA-INTERIM this diagnostic is not provided publicly. However, the former ECMWF staff member Dr. Pedro Viterbo and his successor Dr. Gianpaolo Balsamo kindly made it available for this study.

2.2.2. NCAR/NCEP

Shortly after ECMWF has introduced its ERA-15, the *National Center for Atmospheric Research* (NCAR) and the *National Center for Environmental Prediction* (NCEP) started a joint global reanalysis project (NNRP). The suggested modeling period was chosen with 40 years, starting with 1957. The selected model configuration is identical to the operational system that became operational at NCEP, in January 1995. Only the horizontal resolution is decreased from T126 (≈ 105 km) to T62 (≈ 210 km). The vertical discretization is 28 layers (Kalnay *et al.* , 1996).

The simulations did not end, as intimated, after the 40 year period. The reanalysis is still being continued. Compared to ERA-INTERIM, NNRP has a coarser spatial resolution. The atmospheric fields are available at a 144 × 73 grid (2.5°) with 17 pressure levels (1000-10 hPa) for temperature, geopotential, and horizontal wind, 12 (1000-100 hPa) for pressure vertical velocity, and 8 (1000-300 hPa) for relative humidity.

The evaluation of NNRP revealed problems with drying soils and the representation of snow (Roads *et al.* , 2002). The experienced shortcomings led to the development of a second reanalysis model, the NCEP-DOE AMIP-II *Reanalysis* where several changes were made to the land-surface model and the radiation physics in the model. However, the representation of the atmospheric properties and the data assimilation method is similar to NNRP (Roads *et al.* , 2002; Kanamitsu *et al.* , 2002). Therefore, it is assumed that NCEP2 will yield to almost identical results for the atmospheric moisture flux balance.

For NNRP, no fields of vertically integrated moisture flux divergence are provided by the data center of NCAR. This necessitates the computation from available fields. It is to be regretted that NCAR/NCEP could not prepare the desired data from their 28 layer model data. For self computation, only the 17 pressure level data is available. Specific humidity is only archived up to the 8th pressure level. A more detailed description on the computation of the moisture flux divergence fields is given in section C of the Appendix.

2.3. Atmospheric Water Budgets: Regional Downscaling

In the previous section, recently available global reanalysis models were introduced and reviewed and their possible skill for water budget estimations was argued. The facile representation of hydrological processes, especially at the land surface and for the soil layer, and the coarse spatio-temporal resolution are the most severe limitations in terms of quantifying the terrestrial water budget at continental scale river basins or regions.

The deficiencies of the global models caused the scientific community to develop downscaling approaches for global simulation results. Statistical methods use high resolution elevation information to correct for height. Also spatial patterns e.g. of soil, land-use or vegetation type can be utilized for horizontal interpolations. Statistical downscaling accounts for biases, caused by the crude representation of spatial features in global models. However, spatial redistribution of water cannot be achieved with statistical methods. This is only possible when the resolution of the physical-based model is increased. A higher model resolution implies an altered orographic structure. This has consequences for the movement of the air masses. More detailed information about land use, soil type and vegetation affects the albedo and thus the radiation processes.

Mesoscale atmospheric models have been developed to perform such locally refined simulations. Starting and boundary conditions can be taken from a global model. The atmospheric dynamics and physics processes are completely recomputed. This concept is known as dynamic downscaling.

The central question is now if such a regional hydrometeorological model is able to add value to a global simulation. The detailed description of physical processes and atmospheric dynamics, as well as the increased spatial and temporal resolution suggest an improving accuracy for the quantification of hydrological fluxes. For the global models presented, $-\nabla \cdot \vec{Q}$ is only available at every six hours (00, 06, 12, and 18 UTC). This means that essential portions of the diurnal cycle might be missing for certain locations on the globe. With the regional model the fluxes are integrated over time using a much smaller interval, typically 30 seconds to a few minutes. However, independent from the model resolution, the verification of simulation results is always a problem because of the limited data availability. At least, the comparison of water budget terms of a regional simulation and its global driving model allows the estimation of uncertainties.

Prevalent mesoscale atmospheric and climate models are the *Weather Research and Forecast model* WRF (Skamarock *et al.* , 2008) and its predecessor MM5 (Grell *et al.* , 1995), the *Regional Model* REMO (MPI, Hamburg), the *Lokal Modell* COSMO-LM (DWD), and the *Regional Atmospheric Modeling System* RAMS (Cotton *et al.* , 2003). For this study, the decision fell on WRF. The model combines several conceptual and practical advantages. Static input data, such as elevation, land-use and vegetation type, albedo, soil properties are available on a global extent. The formulation of the model dynamics and physics is mass conserving. A sophisticated concept for the execution on massive parallel computers as well as the high flexibility for defining the properties of the model domain made WRF the preferred choice.

2.3.1. Model Description

The Weather Forecast and Research modeling system WRF addresses the simulation of atmospheric dynamics on a scale much smaller than depicted by global atmospheric models. Depending on the field of application, various configurations of WRF can be realized. In general two variations of the WRF Software Framework (WSF) are maintained: the *Non-hydrostatic Mesoscale Model* (NMM), developed at NCEP, and the *Advanced Research* WRF (WRF-ARW) from NCAR. The two versions apply different dynamic solvers inside the WSF. The WRF-NMM version is intended as a real time numerical weather prediction model. WRF-ARW focuses on regional modeling, ideal simulations, and other fields like air chemistry (WRF-CHEM) or hurricanes (HWRF). It is also possible to apply the modeling system on a global extent (Global-WRF). WRF is also applied for the dynamical downscaling of global climate models.

The basic model architecture, comprising the parallelization implementation, data in- and output, and equation solvers, is being developed and maintained by the National Center for Atmospheric Research (NCAR), the National Oceanic and Atmospheric Administration's (NOAA) National Centers of Environmental Prediction (NCEP) and Forecast System Laboratory, and many other institutions and scientists in the US and elsewhere (Skamarock *et al.* , 2008).

WRF-ARW relies on the Mesoscale Model 5 (MM5), developed at the Pennsylvania State University (PSU) and NCAR. The most notable improvements in WRF-ARW are the terrain following mass (η) coordinate and the 3rd order Runge Kutta integration scheme. Compared to the σ coordinate in MM5, the new model describes the atmosphere in a fully compressible, non-hydrostatic, and mass conserving way. Regarding numerical and forecast stability, the new integration scheme outperforms the Leapfrog formulation of MM5 (Skamarock & Klemp, 2008).

For the downscaling of global atmospheric reanalyses, WRF-ARW is applied in *real mode*. This means that real data (compared to ideal assumptions) is used to drive the regional model. A regional atmospheric simulation requires the solving of an initial value and a boundary value problem. Hence, at start, the model is initialized with several two- and three dimensional fields that describe the land surface properties and the initial atmospheric state. Time variant lateral and lower boundary values are obtained from global fields. To fit the regional model's temporal resolution, the boundary conditions are linearly interpolated, at run time.

Physical processes like radiation or land-surface interactions as well as sub-gridscale features like cumulus precipitation or eddy transport affect the atmospheric tendencies. In WRF, such mechanisms are taken into account by physical driver modules. For most of the physical compartments more than one module is available. With version 3.1 of WRF-ARW a total number of 31 physical modules is provided. Table 2.2 depicts their distribution into different compartments. Theoretically, 6,912 variations exist for the combination of those modules. Practically, many combinations are ineligible. However, omitting unusable configurations does not lead to an unequivocal model setup. Hence, testing of different physical model realizations for identifying suited model setups is unavoidable. The differences in simulated precipitation and temperature characteristics between different model setup can be significant.

Because of the non-linear nature of the model's differential equations, a complete algebraic integration is impossible. Thus, numerical approximation is required. In WRF, finite-difference methods are employed for solving atmospheric dynamics and physics. Regarding numerical stability, according to the Courant–Friedrichs–Lewy (CFL) condition, the integration time step for dynamic processes depends on the horizontal discretization in the model. $dt = 6dx_{km}$ gives a good approximation. E.g. a $(30\,\text{km})^2$ run requires an integration time step around 180 seconds. Physical conditions that change relatively slowly with time are usually updated at a longer time interval. For example, radiation is usually called every 30 minutes, the sub-grid scale cumulus parametrization every 5 minutes. This measure reduces computational effort and hence simulation time.

In contrast to its predecessor, the Mesocale Model 5 (MM5), WRF provides a well designed program structure. Prior to compilation, a special preprocessor creates source code for declaration, allocation, and deallocation of variables that were previously defined in the model registry. Such a code design significantly reduces errors and provides a clear code structure. In version 2.2, WRF has about 160,000 lines of code (Masoud Sajadi, 2007).

Table 2.2.: Available physic modules in WRF-ARW version 3.1 (Skamarock *et al.* , 2008)

Compartment	**Available modules**
Short wave radiation	4
Long wave radiation	3
Planetary boundary layer	4
Microphysics	9
Surface layer	3
Land surface	4
Convective parametrization	4

2.3.2. Model Configuration

Terrestrial static boundary conditions

Stationary fields like land-use and soil categories, annual mean deep soil temperature, terrain height, slope category, monthly vegetation fraction, monthly albedo, and maximum snow albedo are needed for setting up WRF. The necessary data can be downloaded on the WRF-user website. Depending on the type of data, different horizontal resolutions are available (table 2.3).

GEOGRID, a tool of the WRF Preprocessing System (WPS) performs a horizontal interpolation of the fields onto the model grid. It is also possible to import alternative data sets with the WPS, e.g. SRTM elevation, high resolution sea-surface temperature or land-use data from further sources.

Meteorological forcing, transient boundary conditions

The time variant boundary conditions for the regional atmospheric model can be subdivided into three categories. At lateral boundaries, information about atmospheric dynamics is required. That comprises horizontal wind, water vapor, geopotential height, and temperature data. The data is usually taken from a global atmospheric model. A typical temporal resolution of such data is six hours. For the lower boundary, spatially distributed information about sea-surface temperature (SST), land use type, vegetation cover and type, and albedo is ingested into WRF. These fields experience changes on a larger temporal scale than the atmospheric state variables. Hence, the update frequency ranges from six hourly for shallow water SST to monthly for vegetation fraction, and albedo.

Moreover, if spectral nudging is applied within the regional model, four dimensional (x,y,z,t) fields are required for the dynamic and state variables of wind, temperature, and humidity. Here the temporal resolution is identical to the lateral boundaries. With spectral nudging (four dimensional data analysis, FDDA) the fields of the regional model become relaxed towards the global model. This allows the propagation of large scale atmospheric patterns into the regional model. Spectral nudging can be applied to the variables temperature, horizontal wind, humidity, and geopotential height.

Model physics

As mentioned previously, processes like radiation or surface exchange significantly affect atmospheric dynamics. In WRF, a large number of physical modules model these physical features.

Table 2.3.: Input for the WPS utility GEOGRID. This data is available from the WRF users website.

Field	Vendor	Resolution
Topography	USGS	10’, 5’, 2’, 30”
Landuse	USGS	10’, 5’, 2’, 30”
Soiltype bottom	USGS	10’, 5’, 2’, 30”
Soiltype top	USGS	10’, 5’, 2’, 30”
Soil temperature	N/A	1°
Max. snow albedo	N/A	1°
Slope category	N/A	1°
Albedo	NCEP	8.64’
Green fraction	N/A	8.64’

In the following, the different compartments are introduced and the configuration used for this study are depicted.

Radiation Radiation processes form the main stimulus to atmospheric dynamics. Absorption of shortwave radiation causes atmospheric and ground heating. The resulting long wave radiation is reflected by clouds and absorbed by atmospheric gases like CO_2 and O_3.

For the simulation of long wave radiation the Rapid Radiative Transfer Model (RRTM) (Mlawer *et al.* , 1997) is selected. The RRTM accounts for the effects that water vapor, O_3, CO_2, and cloud optical depth have on infrared and thermal radiation. 16 spectral bands are resolved. For shortwave radiation processes the Goddard (Chou & Suarez, 1994) scheme is chosen. It considers 11 spectral bands and distinguishes diffuse and direct solar radiation with regard to scattering and reflection (Skamarock *et al.* , 2008).

Microphysics The calculation of water vapor, cloud, and grid-scale precipitation mechanisms is performed by the microphysical schemes. Phase mixing and conversion processes are simulated explicitly. The chosen WRF Single Moment 5 module (WSM5) (Hong *et al.* , 2004) distinguishes among vapor, rain, snow, cloud ice, and cloud water phase. The WSM5 does not account for mixed-phase processes. Such effects become important when the horizontal resolution deceeds about $(10\,\mathrm{km})^2$ (Skamarock *et al.* , 2008).

Planetary boundary layer (PBL) Sub-gridscale fluxes, caused by eddy transports, affect the whole atmospheric column. Those processes are parametrized in the PBL scheme. Vertical diffusion, planetary boundary height, tendencies of temperature, moisture and horizontal momentum are simulated. The module requires energy and moisture fluxes from the land-surface physics. According to the evaluation of Borge *et al.* (2008), the Yonsei University (YSU) (Hong *et al.* , 2006) scheme is selected for this study. The PBL top is deduced from the buoyancy profile. Entrainment in the transition zone of PBL and free atmosphere are formulated explicitly in the YSU model (Skamarock *et al.* , 2008).

Cumulus parametrization If the horizontal resolution exceeds about $(5\,\mathrm{km})^2$, convective and shallow cloud processes cannot be resolved by the numerical representation of the atmospheric model. For the description of sub-grid scale convective precipitation and thus for the water mass budget, cumulus parametrization is essential. Wang & Seaman (1997) give an overview on prevalent convective schemes that are currently incorporated in mesoscale atmospheric models like MM5 or WRF.

In WRF-ARW, four different convective schemes are selectable, i.e. the Kain-Fritsch (KF) (Kain, 2004), the Betts-Miller-Janjić (BMJ) (Janjić, 2000), and two different Grell (Grell & Dévényi, 2002) schemes. Several conceptual changes were applied with the incorporation of these model into WRF. Details can be found in Skamarock *et al.* (2008).

A first model evaluation showed that the cumulus parametrization significantly impacts the amount of precipitation during warm periods. Accordingly, two different schemes, i.e. Kain-Fritsch and Betts-Miller-Janjić, where selected within the scope of this study. The two approaches depict different concepts with respect mass and energy conservation. The Grell methodology is omitted here because of its similarity to the Kain-Fritsch scheme and due to computational effort.

Land-surface exchange Variations in land-use type, soil type, soil moisture content, and orography induce spatial heterogeneity. Such surface exchange processes are vital to obtain a correct representation of atmospheric dynamics in a model. In WRF-ARW the land-surface exchange properties are subdivided into the two components surface layer and land-surface. Friction velocities and exchange coefficients are defined within a surface layer scheme. This information is needed for the calculation of moisture and heat fluxes by the land-surface model. Although three different schemes are available, the MM5 similarity theory model is required for the chosen YSU PBL scheme (Skamarock *et al.* , 2008).

Land-surface models (LSM) take information from surface-layer scheme and compute heat and moisture fluxes for land and sea-ice grid cells. Over water, the fluxes are calculated by the surface layer scheme, itself. ARW provides four different LSMs, differing in the number of soil layers and in the representation of snow and vegetation processes. For this study, the NOAH LSM Chen & Dudhia (2001) is elected. The model was jointly developed by the **N**CEP, the **O**regon State University, the US. **A**ir Force, and the US. **H**ydrologic Research Lab. In the NOAH LSM, the soil is discretized by four vertical layers. In top-down order, their thickness is 10, 30, 60 and 100 cm. The model accounts for soil temperature, soil moisture, evapotranspiration, soil drainage, runoff, canopy effects, and snow coverage. Also, surface sensible and surface latent heat flux, upward long wave and upward shortwave radiation are calculated. However, only vertical fluxes are simulated by the model. Lateral transport of water or heat is neglected. Hence, feedback mechanisms, caused by lateral water redistribution, are not taken into account.

Land surface characteristics In WRF, sea-surface temperature (SST), albedo, vegetation fraction, and sea ice are not predicted. However, the model provides the opportunity to import and update these fields. Climatological vegetation fraction and albedo maps are contained in the preprocessing system of WRF. Sea ice and SST data has to be incorporated from external data sources. For this study, this information is taken from the respective fields that are contained in the global driving reanalyses with six hourly resolution.

As an alternative, WRF provides the option of using constant fields for the land surface characteristics. If this configuration is chosen, the SST, and sea ice fields are not updated during the simulation and values for the vegetation fraction and albedo are taken from a specified table.

In order to assess the impact of a realistic representation of land surface parameters on the water budget of a domain, both options (constant and table values vs. variable fields) are examined with the regional simulations.

Technical configuration

For this study WRF-ARW with version 3.1 is used. The model is compiled in a 64-bit environment, using PGI's pgf90. For execution on a parallel architecture, MPI support is enabled by MVAPICH2 (Liu *et al.* , 2004). With this configuration, WRF is run on a RedHat NEC linux cluster, equipped with INFINIBAND network technology.

For the chosen study regions the domain sizes lie between 23,000 and 69,000 grid cells. Typically, when using 32 to 48 CPUs the computation time of one simulated year ranges from four days to one week. The computational demand can be reduced by a factor of two to four if the *adaptive time-step* option in WRF is activated. The model integration time step is set with dependence to the Courant–Friedrichs–Lewy (CFL) condition. Hence, if strong gradients exist in the prognostic equations, numerical stability is achieved by decreasing the model time step. Figure 2.1 visualizes the variations in the integration time step in the adaptive mode.

Without using this option, in order to obtain numerical stability, the needed computation time step deduces from the smallest interval that would occur with the adaptive time step option activated.

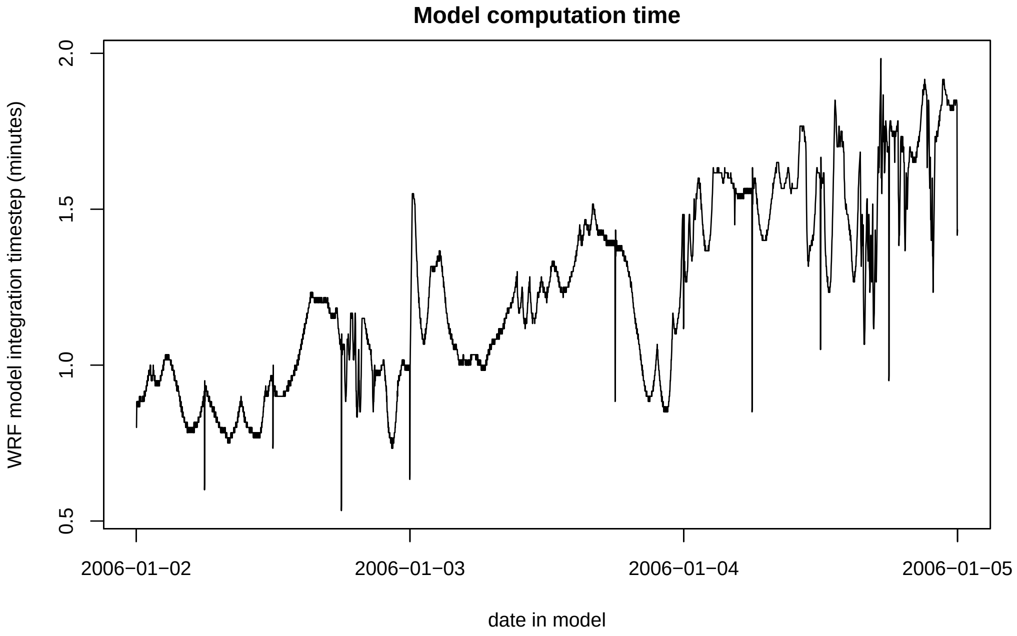

Figure 2.1.: Model integration time-line with activated WRF adaptive time step option.

Despite the benefit achieved by using the adaptive time step option, the computational demand for such simulations is still very high. Performing regional simulations for all of the four chosen geographical regions, and testing of different physical setups, requires a tradeoff between model resolution and computational means. Therefore, the horizontal grid resolution is chosen with $(30\,\mathrm{km})^2$. Vertically, 40 different layers are defined. Although the required model integration time step is about 180 seconds, the archiving interval is set to six hours. Table A.2 lists all fields being recorded for the regional simulations. In WRF-ARW variables are being stored in two different modes. State variables like temperature or moisture are stored for a specific point in time. Budget fields like precipitation or evapotranspiration are stored cumulatively, i.e. the output interval sum is considered. The soil water representation of the regional model requires considerable time to overcome the initial conditions of the global driving data. Therefore, for spin-up the simulations cover two additional years in advance to the start of the GRACE mission.

2.3.3. Regional Simulations Overview

The global distribution of the chosen study regions requires a thorough testing of the impact of different configurations of the regional atmospheric model. The numerous schemes and options that can be selected for WRF-ARW cannot be handled with the available computational resources. Therefore, as described in the previous sections, a certain configuration (tab. 2.4) is chosen according to the suggestions of Borge *et al.* (2008), Skamarock *et al.* (2008), and Wang *et al.* (2009).

Two different global reanalyses are used for the driving of the regional model. The impact of applying two different cumulus schemes is tested for all study regions but the Siberian domain. Furthermore, the sensitivity of spectral nudging (four dimensional data assimilation FDDA) is

Table 2.4.: Chosen WRF-ARW setup for the regional simulations.

Compartment	Selected scheme(s)
Short wave radiation	Goddard
Long wave radiation	RRTM
Planetary boundary layer	YSU
Microphysics	WSM5
Surface layer	MM5 similarity
Land surface	NOAH-LSM
Convective parametrization	Kain-Fritsch, Betts-Miller-Janjić

investigated. Together, up to eight simulations are necessary for one regional model domain. Theoretically, this means the computation of almost 200 simulated years. In reality, not all calculations are performed e.g. because of numerical problems with setting the SST to constant. A comprehensive overview on all performed simulation runs is given in table A.1 of the appendix. With testing and debugging, about 1.5 years of computation time where necessary with the supercomputer of the institute.

No changes are made with respect to predefined constants in the regional atmospheric model. No calibration is performed, neither in general, nor for the single study domains. The quality of the regional simulations is assessed by an evaluation of the results with independent observations of precipitation and 2-meter air temperature. The analysis comprises the spatial patterns and the basin aggregated time series. Those configurations of the regional model that lead to reasonable results are then considered for the comparison with GRACE and the estimation of uncertainty bounds for the atmospheric water budgets.

2.4. Discharge Observations

Solving the water balance equation (eq. 1.1) for $\frac{dS}{dt}$ requires information about the basin discharge R. For basins that are completely enclosed by a topographic boundary, missing an outlet, the discharge term is defined as zero.

The collection of discharge data for globally distributed river catchments is a challenging task. Many states refuse to share their measurements because of political reasons. Available data relies on different measurement and recording methods. In 1988, the *Global Runoff Data Centre* GRDC, was founded under the auspices of the *World Meteorological Organization*. The GRDC collects monthly to daily river discharge data from more than 7300 stations in 156 countries and provides access for non-commercial applications.

This study uses monthly discharge data from the GRDC database. The data was collected and transformed into monthly mean values by a colleague of the DWB project, Henry Kindt (Institute for Hydraulic Engineering, University of Stuttgart). Regrettably, the runoff time series are not available for all desired study regions. Table B.1 gives an overview for the river basins that are contained within the selected study domains.

2.5. Evaluation Data Sets

The estimation of errors and uncertainties of large scale moisture flux derived water budgets is a tough issue. Virtually, proper measurements of evapotranspiration are absent. Precipitation data is lacking a homogeneously dense distribution. This means that a direct validation of $-\nabla \cdot \vec{Q}$

with measurements of P and ET is impossible. Also the true accuracy of GRACE derived water storage changes is unknown, because signal separation and spatial filtering imply another source of uncertainty. Hence, GRACE cannot be used for the validation of the hydrometeorological budget approach.

Station observations of near ground air temperature and precipitation have a rather good density on the continents but also over the oceans when remote sensing is incorporated. For these two variables, global gridded data sets are available from different institutions. The temporal resolution is monthly. The spatial interpolation is usually 0.5°. This data can be considered for an evaluation of the global and regional atmospheric fields on a monthly basis. The comparison will give us some ideas, whether the simulation results are close to reality or not. Moreover, the evaluation will show the uncertainties from the deviance of the different gridded data sets.

2.5.1. Air Temperature

The two prevalent gridded global observation data sets for 2 meter air temperature are prepared at the Climatic Research Unit (CRU), University of East Anglia and at the Center for Climate Research, University of Delaware.

CRUT At CRU, several temperature fields are prepared and hosted. CRUTEM, HADSST, and HADCRUT denote the land surface temperature, the sea surface temperature, and the combination of both, respectively. For this study, the CRUTEM data set is chosen. The monthly fields of CRUTEM3 rely on homogenized, quality-checked observations from 4,349 stations. The horizontal resolution of the product is 5°× 5°. The time series covers the period from 1850 until now. Naturally, the number of ingested observations increases substantially for more recent dates. (Brohan *et al.* , 2006).

This data set will be referred to as CRUT within this study.

DELT The University of Delaware provides a gridded time series of terrestrial air temperature for the period 1900 to 2008. The number of considered stations lies between 1,600 and 12,200, where the higher count refers to the more recent dates. One fraction of the station data comes from the *Global Historical Climatology Network (GHCN)*. This input has a very high quality that is equivalent to CRU. A detailed description of the GHCN can be found in Peterson & Vose (1997). With contrast to CRU, the Delaware product is extended with additional available observations. These combined monthly station averages are then interpolated to a 0.5 °× 0.5 ° grid (Matsuura & Willmot, 2009a).

As this data set has no defined acronym, it will be named as DELT for further usage.

2.5.2. Precipitation

While air temperature can be measured with relatively high accuracy, precipitation is not that easy to quantify. Gauge sampling is error prone because of coarse station networks and the inhomogeneous nature of precipitation events. Radar estimation is still problematic as the conversion from reflectivity to rainfall intensity is highly nonlinear. Also satellite approaches suffer from similar conversion problems. Interestingly, the number of available gridded time series is higher than for temperature. The four products that are chosen for evaluation purpose are described below.

CRUP Similar to CRUT, a precipitation data set is maintained at CRU. It covers the period from 1901 to 2006. Until now, the product is stated as preliminary. Neither a detailed documentation, nor publications were found. The data can be downloaded in 0.5 °× 0.5 ° resolution on the website of the *British Atmospheric Data Centre* (BADC).

DELP This gridded precipitation time series from the University of Delaware is based on the GHCN database, complemented by additionally available station data. The set comprehends the time span from 1900 to 2008. In total 4,800 to 22,000 station time series were incorporated. The horizontal interpolation has a resolution of 0.5 °× 0.5 °. (Matsuura & Willmot, 2009b)

GPCC The *Global Precipitation Climatology Centre* GPCC is located at the *National Meteorological Service of Germany* (DWD). It contributes to the *World Climate Research Program*. Different products of gridded monthly precipitation are available. For the study, the *Full Data Reanalysis Product* (Version 4) is used. While for the period from 1989 to 2001 the data base counts more than 30,000 stations, this number decreases from about 20,000 in 2003 to only 10,000 in the year 2008. Hence, the quality of the product should be comparable to DELP or CRUP. GPCC provides a maximum resolution of 0.25 °× 0.25 ° (Schneider *et al.* , 2008).

However, for compatibility reasons, the 0.5 °× 0.5 ° version is adopted here.

GPCP The *Global Precipitation Climatology Project* (GPCP) is another contributor to the *World Climate Research Program*. GPCPsignificantly differs from the other product by utilizing microwave and infrared space borne observations techniques in addition to ground station measurements. Thus, compared to the precipitation products described before, it is the only real global data set, as it covers not only the land masses but also the oceans. GPCP provides monthly 2.5 °× 2.5 °, and daily 1 °× 1 ° fields. The data is available for the period 1979 to present. The number of included ground stations lies between 6500 and 7000 (Adler *et al.* , 2003).

Due to compatibility reasons, for this study, the monthly product (2.5 °× 2.5 °) is chosen and interpolated to 0.5 °× 0.5 ° with a bi-linear algorithm.

2.6. The GRACE Satellite Mission

The objective of the *Gravity Recovery And Climate Experiment* GRACE is the mapping of the global gravity field of the earth with a maximum spatial resolution of 400 km at a monthly interval (Tapley *et al.* , 2004). It is a joint venture of the *German Aerospace Center* (DLR) and the *Jet Propulsion Laboratory* (JPL) of the NASA. The satellite mission aims at two major goals: improving the models of the static gravity field (geoid) and monitoring the spatio-temporal mass variations of the earth system.

On a monthly time scale, the prevalent process of mass variation on the globe is the redistribution of water within the hydrological cycle. Hence, what GRACE captures over the land areas is mainly changes in terrestrial water storage height. This coherency makes it possible to close a major gap in large-scale hydrology, because extensive ground based measurements of water storage change are well-nigh impossible. With the help of GRACE, for the first time, it is possible to close the water balance solely by observations so that evapotranspiration remains as the residual term (Eq.2.1).

Unfortunately, the GRACE observations are not free from errors. The GRACE measurements depict the integral mass variation between the satellite and its surrounding mass objects. This includes the mass change on earth as well as perturbations in space like e.g. caused by the moon or the planets of the solar system. The derivation of the terrestrial water storage variations requires the complete removal of mass fluctuations from other compartments (Swenson *et al.* , 2003). This necessitates the incorporation of external observations and models and thereby introduces uncertainties. As no global observations exist for evapotranspiration, a validation of the GRACE solutions by hydrological observations is not possible. However, by introducing atmospheric water budget estimates ($-\nabla \cdot \vec{Q} \approx P - E$), an evaluation with GRACE is made possible.

In the following, the possibilities and shortcomings of the GRACE mission and its use for hydrological applications is discussed in more detail.

2.6.1. Mission Configuration

Satellites that follow a near Earth orbit experience alterations of their track because of spatio-temporal variations in the mass distribution of the earth. This deflection is proportional to changes in the global gravity field. Two close by co-orbiting satellites will be affected by the same mass signal with a certain time delay. Thus, the inter-satellite distance correlates with the integrated effect of the global mass distribution.

The two GRACE spacecrafts have a nearly polar orbit (89 °) and were placed about 500 km high. The decay in altitude is about 30 m/day, hence there is no fixed repeat pattern of the ground track. The mean distance between the satellites is 220 ±50 km. A K-band microwave ranging system provides gap deviations with an accuracy of $<10\,\mu$m. The number of orbits per day is 16. The aggregation of approximately one month of data is necessary for a global coverage with a spatial resolution of 400 km (Kim & Tapley, 2002; Tapley *et al.* , 2004).

The mission started on March, 17th 2002, with an intended lifetime of five years, but the healthy condition of the two satellites induced a prolongation beyond the year 2009.

For a precise measurement it is required that the orientation and distance of the satellites remain nearly constant. GPS is used to determine the orbits with high accuracy. Track and position corrections are necessary but of course introduce a bias in the range measurement. Therefore, information from a on board three axis accelerometer is used for the compensation of this error (Kim & Tapley, 2002).

Monthly gravity field solutions are computed by three different institution within the GRACE project, GFZ Potsdam, JPL, and CSR (Center for Space Research, Austin Texas). Additionally, 10-day gravity field solutions are available at the *Centre National d'Études Spatiales* (CNES, France) and also at GFZ.

2.6.2. Gravity Field Solutions

Obtaining monthly global gravity fields from the one Hertz along-track measurements requires considerable numerical effort. The processing starts with the determination of the theoretical observations along the satellite track. Therefore, a background gravitation model is constructed that accounts for all definable properties that affect the ideal orbit. This comprises the mean gravity field of the Earth, the perturbation effects from the Sun, the Moon, and the planets of the solar system, the tides of both, solid earth and ocean, and short term atmospheric and oceanic mass variations. This background model is then interpolated to the observed satellite track which has been computed from GPS and accelerometer data at a five second interval. The deviations between theoretical orbit and actual K–band observation are applied to improve the background model and the calibration of measuring instruments by least-square fitting. This yields improved monthly gravity field coefficients. If these are added back to the initial a-priori gravity field the monthly GRACE gravity field solution (GSM) is obtained. This product is free from oceanic and atmospheric perturbations, and tides. Hence, all mass variations that occur over and under the solid surface of the earth are contained. GFZ, JPL, CSR, and CNES adopt this processing approach for their monthly and 10-day GSM fields. However, differences exist in the background models (Table 2.5) and in the numerical solution strategies (Flechtner, 2007; Bettadpur, 2007; Watkins & Yuan, 2007; Bruinsma *et al.* , 2010).

Table 2.5.: Gravitational background models of different vendors for the gravity field processing

product	a-priori gravity field	sun & planetary perturbations	solid Earth tides
CNES	EIGEN-GL04C	DE403	IERS2003
CSR	GIF22A	DE405	IERS2003
GFZ	EIGEN-GL04C	DE405	IERS2003
JPL	GIF22A	DE405	IERS2003

product	ocean tides	atmospheric mass	ocean mass
CNES	FES2004	ECMWF 3-d pressure 6h	MOG2D
CSR	FES2004	ECMWF 3-d pressure 6h	OMCT
GFZ	FES2004	ECMWF 3-d pressure 6h	OMCT
JPL	FES2004	ECMWF 3-d pressure 6h	OMCT

Figure 2.2 depicts the different compartments of transport and exchange processes of mass in the earth system. The monthly GRACE solutions are corrected for atmospheric and oceanic mass redistribution. Therefore, the remaining signal will mainly account for terrestrial hydrology. However, some additional information is still contained within this signal. Large scale geological convection of the liquid mantle as well as tectonics and volcanic eruptions affect the global gravity field. Nevertheless, compared to hydrological scales, such geological processes can usually be neglected, unless trends are analyzed. Another important effect that has to be considered in terms of trends is the glacial isostatic adjustment (GIA) caused by the melting of ice masses in the past 20,000 years. Uplift rates are usually around 10 mm/yr. Apart from the above described limitations, the GRACE GSM fields can be understood as global temporal snapshots of terrestrial water mass distribution. The portion of water kept in the atmosphere is rather small compared to the amount of continental storage. Thus, the observations from GRACE will allow the estimation of monthly water storage variations. This approach is new to the hydrological sciences and therefore challenging.

2.6.3. Data Quality

As for all geophysical observation systems, the maximal attainable information density of GRACE is determined by the spatio-temporal resolution of the sampling rate. Tapley *et al.* (2004) mentioned a spatial resolution of 400 km for monthly GRACE solutions. Thus, for obtaining accurate estimates the considered region requires a minimum basin scale of several hundred km and gravitational effects that exceed the observational errors of GRACE (Swenson *et al.* , 2003).

Noise reduction The GRACE solutions exhibit spurious stripe patterns with a north to south orientation. A significant amount of noise is contained in the short wavelength components of the spherical harmonic (Stokes) coefficients of the GRACE solutions. A general reduction of noise is achieved by the application of spatial smoothing e.g. with a Gaussian filter. Swenson

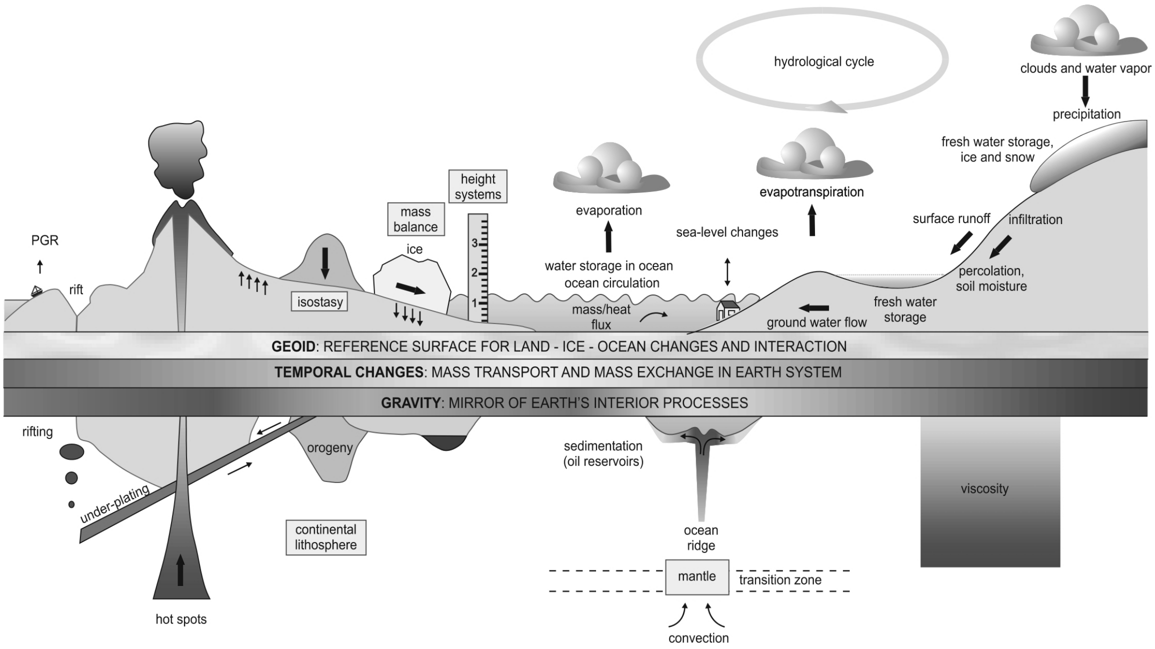

Figure 2.2.: Mass distribution and transport in the earth system (Ilk *et al.* , 2005)

& Wahr (2006) found correlations among the high-frequency Stokes coefficients and derived a methodology for a de-correlation. However, by application of this de-striping algorithm a significant portion of noise remains within the GRACE solutions. This residing noise is addressed by an additional spatial smoothing. Several studies, comparing synthetic signals from global water balance models (e.g. GLDAS) with GRACE estimates, come to the conclusion that spatial smoothing with a Gaussian low-pass filter of 500 to 800 km leads to the best signal to noise ratio in terms of terrestrial water storage variations (Rodell *et al.* , 2004; Swenson & Wahr, 2006). Duan *et al.* (2009) gives an comprehensive overview on the de-correlation and spatial filtering methodologies. Currently, a combination of the Swenson & Wahr (2006) de-correlation approach and Gaussian isotropic filtering is the most widely used approach for estimating terrestrial water storage variations with GRACE. The methodology is also adopted for this study. For Gaussian filtering, a halfwidth radius of 500 km is chosen.

Signal attenuation According to Klees *et al.* (2007) and Chen *et al.* (2007), the Gaussian smoothing of GRACE fields will bias the amplitude of the estimated water storage variation signal. Usually, this effect leads to an attenuation of the amplitudes. Hence, to obtain comparable time series of modeled basin water storage change and GRACE estimates, bias correction is a central issue. Assuming a filter radius of 800 km Klees *et al.* (2007) and Chen *et al.* (2007) showed that for continental scale river basins like the Amazon, Mississippi, Ganges, and Congo, the amplitude of the annual bias ranges between 20% and 35% of the corresponding water storage variation.

Figure 2.3 depicts the attenuation effect of spatial filtering with a Gaussian kernel for the Amazonian study basin. The time series of GRACE (GFZ) is compared to the filtered and unfiltered field of the atmospheric water balance ($-\nabla \cdot \vec{Q} - R$, ERA-INTERIM). Figure 2.4 presents the statistical coherence between grace and the atmospheric time series for the largest 13 basins with available discharge data or nonexistent discharge. In general, with spatial smoothing of the atmospheric fields, a gain in coherence with grace is observed. However, for some basins, the effect of spatial filtering is negligible. These basins are characterized by a desert climate

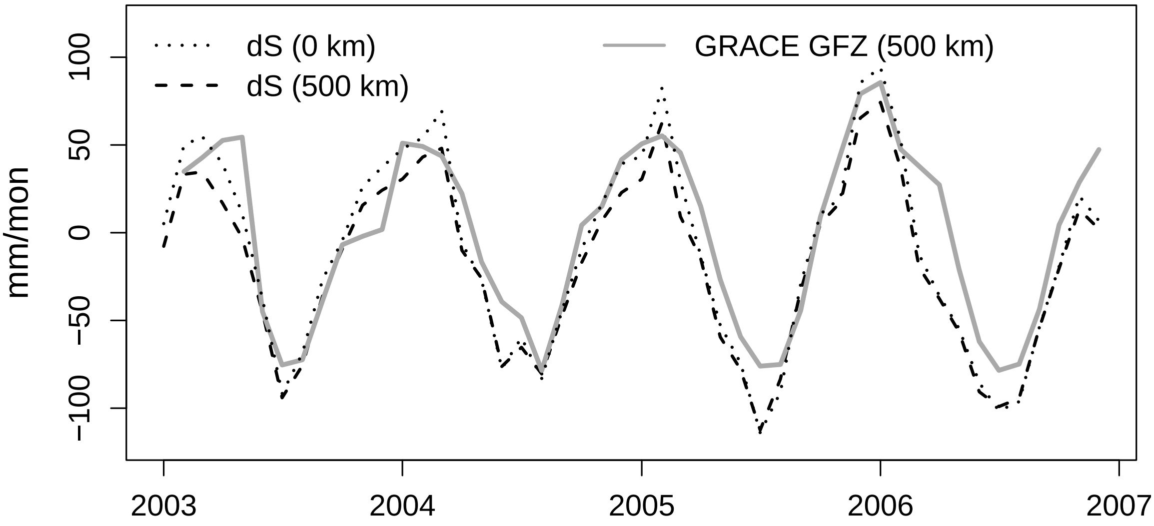

Figure 2.3.: Storage change $\nabla \cdot \vec{Q} - R$ (ECMWF ERA-INTERIM) for the Amazonian basin. No smoothing (dotted) and 500 km Gaussian filter (dashed)

and thus low water storage change rates. For an explanation of the Taylor diagram depiction it is referred to section 2.7.3.

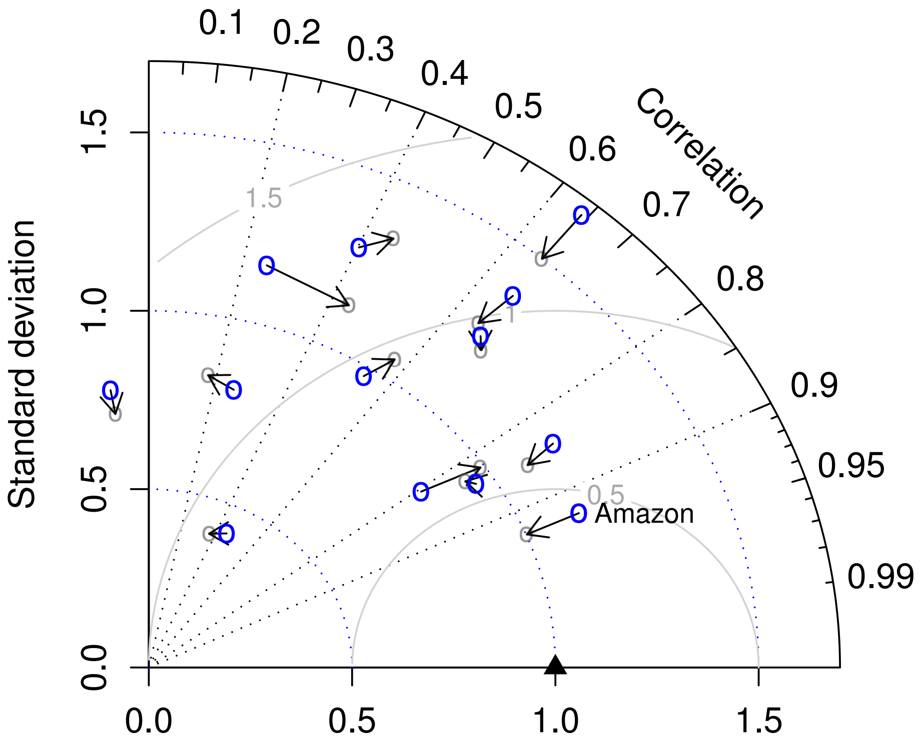

Figure 2.4.: Normalized Taylor diagram of unfiltered (open circles) and 500 km smoothed (arrowhead) $\nabla \cdot \vec{Q} - D$ (ECMWF ERA-INTERIM) versus GRACE GFZ RL04 500 km, de-correlated (baseline triangle).

Fringe or leakage effect By applying spatial smoothing, the border of a region becomes blunted. Hence, processes outside a well defined basin may effect the total balance inside (Swenson *et al.* , 2003; Rodell *et al.* , 2004). Figure 2.5 illustrates this relation. The radius

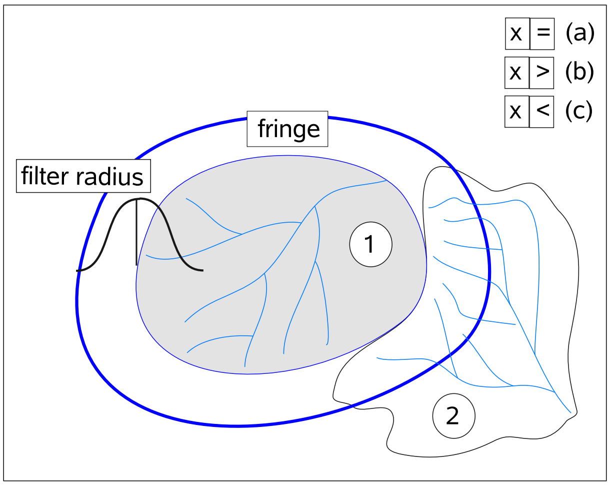

Figure 2.5.: Fringe effect, caused by Gaussian spatial smoothing.

of the spatial filter determines the fringe-width of a river basin (1). Three different modes can be identified for the configuration of basin and fringe zone. Related to the basin inside, this is equality (a) and higher (b) or lower (c) amounts in the fringe. Mode (a) causes no alteration of the mean basin value. A gradient from basin (2) to basin (1) results in a positive bias (b) and vice versa. Depending on how the different modes are distributed along the border line, the overall fringe effect will be positive, neutral or negative. If basin aggregated time series are considered, the ratio between the basin size and the filter radius determines the strength of the leakage effect.

Leakage effects are also obtained for coastal regions. Especially locations with small water mass variation like e.g. Australia are influenced by tides of the adjacent ocean areas. Awange *et al.* (2009) found that the leakage error was significantly reduced in release 4 of the CSR GRACE solutions. But it is also stated that the de-aliasing of ocean tides is still not perfect.

Numerical differentiation The monthly GRACE solutions contain the mass deviations from a long term reference field. Monthly change rates for the terrestrial water storage variations are therefore obtained as time derivatives of the monthly state fields. For this study, the central difference approach is used:

$$\dot{m} = \frac{dM}{dt} \approx \frac{f(t+\Delta t) - f(t-\Delta t)}{2\Delta t} \tag{2.6}$$

At the beginning or end of a time series or if missing values are contained, the change rates are computed accordingly with the forward- or backward difference method

$$\dot{m} = \frac{dM}{dt} \approx \frac{f(t+\Delta t) - f(t)}{\Delta t} \tag{2.7}$$

$$\dot{m} = \frac{dM}{dt} \approx \frac{f(t) - f(t-\Delta t)}{\Delta t} \tag{2.8}$$

2.7. Analysis

2.7.1. Study Design

The evaluation of atmospheric water budgets with GRACE solutions requires to investigate the reasonableness of the different global and regional atmospheric products and to prove by a validation with independent observations. Figure 2.6 gives an overview on the concept of validation and evaluation that is applied for this study.

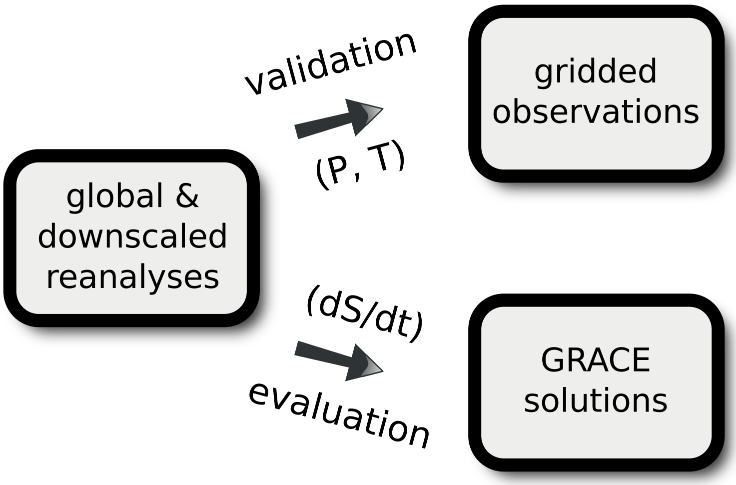

Figure 2.6.: Study structure overview

For validation, gridded observations of precipitation and temperature are used. The comparison comprises spatial deviation patterns and basin aggregated time series. For the spatial pattern analysis, deviation maps of annual statistics are prepared. The statistical coherence for the basin aggregated time series is investigated with Taylor diagrams and bias tables. The methods are described in detail within the following two sections.

The validation allows the identification of reasonable global reanalyses and regional model setups. The verified products, in particular the derived terrestrial water storage variations are then evaluated against the GRACE solutions. This is only possible for the basin aggregated time series because no information about the spatial distribution of runoff is available. The time series for the best performing atmospheric products are plotted along with the GRACE collective of GFZ, CSR, and JPL. Additionally, for all atmospheric water budget time series, the coherence with GRACE is also analyzed using Taylor diagrams and bias tables.

2.7.2. Deviation Maps

For validation, the global and downscaled reanalyses, are compared with independent gridded observation data sets of temperature and precipitation. For this purpose, the gridded fields are transformed onto a 0.5 °× 0.5 ° grid by using the *Climate Data Operators* (CDO) from MPI Hamburg (https://code.zmaw.de/projects/cdo). CRUT and GPCC are taken as reference data set for temperature and precipitation, respectively. For every study domain, the resembling quality of the global and the regional atmospheric fields (x) is investigated by computing and plotting the deviation patterns with regard to the reference data set (r). In terms of precipitation, the difference (y) is computed from the annual sums:

$$y_{i,j} = \sum_{n=1}^{N} r_{i,j,n} - x_{i,j,n} \tag{2.9}$$

for temperature, the annual mean values are considered:

$$\overline{y_{i,j}} = \frac{1}{N} \sum_{n=1}^{N} r_{i,j,n} - x_{i,j,n} \tag{2.10}$$

with i and j denoting the east-west and south-north indexes of the horizontal grid. N stands for the number of months in a year. The resulting deviation maps are plotted using the *Generic Mapping Tools* (GMT), available at (http://gmt.soest.hawaii.edu).

2.7.3. Taylor Diagram

Taylor (2001) proposed a novel diagram type, combining the information in correlation coefficient (R), root mean square error (E), and standard deviation (σ). With this graph, multiple time-series of observed and simulated become easily comparable. The bias corrected root mean square error (E') for a basin aggregated reference (f) and simulation (h) time series is defined with

$$E' = \left\{ \frac{1}{N} \sum_{n=1}^{N} [(f_n - \bar{f}) - (h_n - \bar{h})]^2 \right\}^{1/2} \tag{2.11}$$

can be rewritten as

$$E'^2 = \sigma_f^2 - 2\mathrm{COV}_{f,h} + \sigma_h^2 \tag{2.12}$$

with $\mathrm{COV}_{f,h}$ denoting the covariance of the two time series f and h (Eq. 2.13).

$$\mathrm{COV}_{f,h} = \sigma_f \sigma_h R \tag{2.13}$$

The analogy between equation 2.14 and the law of cosine (Eq. 2.15)

$$E'^2 = \sigma_f^2 + \sigma_h^2 - 2\sigma_f \sigma_h R \tag{2.14}$$

$$c^2 = a^2 + b^2 - 2ab \cos\varphi \tag{2.15}$$

provides the basis for the construction of the *Taylor Diagram*. The triangle in Figure 2.7 visualizes the geometrical relationship among the different statistical measures on a polar graph. The radial distance from the origin attributes to the standard deviation. The reference field is positioned on the abscissa according to its standard deviation (gray filled triangle). The radial position of the related field (gray filled square) is defined by it's standard deviation and the angle of $\cos^{-1}(R)$.

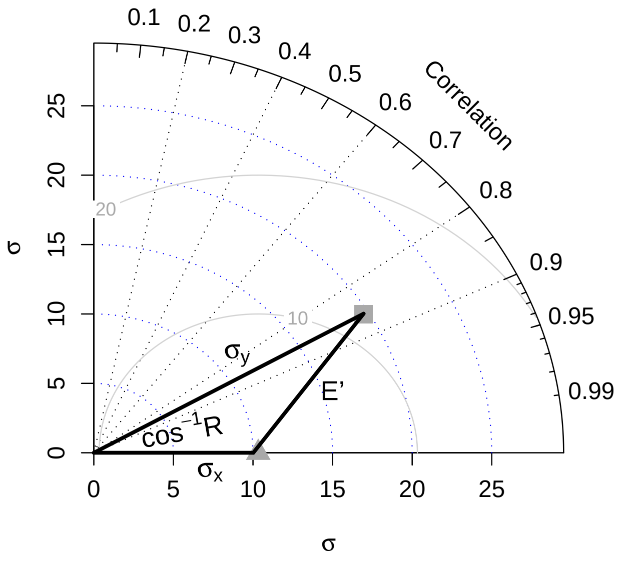

Figure 2.7.: Geometric configuration of a Taylor Diagram.

Here, only the right half of the graph is shown. The left side is needed in the case of anti-correlations where negative angles are obtained. The distance between reference and related field is predefined by the bias corrected root mean square error ((E')). The gray arcs in the graph mark the equidistances of (E') having the same unit as σ. A model, well resembling the reference values, minimizes the length of (E') and shares the same standard deviation radius.

2.7.4. Climate Diagrams

In the following chapters the four selected study domains are introduced and a short overview on the climatic characteristics is given. For that purpose, a number of climate diagrams are prepared for every domain, according to the methodology of Walter & Lieth. However, the monthly mean values are derived from gridded observations data sets instead of real station values. CRUT and GPCC are taken for the derivation of the climatic (1961-1990) means for temperature and precipitation. Thus, for a particular station or location, the climate diagrams depict respective pixel values of the gridded observations. The climate diagrams contain the elevation above sea level, and the annual mean temperature and precipitation. Temperature minimum and maximum is printed left of the °C axis. Figure 2.8 provides an example for the climate diagrams that are used in this study.

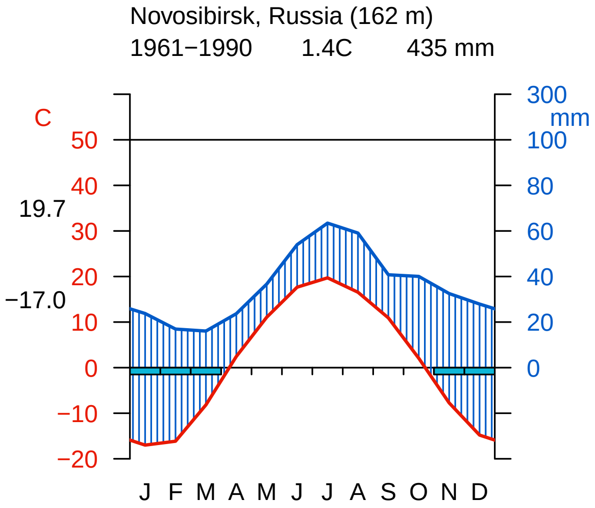

Figure 2.8.: Climate diagram for Novosibirsk

3

Siberian domain

Large areas of the northern hemisphere are characterized by a cold and humid climate. On the American continent, this zone belongs to the territories of Canada and Alaska. For Asia, Russia covers the biggest part. The Siberian domain encompasses the three river catchments of Ob, Yenisei, and Lena. It represents climatic conditions where the hydrological regime is controlled by snow and ice for at least two thirds of the year.

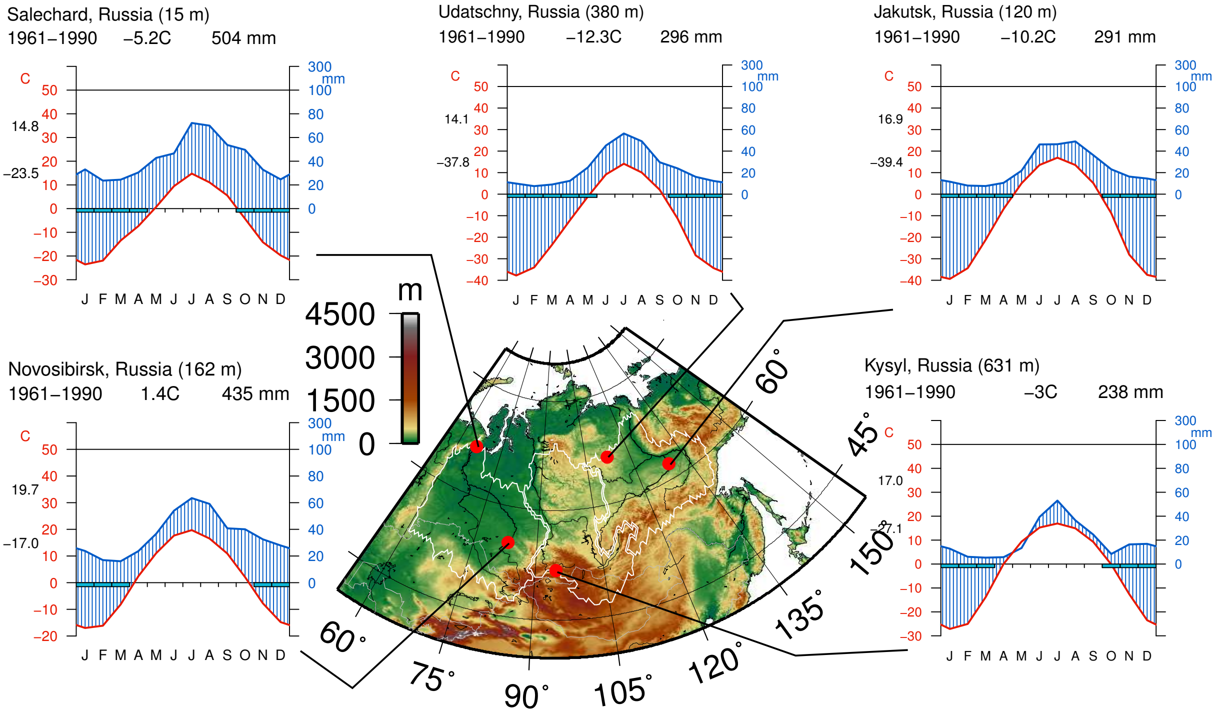

Figure 3.1.: Domain configuration and climate diagrams. River basins (in left to right order): Ob, Yenisei, and Lena.

3.1. Domain Characteristics

Climate The climate diagrams in figure 3.1, visualize the annual variations but also the spatial gradients of temperature and precipitation. According to Köppen–Geiger, the region has a fully humid snow climate with a cool summer (Kottek *et al.* , 2006). The annual mean temperature decreases from west to east along the South Siberian Mountains, and from south to north with typical values of +2 °C to -15 °C and minimum monthly means of -15 °C to -40 °C. In the warmest summer months, about 14 °C to 20 °C can be reached. The precipitation gradient is directed to the opposite with higher amounts in the northwest and dryer conditions in the south west with annual sums between 200 and 500 mm.

Hydrometeorology In winter, typically from October until March, the atmospheric state over the northern Asian continent is dominated by the Siberian Anticyclone. According to (Sahsamanoglou *et al.* , 1991) the center position of this cold high varies within the region of 90°E–11°E and 40°N–55°N. Patterns of temperature and precipitation are closely related to the strength of the Siberian High. With increasing distance to the center, this coherence becomes weaker Gong & Ho (2002).

Numaguti (1999) found that, in winter, most of the precipitating water of northern Eurasia is supplied by evaporation from the Atlantic Ocean. Summer rainfall has its main source in easterly transport of continental evapotranspiration. The annual precipitation sums are narrow with 500 mm in the west and only 200 mm in the southeast, with around 60% falling in summer (May–September). The maximum is usually experienced in July. Winter precipitating is almost constant ranging between 30 mm month^{-1} in the west and 10 mm month^{-1} in the east.

River basins For the Siberian study region, the two river catchments of Yenisei and Lena are combined in order to cover a spatial extent that is comparable to the Amazon river basin. Together with the Ob, the rivers form the largest tributaries to the arctic ocean (Berezovskaya *et al.* , 2004). Their contribution to the total freshwater input into the arctic ocean is about 46%.

For Yenisei, the gauge Igarka is selected from the GRDC database. Until here, the river is accessible by ocean vessels. The length of the upstream mainstem is 4,337 km. The distance towards the Arctic Ocean is 525 km. At the river mouth, the Yenisei drains an area of 2,580,000 km^2. At Igarka the catchment size reduces to 2,413,479 km^2. The mean annual station runoff is 236 mm and the average discharge rate is 18,050 m^3 s^{-1}. In winter, the flow decreases to 3,120 m^3 s^{-1}. The maximum values are measured during the snow melt season with a mean value of 112,000 m^3 s^{-1} (Fekete *et al.* , 2000).

The Lena catchment adjoins the eastern boundary of the Yenisei basin and covers an area of 2,500,000 km^2. The last station with available data from GRDC is Kyusur, located 150 km before the estuary. The station accounts for an area of 2,430,000 km^2. Additional meta data is missing for this station. Therefore, information from the nearby gauge Stolb is considered. This station is available in Fekete *et al.* (2000). At Stolb, the length of the upstream mainstem is 4,329 km. In compliance with the west-eastern gradient in precipitation, with 198 mm the annual runoff term is smaller than for the Yenisei. The experienced average rates of discharge are 15,000 m^3 s^{-1}, 927 m^3 s^{-1}, and 85,880 m^3 s^{-1}, for normal flow, winter conditions, and the snow melting period, respectively.

From Mai to June, snow and ice begin their melting in the southern basin regions. The river ice breaks into floes and floats towards the still frozen regions of the north. This often leads to severe congestion where the rivers are still frozen. During congestion events the discharge measurements are often inaccurate. Knowledge about this process is required to explain some irregularities in the discharge data. For Lena and Yenisei, the influence of ice congestion is usually seen in June.

3.2. Validation

Orography The spatial patterns (fig. 3.2) of elevation are very similar for the global reanalyses and WRF. Differences occur at the coastlines. The ocean area of NNRP is smaller than for the others and the maximum heights are also slightly decreased. Nevertheless, the main formations of the South Siberian Mountains are well resembled by any of the three fields. The peaks of the Altai and the Celestial Mountains mark the highest positions of the domain with heights exceeding 4,500 and 7,000 m, respectively. WRF, NNRP and INTERIM show maximum elevations of 3,000-4,000 m for those regions.

Precipitation Over the Siberian domain, the GPCC station network is well distributed with an acceptable density (fig. 3.3). For 2005, the spatial patterns of the accumulated precipitation of GPCC are in good agreement with the climate diagrams of figure 3.1. The comparison with CRUP and DELP shows significant deviations for the northeastern regions where both products suggest lower annual sums by an average of 200 to 300 mm. As distinct from CRUP and DELP, GPCP is very close to the observations of GPCC.

The two global reanalysis fields of NNRP and INTERIM contain some differences in their spatial patterns. With respect to GPCC, INTERIM suggests increased precipitation values for the upper basins of Lena and Yenisei. The high values that GPCC observes for the northwestern parts of the domain is not resembled by the reanalysis models. Furthermore, NNRP overestimates precipitation throughout the three river catchments by 100 to 300 mm.

For DELP and CRUP no information about the station network density is available. As GPCC has a rather dense observation network, and because GPCP uses additional information from remote sensing, it is assumed that, for the arctic region, the two fields are more reliable than the gridded data sets of CRUP and DELP. Furthermore, the spatial patterns of the reanalysis fields support this assumption because they do not agree with CRUP and DELP in terms of reduced precipitation over the eastern part of the domain.

Figure 3.4 visualizes the differences in spatial precipitation patterns for the regional simulations. At first appearance, all fields turn out to be very similar. For the Ob catchment, WRF suggests lower values than actually observed. Along the eastern coastline, wetter conditions are seen. For the catchments of Lena and Yenisei less deviation is experienced with respect to GPCC. The strongest effect is seen for the SST switch. NR KF SST const. and EI KF SST const. lead to dryer conditions along the eastern coastline. Here, the NNRP driven simulation is stronger affected than the one driven by ERA-INTERIM. However, for 2004 (not shown), EI KF SST const. yields much wetter conditions, compared to the observations. Thus, the SST setting can either lead to dryer or wetter conditions. In general, it affects mainly the southeastern region of the domain but also parts of the basins of Lena and Yenisei.

For the mountainous regions in the southern part of the domain, all regional simulations conclude with wetter conditions than observed by the global data sets. In general, the EI runs are dryer in the southwest than the corresponding NR runs. Compared to the Ob catchment, for Lena and Yenisei the deviations from GPCC are marginal. Furthermore, the variations for the different regional simulations mainly occur outside these regions.

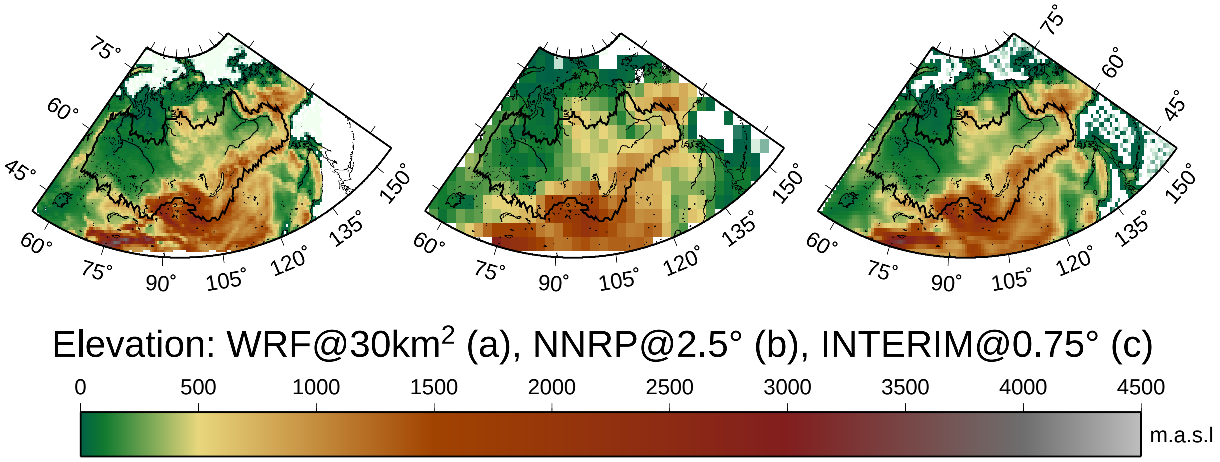

Figure 3.2.: Siberian domain: DEM configuration for WRF (a) and the reanalysis models of NCAR/NCEP (b) and ECMWF ERA-INTERIM (c).

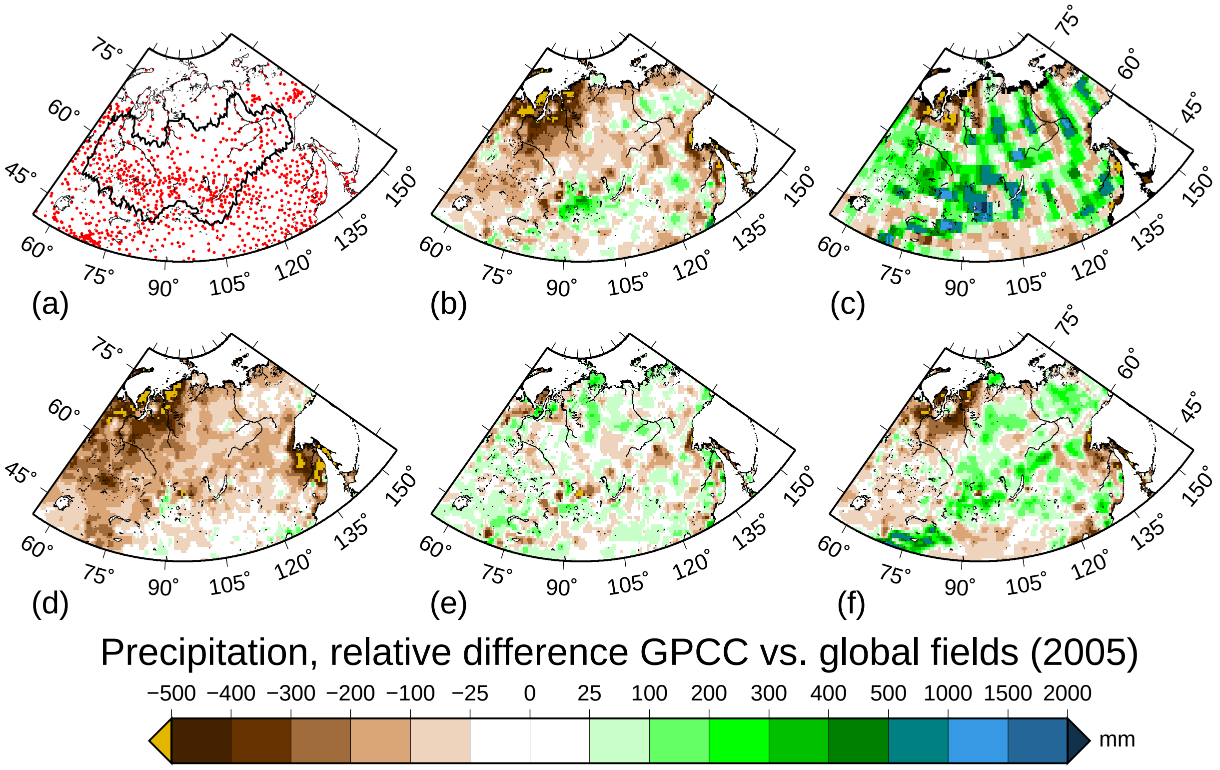

Figure 3.3.: Siberian domain: relative difference in annual precipitation observations and global reanalyses with respect to GPCC. (a) GPCC Station network, (b) CRUP, (c) NNRP, (d) DELP, (e) GPCP, (f) INTERIM.

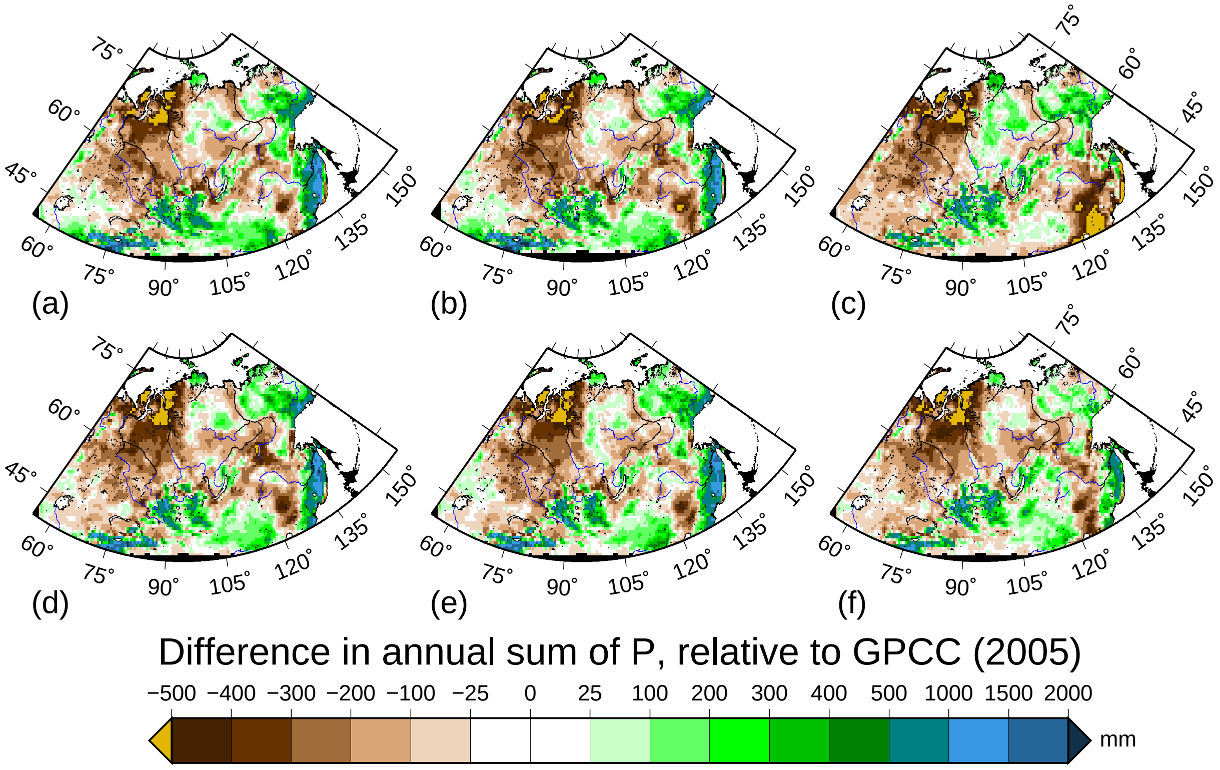

Figure 3.4.: Siberian domain: deviation in annual precipitation of downscaled reanalyses with respect to GPCC. (a) NR SST+KF , (b) NR SST+KF+FDDA, (c) NR KF SST const., (d) EI SST+KF, (e) EI SST+KF+FDDA, (f) EI KF SST const.

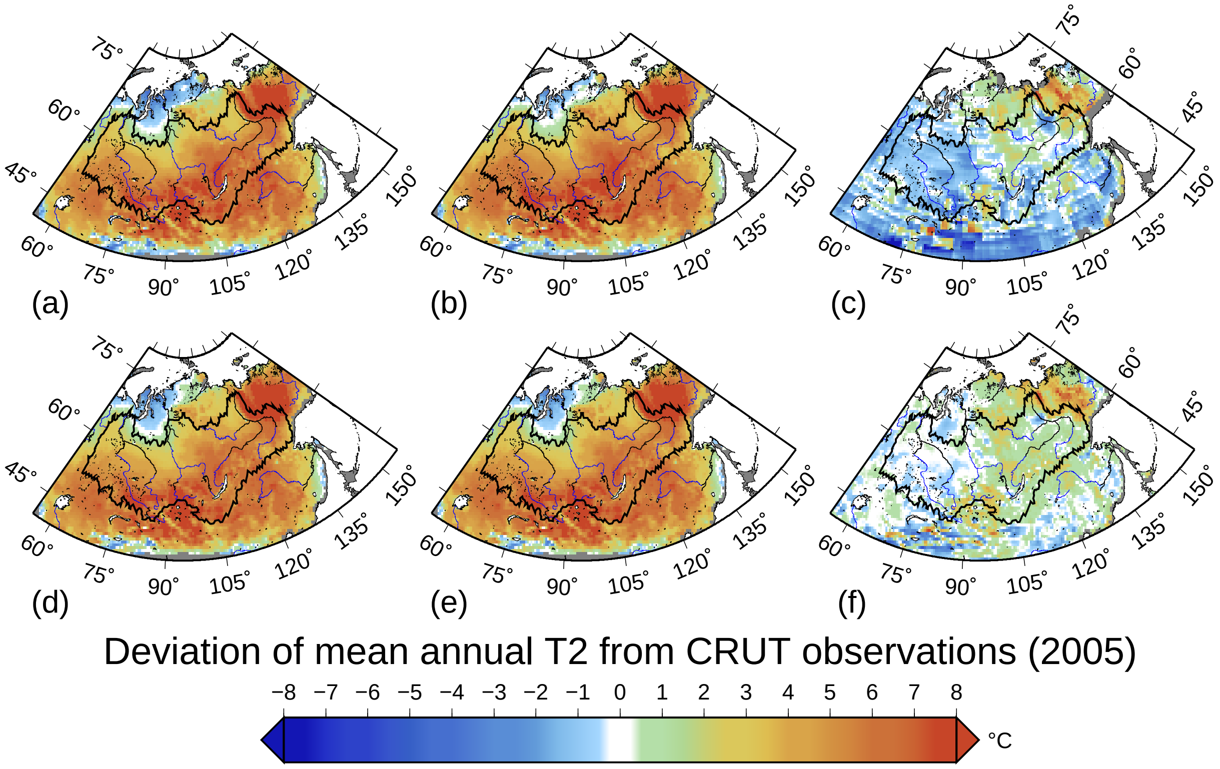

Figure 3.5.: Siberian domain: relative differences in annual mean 2m-temperature of downscaled reanalyses with respect to CRUT. (a) NR SST+KF , (b) NR SST+KF+FDDA, (c) NNRP, (d) EI SST+KF, (e) EI SST+KF+FDDA, (f) ERA-INTERIM.

The comparison of the basin averaged time series reveals a good performance of the global INTERIM field. Summer peaks are slightly overestimated, leading to a total bias of 5 mm month^{-1}. NNRP also resembles the seasonality reasonably but contains a positive bias that ranges from 10 to 50 mm month^{-1} for winter and summer, respectively (tab. 3.1). In the Taylor Diagram (fig. 3.6) INTERIM marks the best position with relation to the observations. NNRP is well correlated to GPCC, mainly because of the seasonal signal variation.

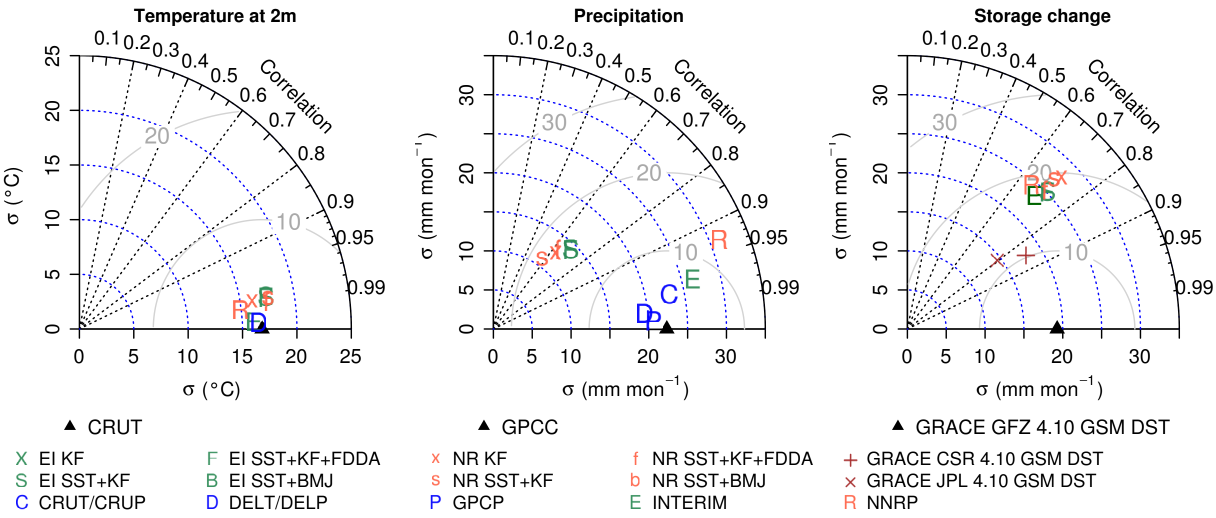

Figure 3.6.: Siberian basin: Taylor diagram for 2m temperature, precipitation, and water storage change.

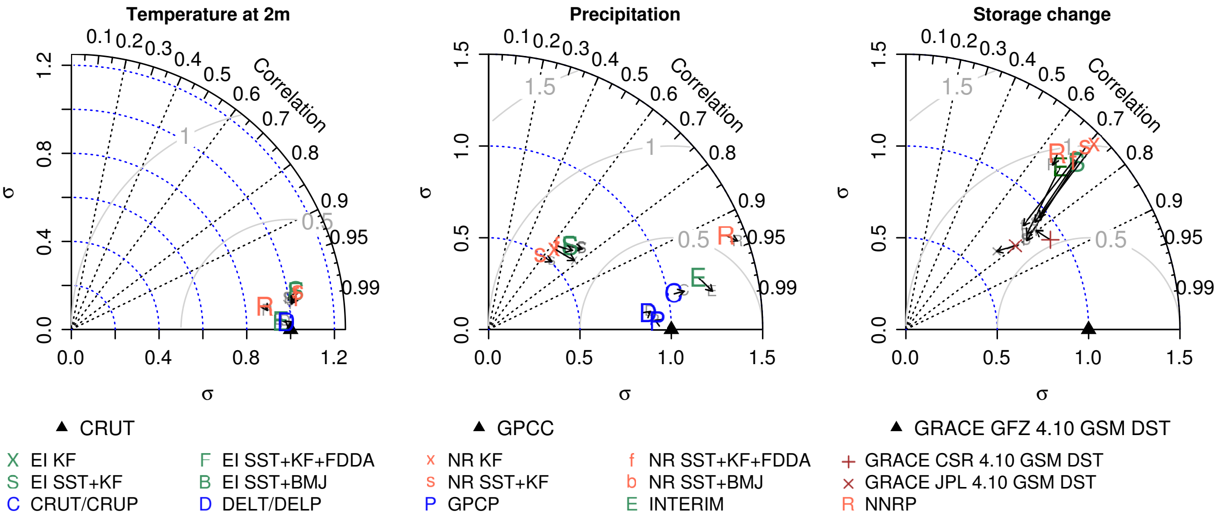

Figure 3.7.: Siberian basin: Taylor diagram for 2m temperature, precipitation, and storage change. Arrows show improvement if only considering the periods from July to January

The WRF simulations tend to cut off the peak in summer rainfall. In return, for the February to June period an increase is experienced. During fall and early winter, GPCC is very well resembled by each of the regional model runs. EI KF+SST, EI KF SST const., and NR KF SST const. leads to an elevated amount of summer precipitation. Gridded nudging (+FDDA) does not bring any improvement over the KF+SST mode.

Altogether, it is difficult to isolate a particular configuration of the regional model that outperforms all others. In terms of temporal correlation, EI driving causes a very little improvement towards NR. This applies also for the standard deviation. Nevertheless, the time series of the global INTERIM reanalysis performs best.

Table 3.1.: Siberian basin: bias for monthly time series of precipitation (mm month^{-1}), temperature (°C), and storage change (GRACE GFZ RL 04, mm month^{-1}) (2003/01 – 2006/12). Gridded observation data versus global reanalyses and regional simulations.

	CRUP	GPCC	GPCP	DELP	CRUT	DELT	GRACE
INTERIM	10.02	4.80	6.09	13.71	1.16	1.21	−4.54
EI SST+KF	4.77	−0.45	0.85	8.47	5.23	5.28	−5.90
EI SST+KF+FDDA	4.77	−0.45	0.85	8.47	5.23	5.28	−5.90
NNRP	22.89	17.67	18.97	26.59	0.44	0.49	−6.92
NR KF	8.36	3.14	4.44	12.05	6.46	6.51	−7.53
NR SST+KF	1.88	−3.34	−2.04	5.58	5.26	5.31	−8.17
NR SST+KF+FDDA	3.46	−1.76	−0.47	7.15	5.28	5.33	−7.42

2 meter temperature In figure 3.5, the deviations from CRUT 2005 mean annual temperature are presented for four different regional simulations and for the global fields of NNRP and INTERIM. A significant mean annual warm bias is experienced from all the WRF model runs (tab. 3.1). In contrast, the global fields seem to be more closely related to CRUT. Despite the bias, the spatial deviation patterns are very similar for the regional and the global fields. Between the catchments of Ob and Yenisei, the models suggest a larger temperature gradient than it is observed with CRUT.

By looking at the time series, it is found that the deviations do not persist over the whole annual cycle. The largest differences with the regional simulations occur at the extremes of summer and winter with up to +10 °C. The transition periods in between are reasonably resembled. Systematic deviation are also seen for the global reanalyses. NNRP underestimates spring temperatures with up to four degrees and during winter a bias of +5 °C is observed. INTERIM contains a similar seasonal bias dependence. However, the deviations are smaller than for NNRP. During summer a peak bias of 0.5 °C is observed. In winter this value increases up to 2.5 °C. In general can be stated that INTERIM performs best in the spatio temporal comparison. According to the Taylor Diagram (3.6), model and observations show a close coherence. However, it must be noticed that the mean bias is not contained in this depiction.

3.3. Water Storage Variations

Model comparison For the combined catchments of Yenisei and Lena, the model uncertainty in water storage variations is significantly smaller than for the Amazon river (fig. 3.8). Especially the results of the regional atmospheric model are very uniform. If different model driving data or different model configurations are used, only minor variations in the time series are seen. Contrarily, the storage variations derived from global fields of moisture flux convergence show a much higher range. Especially, for the August to October months, NNRP suggests elevated amounts of storage depletion with respect to INTERIM.

The span of the three different GRACE solutions (CSR, GFZ, JPL) varies over time between 10 and 40 mm month^{-1}. The satellite observations are well resembled by the global and regional atmospheric models. However, for some periods GRACE suggest smaller diminishing rates. For the winter season of 2005 and 2006, the different atmospheric models lead to a smaller uncertainty width than GRACE. The large negative peaks in the time series of WRF and the global reanalyses are likely caused by uncertainties in the GRDC discharge data because of high water levels and ice induced congestion effects. Therefore, in this case, the observations of GRACE should be more reliable.

For Yenisei and Lena, spatial smoothing has no significant effect on the atmosphere-derived water storage variations. In figure 3.9, the time series of INTERIM and EI SST+KF and their respective filtered equivalents are shown. The differences turn out to be marginal.

Reasonable models Different to the Amazonian study area, the analysis for the combined river catchments of Yenisei and Lena does not lead to a distinct conclusion in terms of identifying an outperforming atmospheric model. For the global reanalyses, the validation with observations of temperature and precipitation is promising. However, the Taylor depiction (fig. 3.6) reveals that this does not apply to the water storage dynamics. Both, global fields and regional simulations, show an equal performance. Errors in the GRDC discharge data could be one explanation for the reduced correlation coefficient.

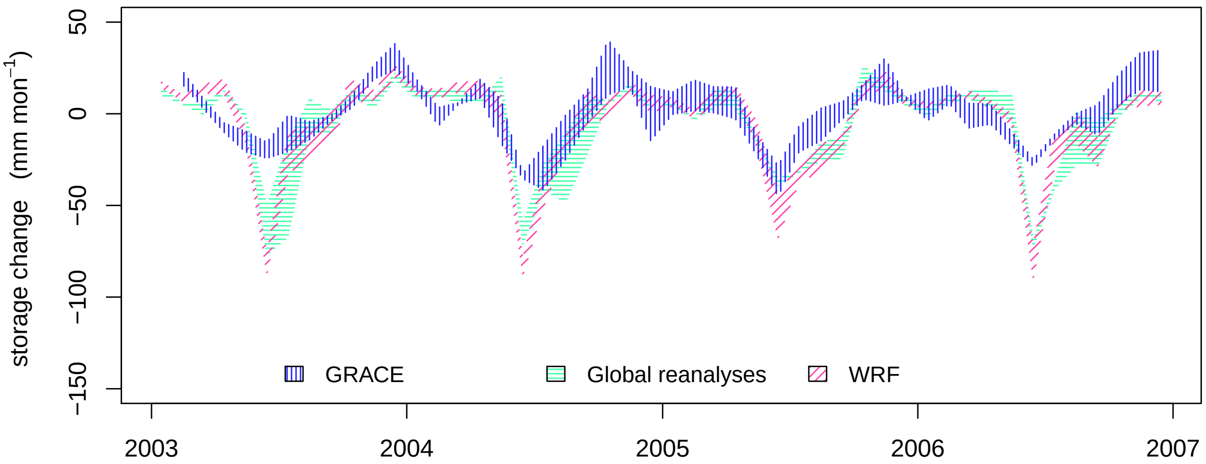

Figure 3.8.: Siberian basin: total uncertainties in basin water storage change, derived from GRACE (GFZ, CSR, JPL, release 4, Swenson & Wahr (2006) de-striping filter & 500 km Gaussian smoothing applied), global reanalysis (INTERIM, NNRP), and WRF. All atmospheric fields of $-\nabla \cdot \vec{Q}$ are smoothed by a 500 km Gaussian filter.

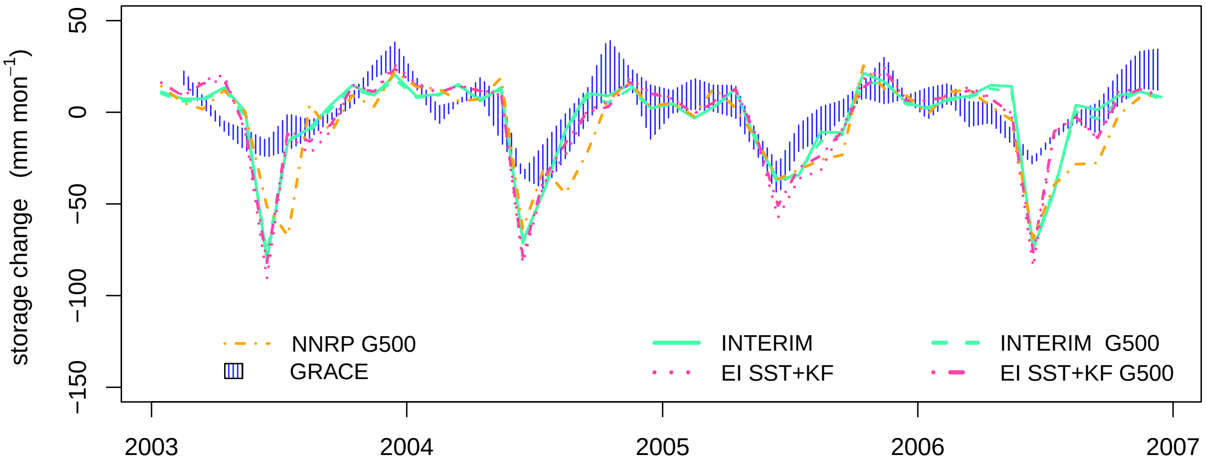

Figure 3.9.: Siberian basin: water storage variations and most reasonable global and regional atmospheric models.

In terms of storage variations, another important finding is that for the Siberian domain, WRF is not very sensitive to different driving data. The model configuration turns out to have a much larger effect on the resulting time series.

In figure 3.9, for the late summer to early winter times, global NNRP shows the largest departure from GRACE. All regional NR simulations depart from that global line and incline to the curves of EI. Hence the quality of NNRP could be questioned for those specific periods. By following that assumption, INTERIM would be the best performing global model. For the regional simulations, all of the catchment aggregated time series show similar quality.

Seasonal performance If only the July to January periods of the time series are considered, the storage variations derived from global atmospheric fields and dynamic downscaling show maximum correlations with the GRACE solutions. The visualization in the Taylor Diagram (fig. 3.7) illustrates the differences between the whole time series and the chosen subset. With this configuration, the atmospheric approach lies within the uncertainty bounds of the three different GRACE solutions. Contrarily, for precipitation, the changes in correlation are only small. For the 2-meter temperature almost no effects are seen. The fact that the inclusion of the months March to June results with the weakest correlation measures corroborates the assumption that the discharge data is erroneous for those specific times. If it was the evapotranspiration that causes an imbalance in the atmospheric water budgets, it would be likely that the effects persist also for the summer and fall season.

Different to the WRF runs and INTERIM, for NNRP the correlation increases only little. NNRP agrees best with GRACE ($r = 0.77$) if only the June to December months are considered. Nevertheless, from December to May, all time series of atmosphere derived water storage variations are very similar with smaller uncertainty bounds than the GRACE observations.

3.4. Performance of the Regionalization

For the Siberian study region, it is concluded that with dynamical downscaling, the positive bias in annual precipitation of the global reanalyses can be significantly reduced. However, the maximums of summer precipitation do not always resemble the global observations. In terms of temperature, the regional model shows strong deviations of up to +10 °C. These deviations occur regardless of the tested model configuration. However, the observed bias follows a certain periodicity with a maximum every summer and winter. The deviations in 2m-temperature do not seem to have a strong influence on the water budget. During winter the temperatures remain below the freezing point. Thus evapotranspiration is not affected. The peak values of monthly precipitation are smaller with the regional simulation. Altogether, the dynamic downscaling adds value to the global fields by mainly improving the precipitation bias with respect to the gridded observation data. This effect becomes much more pronounced for the NNRP simulation.

4

North African domain

The North African domain encompasses the Saharan desert and includes the Lake Chad watershed, and the river catchments of Niger, Nile, Senegal, and Volta. Unfortunately, for the large rivers, discharge data is laking. Volta and Senegal are too small for a comparison with GRACE. Therefore, this study region is selected to address hot arid climates. The borders of the considered area are selected in a way that all runoff flows to the inside. Hence, the discharge term of the water balance equation becomes zero and the atmospheric water budgets are directly comparable to GRACE.

The same principle is applicable to the enclosed basin of Lake Chad. Except for atmospheric exchange, all incoming water remains within the topographically defined boundaries and discharge is therefore defined to be zero.

4.1. Domain characteristics

Climate The North African domain encompasses a large range of climatic zones. In terms of the Köppen–Geiger classification (Kottek *et al.* , 2006), the northern part is dominated by hot arid desert (BWh). Between 15 and 10 °C N, the characteristics change to steppe (BSh). The regions further south are influenced by the Intertropical Convergence Zone (ITCZ) which causes summer precipitation. Therefore these regions are defined as equatorial winter dry (Aw). Along the southern and south-western coast this period of rainfall gets prolonged because the monsoon (Am).

In figure 4.1 the domain's spatial extent is depicted. The climate diagrams represent the various climatic characteristics, ranging from hot arid desert (Algeria, Libya) and winter dry (Chad) to monsoonal (Lagos) conditions. The seasonal variation in air temperature is strong for the desert locations. Towards the equator the monthly mean values converge towards the annual average.

Hydrometeorology In Western Africa and the in the Central regions like Chad, Sudan, and Nigeria, precipitation is strongly connected to the ITCZ. The African Easterly Jet (AEJ) causes westward propagating disturbances that generate convective precipitation. The intensity and location of these systems varies from year to year (Nicholson & Grist, 2003). Along this rainbelt,

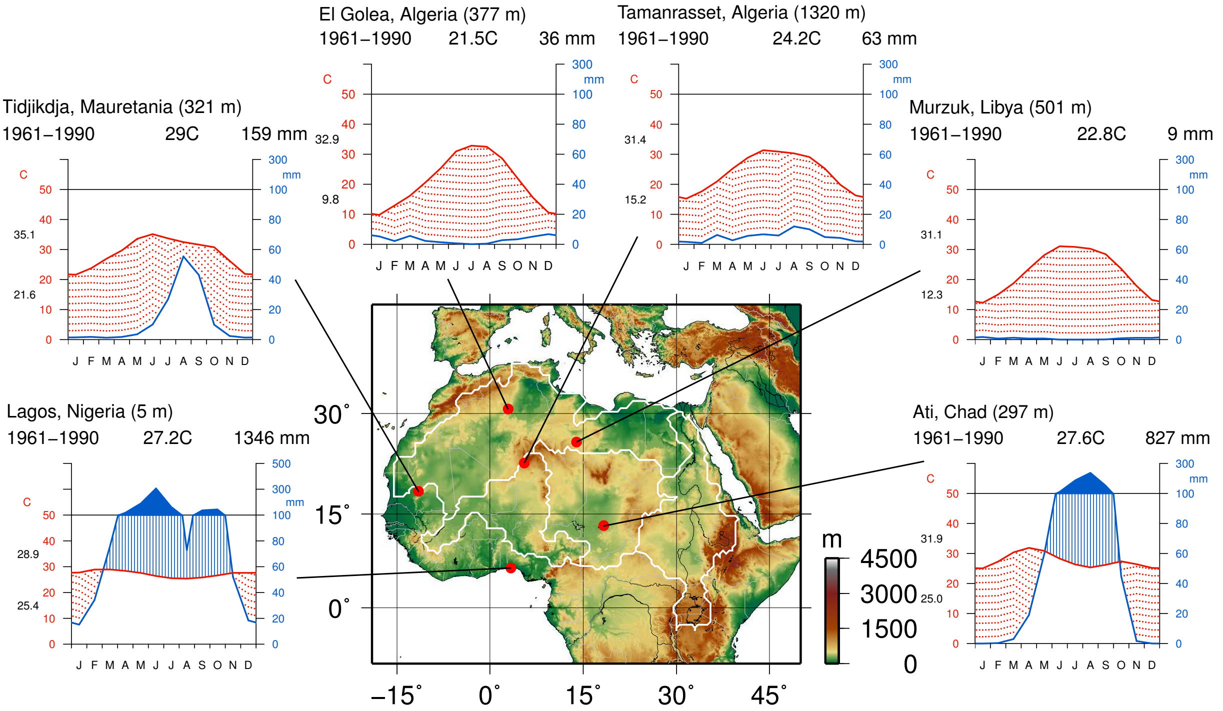

Figure 4.1.: Domain configuration and climate diagrams. Basins (left to right order): Sahara, Niger, Lake Chad, and Nile.

the annual sums of rainfall range from 400 to 1500 mm. At some parts of the southern coastline of West Africa, these values can rise to 3000 mm and above to due to the monsoon.

Winter precipitation that occurs along the Mediterranean reaches values between 200 and 700 mm yr^{-1} with a strongly decreasing inland gradient. In the Saharan desert, the mean values of annual precipitation range from zero to about 60 mm (Tamanrasset, Algeria).

Study areas The Saharan study extent is confined by its surrounding topographical watershed. By this definition, no water leaves the region and therefore the discharge term of the water balance equation (1.1) is set to zero. The size of the selected area is 5,271,752 km^2, comparable to the Amazon basin ($\approx$ 4,650,000 km^2) and the combined river catchments of Yenisei and Lena ($\approx$ 4,950,000 km^2).

The Chad depression covers about 2,400,000 km^2 and is the largest inland drainage area of the African continent. The Lake Chad covers 1,350 km^2. The Chari river is the most important tributary. It is responsible for 95% of the inflow. It delivers water from the southeastern part of the basin, where precipitation is proportionally high. No water leaves the boundary of the basin. Hence, net precipitation (P-E) is always proportional with the water storage change, and the discharge term in (eq. 1.1) can be assigned with zero.

The Niger has a length of almost 4,200 km and drains a total area of around 2,260,000 km^2. The last gauging station with available discharge data is located at Lokoja, a small town at the confluence with its major tributary, the Benue River. The Lokoja station accounts for 2,078,000 km^2 of the catchment area. The recorded mean values for discharge volume and height are 5,094 m^3 s^{-1}and 77 mm yr^{-1}, respectively. Mean peak discharge is about 13,624 m^3 s^{-1} and mean low flow 1,837 m^3 s^{-1}. Monthly data from GRDC is available for the years 1975 to 2006.

The modeling domain covers also the river basins of the Nile ($\approx$ 3,050,400 km^2), the Niger ($\approx$ 2,100,500 km^2), and the Senegal ($\approx$ 417,107 km^2). For the Nile no discharge data is available.

The Kongo river is not totally covered by the regional simulation. And the remaining major rivers are too small for an evaluation with GRACE (see also tab. B.1).

4.2. Global Validation

Topography Figure 4.2 illustrates how the different models represent the elevation. The height field of WRF gives a good representation of the coastlines and orographic structure. ECMWF INTERIM also contains the important features like the ridge of Atlas, and the Ahaggar and Tibesti mountains. With NNRP, the terrain becomes significantly smoothed, e.g. for the Atlas ridge the peak values are reduced by about 1000 m. Almost all cells of the Mediterranean Sea exceed the sea level. The West African coastline is coarsely represented, especially at the Canaries.

Precipitation In figure 4.3 the deviations in the annual amount of precipitation from different observation data sets are presented. The GPCC station network plot (a) reveals large gaps for the arid regions between 15 ° N and 30 ° N. For the Sahara, the differences are comparatively small among the gridded observations. GPCP has 25 to 100 mm higher values in the eastern part. CRUP suggests dryer conditions with an order of 25 to 100 mm. Towards the south, the deviations become more distinct. Especially along the southwestern coastline, differences of ±500 mm are found. For the central humid region (5 ° N, 30 ° E), GPCC shows a 500 mm higher values, compared to the three other data sets. The relative uncertainties are very high for the Sahara because the total values are very small.

The deviation patterns are more structured for the global reanalysis fields. Both, NNRP (c) and INTERIM (f) simulate dryer conditions for the desert and the Sahel zone. For the basins of Niger and Chad, annual precipitation is up to 500 m lower than observed by GPCC. For the southwestern coastal regions and for the Kongo basin rainfall is vastly overestimated. The deviations occur over large areas and reach 1500 mm and above, at some locations. NNRP appears to be dryer at the Kongo region.

Figure 4.4 visualizes the deviation pattern in annual precipitation for the regional simulations. No runs with invariant sea surface temperature were computed. With this configuration, numerical stability could not be achieved. Instead, the maps for the Betts-Miller-Janjic (BMJ) cumulus parametrization are presented (c,f).

At a first glance, all simulations share the same distinctive features. The 15 ° N line divides an area of strong deviations in the south (blue colors) and an area of moderate deviations in the north (green colors). Remarkably lower values are obtained for the eastern equatorial regions. All SST+KF simulations result in a wet bias. For the Sahara, over large areas, the values are 25 to 300 mm higher than observed by GPCC. South of 15 ° N, 1000 to 2000 mm overestimation is obtained. Over the Kongo river basin the values are further exceed. In contrast with the results of the Amazonian domain, the gridded nudging option (FDDA) leads to an increase in annual precipitation amounts. For SST+KF and SST+KF+FDDA, the resulting conditions are a bit dryer when NNRP driving is used with the regional model. However, the relative uncertainty is rather high for the Sahara where the annual amounts remain usually below 10 to 60 mm.

With NNRP and ERA INTERIM model driving, the SST+BMJ configuration leads to more reasonable results compared to GPCC, especially for the Sahara region. At many locations, the deviations lie within a range of ±25 mm. In the western part, a slight dry tendency is experienced. Furthermore, compared to SST+EI, smaller overestimation is also seen, e.g. for the basins of Chad, Niger, and Kongo. Compared to EI SST+BMJ, NR SST+BMJ shows lower

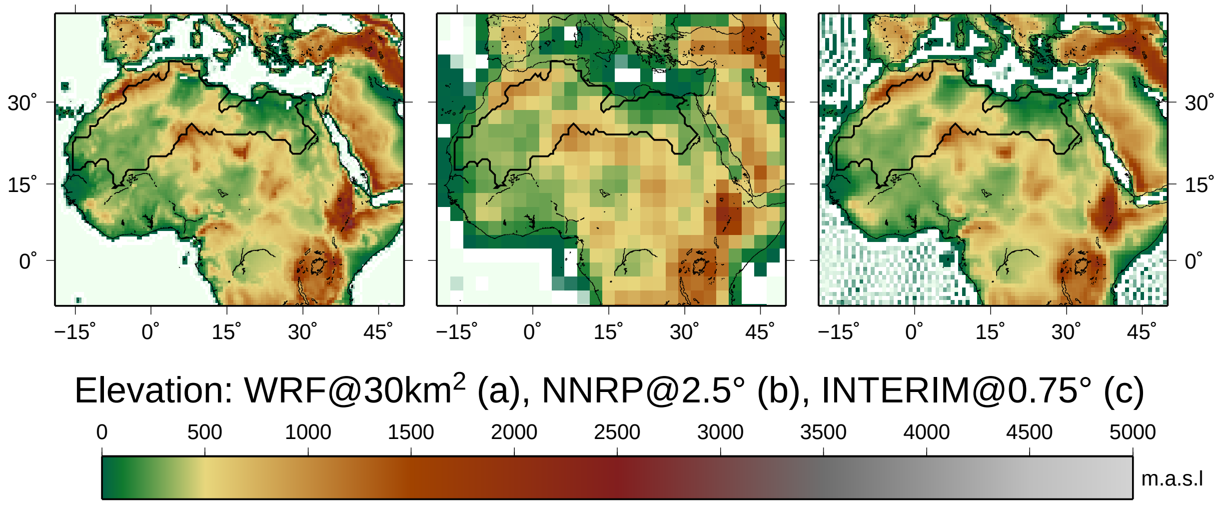

Figure 4.2.: North African domain: DEM configuration for WRF (a) and the reanalysis models of NCAR/NCEP (b) and ECMWF ERA-INTERIM (c).

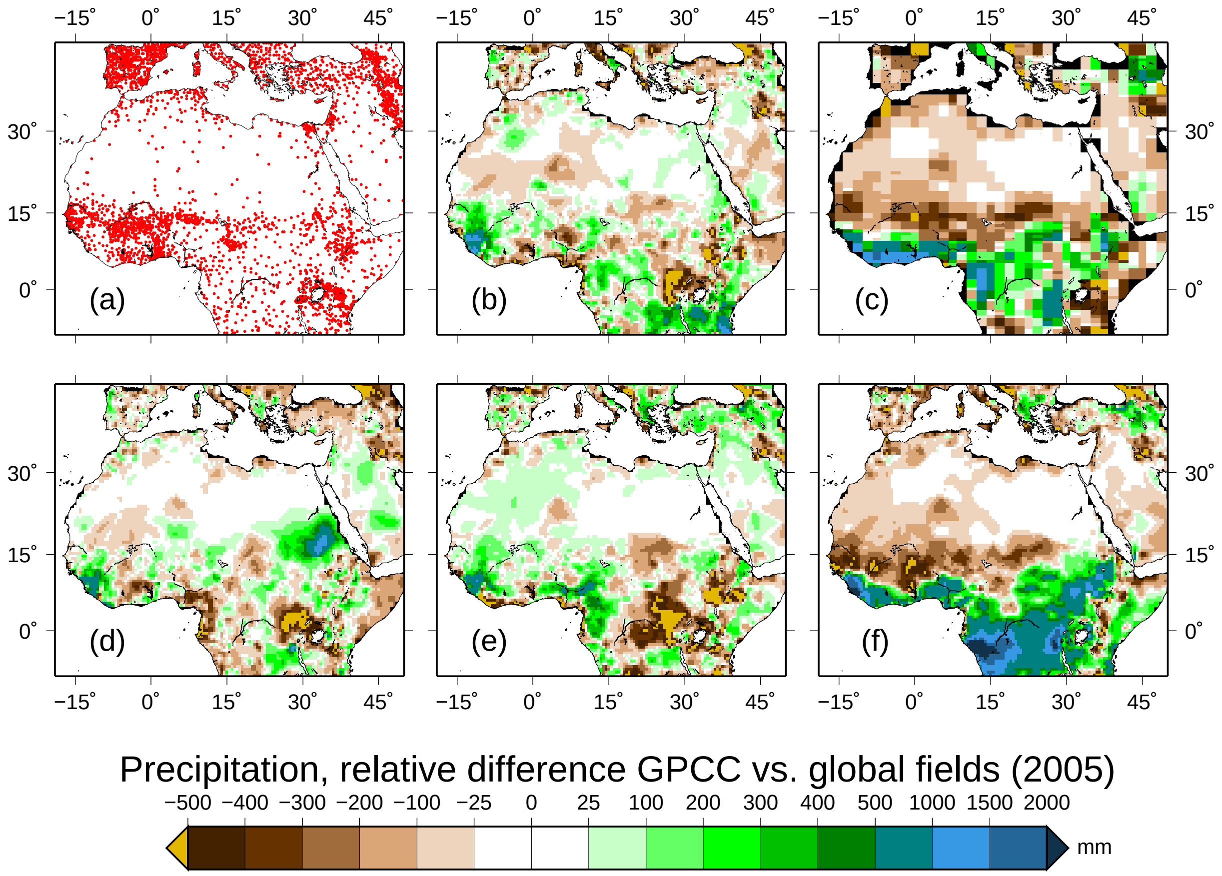

Figure 4.3.: North African domain: relative difference in annual precipitation observations and global reanalyses with respect to GPCC. (a) GPCC Station network, (b) CRUP, (c) NNRP, (d) DELP, (e) GPCP, (f) INTERIM.

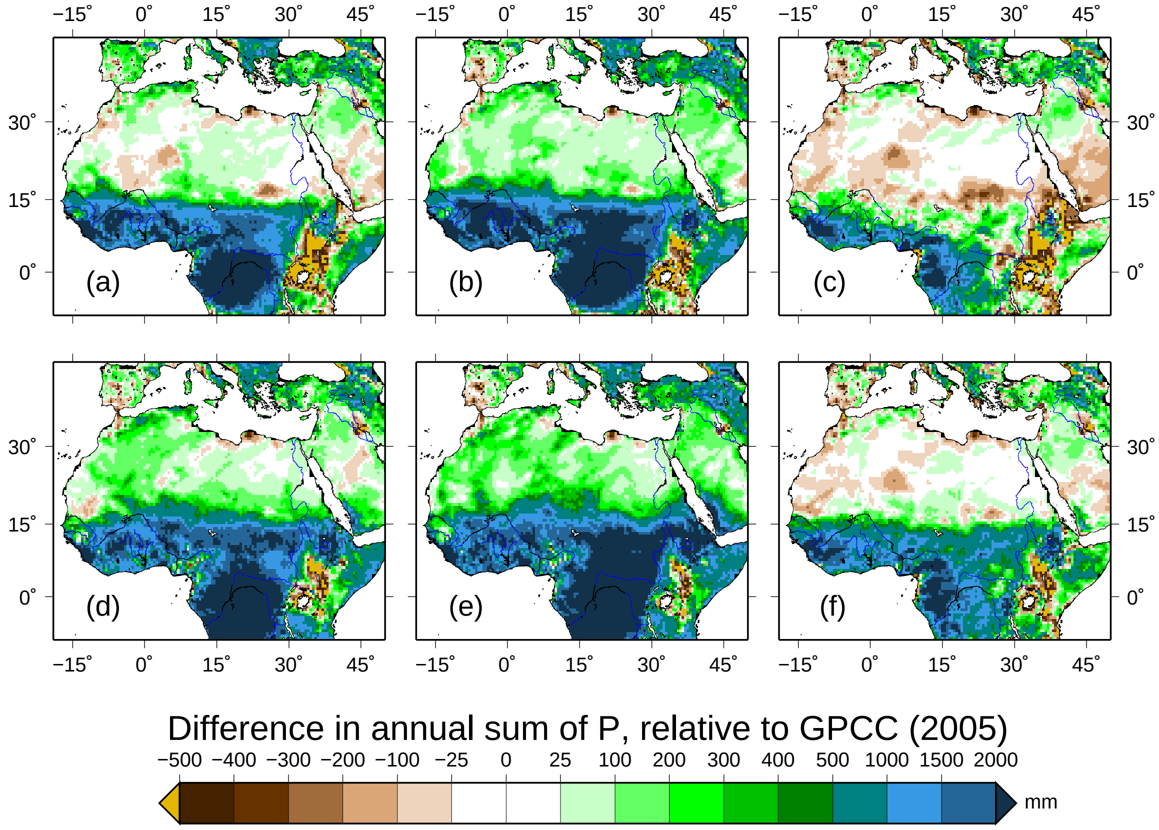

Figure 4.4.: North African domain: WRF precipitation deviations from GPCC (a) NR SST+KF , (b) NR SST+KF+FDDA, (c) NR SST+BMJ, (d) EI SST+KF, (e) EI SST+KF+FDDA, (f) EI SST+BMJ.

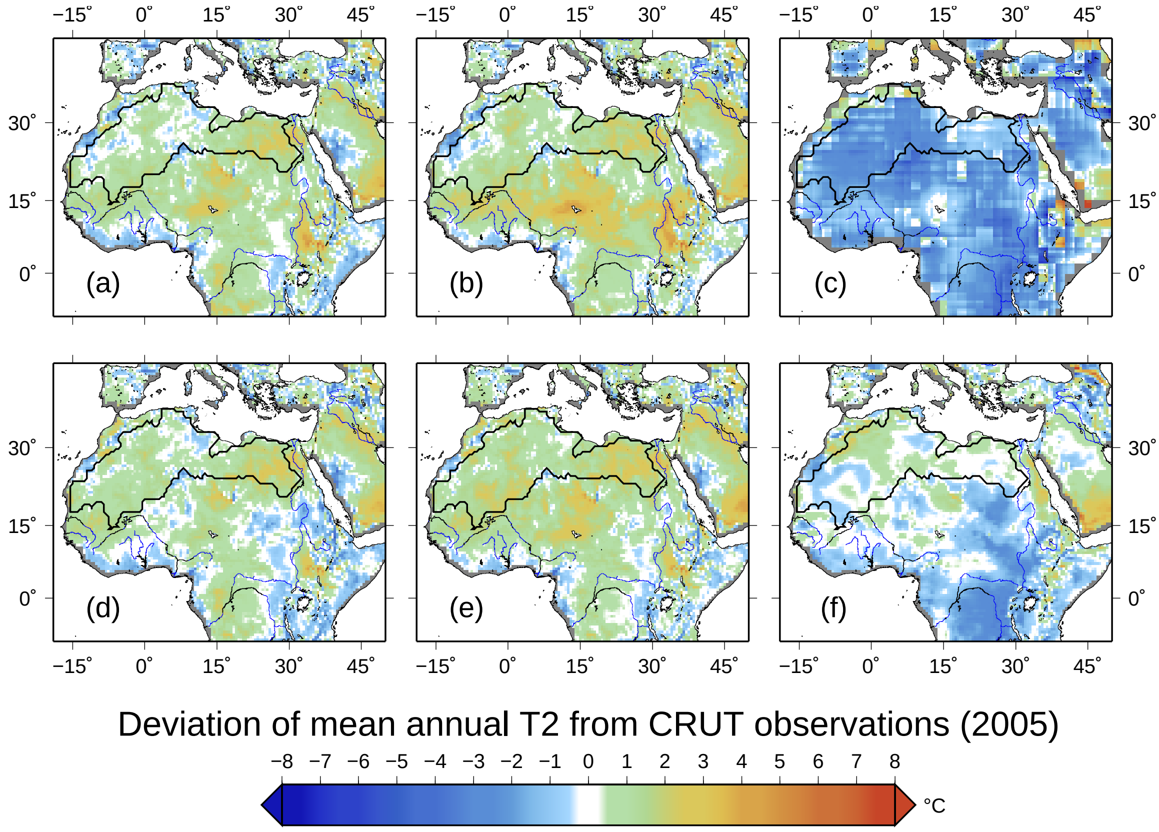

Figure 4.5.: North African domain: WRF 2m-temperature relative differences with CRUT (a) NR SST+KF , (b) NR SST+BMJ, (c) NNRP, (d) EI SST+KF, (e) EI SST+BMJ, (f) ERA-INTERIM.

precipitation amounts for nearly the complete modeling domain. A substantial decrease is seen over the basins of Chad and Kongo and and also partly for the Niger.

The analysis of precipitation patterns shows clearly that the Betts-Miller-Janjic cumulus scheme suits best for the African study region. With the Kain-Fritsch parametrization, tremendous overestimation is experienced for the Central regions and the tropical zone. Gridded nudging (FDDA) further increases the wet bias. Thus, SST+BMJ with NNRP driving is seen to be the most reasonable tested configuration of the regional model for the domain. The deviation patters for the global reanalyses are very similar.

2 meter temperature The deviation patterns for 2m-temperature are depicted in figure 4.5. For the global reanalysis fields, a cold bias tendency can be recognized. NNRP is about 2 °C below the CRUT observations. For INTERIM the picture is more differential. A slight positive bias is seen for the northern and eastern regions. Towards the south, the conditions become similar to those those from NNRP.

The WRF simulations result in a warm bias for most of the domain area. Lower values are obtained for West Africa's southern coastline and in the East. Differences in the regional model parametrization alter the strength of the bias. However no significant changes are seen for the spatial patterns. For the Sahara basin, the NR SST+KF configuration leads to an accordance with the mean value of CRUT. Surprisingly, when gridded nudging is applied (SST+KF+FDDA, very similar to SST+KF and therefore not printed), the bias values show an additional increment, especially over the northwestern continent. With the SST+BMJ setup, the zone where temperature is overestimated by 5 and more degrees, moves towards the south. Thus, from the perspective of bias, the BMJ cumulus parametrization does not outperform the other tested configurations as it is seen for precipitation. But, as shown by the comparison of figures 4.4 and 4.5, it must be noticed that precipitation and shallow air temperature have no connection in their spatial deviation patterns. Therefore, the BMJ configuration seems to be a better choice with respect to a water budget analysis.

In the following, a detailed analysis of water storage dynamics will be given for the three largest hydrological basins with sufficient data available. For the Nile it was not possible to get the discharge information for the study period.

4.3. Saharan Basin

4.3.1. Validation

Precipitation The analysis of the basin averaged time series (2003-2006) for the Sahara is depicted in the Taylor Diagram of figure 4.7 (top). The global reanalyses have a reasonable correlation with GPCC. However, the amplitudes are considerably damped which results in lower standard deviation values. GPCP shows almost no coherence with GPCC and the two curves are totally out of phase. CRUP and DELP are stronger correlated. The regional simulations tend to overestimate precipitation during the summer period (May to August). This increases the standard deviation and likewise the bias corrected RMSE. Both SST+BMJ and NR const. SST have the best coherence with the gridded observations. All SST+KF simulations have much higher standard deviation values, caused by a tremendous overestimation of the Saharan summer rainfall. In table 4.1, the values for the mean bias are presented. The best performance is seen with the BMJ configuration of the regional model ($\approx 2.5\,\mathrm{mm\ month^{-1}}$). INTERIM stays in the same range but with reversed sign. With ≈ 5 mm month^{-1}, NNRP is close to zero precipitation. All regional KF simulations reveal a positive bias between 5 and 10 mm.

2 meter temperature As listed in table 4.1, for the Saharan basin, the regional simulations return a warm bias with all tested configurations. For the NNRP driven run, the deviation ranges between 1 and 2.65 degrees with respect to CRUT. The corresponding global field contain a remarkable cold bias of -1.7 °C. For INTERIM the results are very close to CRUT. However, for the downscaling, a warm bias of 1 to 1.5 ° is obtained. By looking at the bias corrected time series, it can be seen that phase and amplitude of global reanalyses and regional simulations are in very good agreement for the Sahara basin.

4.3.2. Water Storage Variations

Model comparison For the Sahara basin, the variation in water storage is supposed to be small. Figure 4.6 visualizes the total uncertainty ranges for the global reanalyses, the WRF simulations and the GRACE gravity field solutions. For the three data types, the overall span is -20 to 40 mm month^{-1}. GRACE is approximately centered around zero and defined by a 10 to 20 mm uncertainty range. The global reanalyses show a larger and more variable span. A tendency for relatively strong storage depletion is experienced for the late summer months which is mainly due to NNRP. The WRF simulations show the strongest variability. During summer and fall, the range in results is considerably higher than the range of GRACE and the global simulations. A look at the Taylor Diagram of figure 4.7 reveals a strong connection between the time series of precipitation and storage variation. For the considered period from 2003 to 2006, the satellite estimation provides the smallest uncertainties. Furthermore, the band remains constantly within the bounds of the total atmospheric range. The different GRACE solutions show large uncertainties in terms of correlation and bias corrected RMSE (E'). For GFZ and JPL the coefficient (R) is around zero, for CSR 0.6 is obtained and E' is around 8 mm month^{-1} for both. The standard deviation is similar for CSR and GFZ. It seems that the JPL solution suffers from its background error for this regions where only small mass variations occur. Therefore, it is assumed that only CSR and GFZ provide reasonable water storage dynamics for the Saharan basin.

Table 4.1.: Saharan basin: bias for monthly time series of precipitation (mm month^{-1}), temperature (°C), and storage change (GRACE GFZ RL 04, mm month^{-1}) (2003/01 – 2006/12). Gridded observation data versus global reanalyses and regional simulations. Mean precipitation ≈ 6 mm month^{-1}.

	CRUP	GPCC	GPCP	DELP	CRUT	DELT	GRACE
INTERIM	−2.72	−3.88	−4.91	−3.30	0.30	0.15	3.12
EI SST+KF	9.84	8.68	7.65	9.26	1.09	0.94	9.28
EI SST+KF+FDDA	10.79	9.63	8.60	10.21	1.49	1.34	10.20
EI SST+BMJ	3.17	2.01	0.98	2.59	1.29	1.14	5.89
NNRP	−4.23	−5.39	−6.42	−4.80	−1.72	−1.87	−7.67
NR KF	0.70	−0.46	−1.49	0.13	2.65	2.49	10.98
NR SST+KF	5.80	4.64	3.61	5.22	0.93	0.78	7.06
NR SST+KF+FDDA	10.44	9.29	8.26	9.87	1.71	1.56	10.12
NR SST+BMJ	1.58	0.42	−0.61	1.00	0.99	0.84	3.92

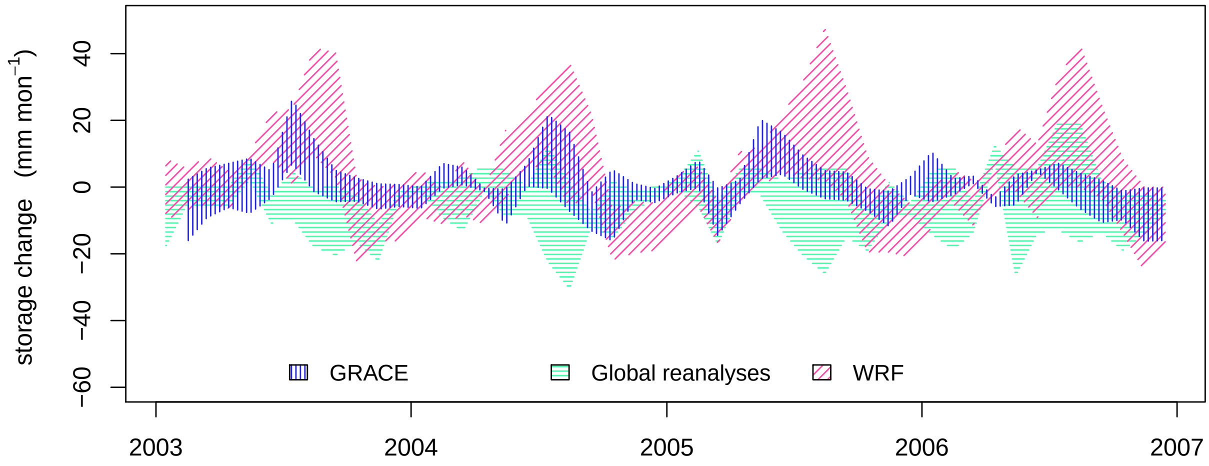

Figure 4.6.: Saharan basin: total uncertainties in basin water storage change, derived from GRACE (GFZ, CSR, JPL, release 4, Swenson & Wahr (2006) de-striping filter & 500 km Gaussian smoothing applied), global reanalysis (INTERIM, NNRP), and WRF. All atmospheric fields of $-\nabla \cdot \vec{Q}$ are smoothed by a 500 km Gaussian filter.

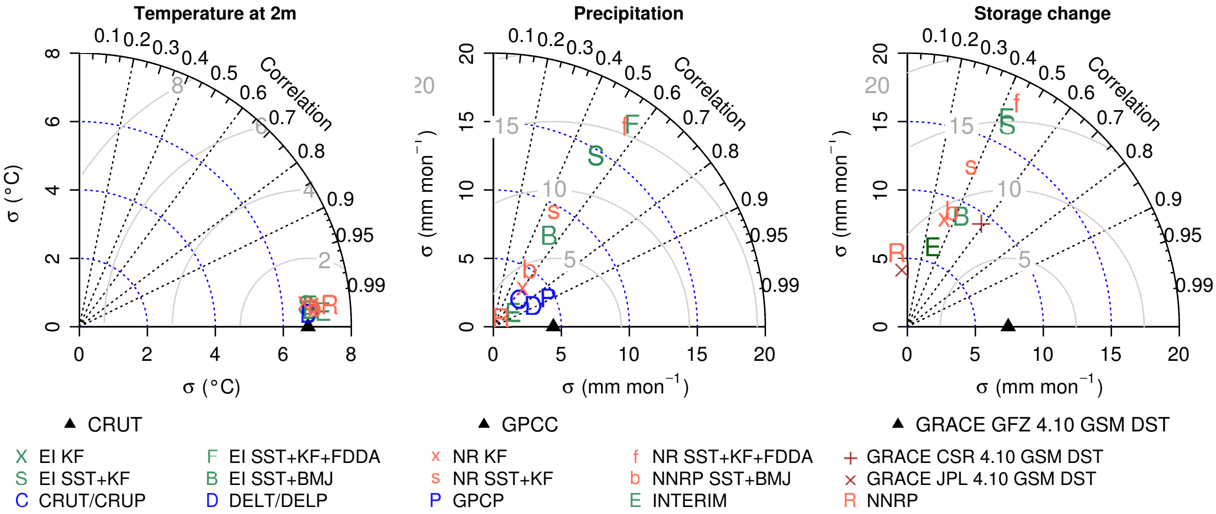

Figure 4.7.: Saharan basin: Taylor diagram for 2m temperature, precipitation, and water storage change.

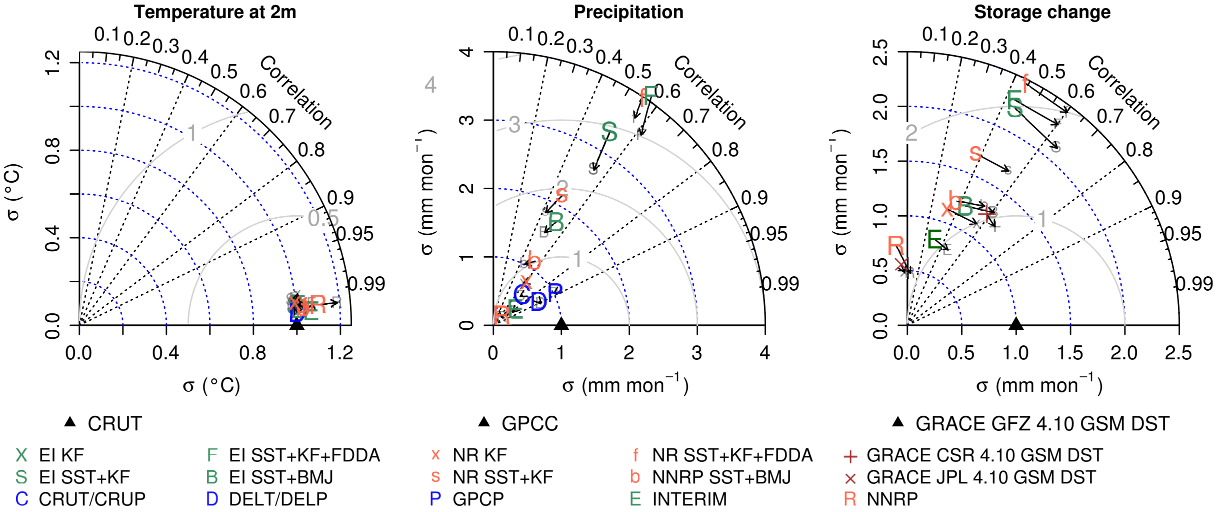

Figure 4.8.: Saharan basin: Taylor diagram for 2m temperature, precipitation, and storage change. Arrows show improvement if only considering the periods from June to November

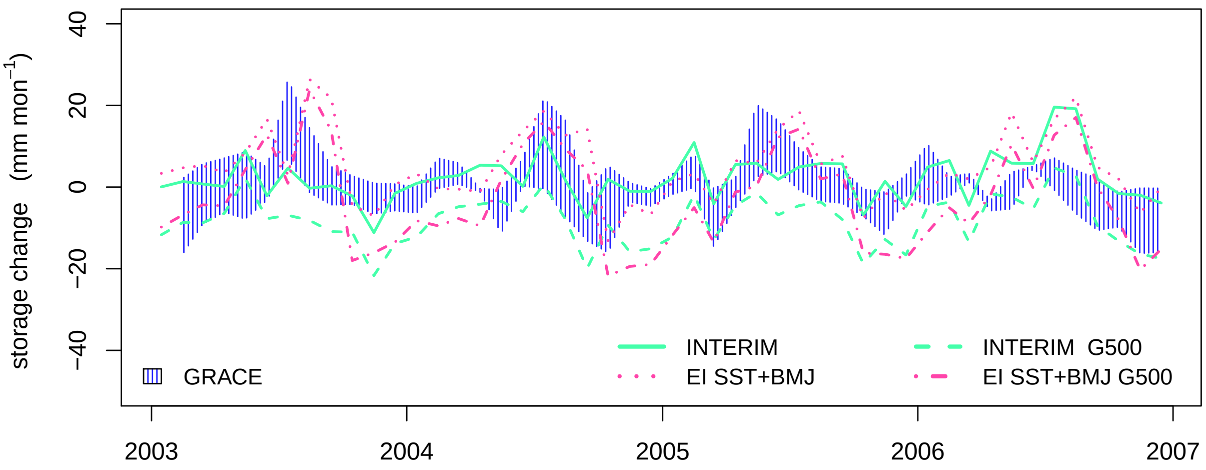

Figure 4.9.: Saharan: basin water storage variations and most suitable global and regional atmospheric models.ECMWF global reanalysis and downscaling.

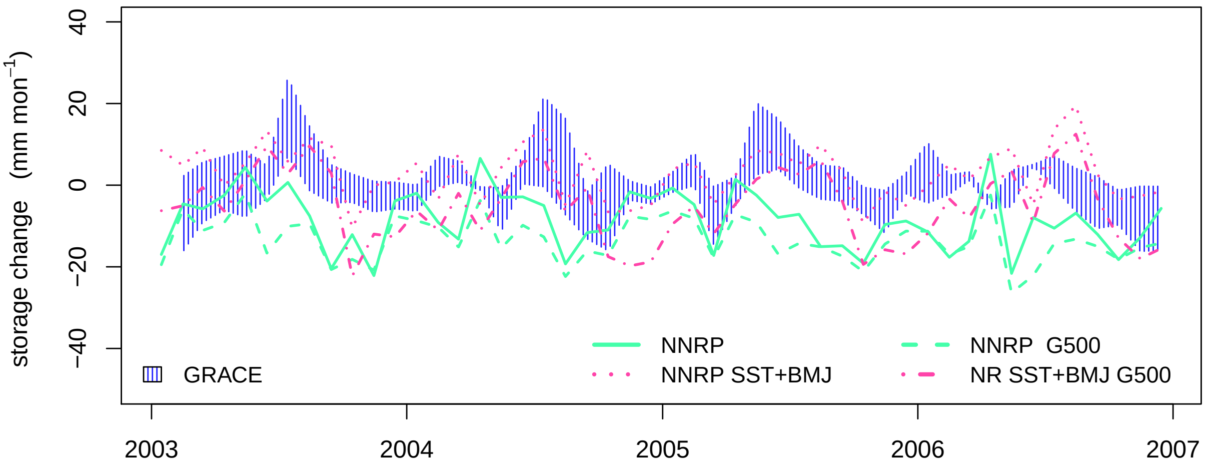

Figure 4.10.: Saharan: basin water storage variations and most suitable global and regional atmospheric models.NNRP global reanalysis and downscaling.

Reasonable models The analysis of precipitation and 2m-temperature time series reveals a poor performance for the regional SST+KF simulations. The NR SST+BMJ configuration shows the most reasonable results in terms of bias and RMSE. NR const. SST leads to a good RMSE as well. But a very strong bias (≈ 2.5 °C) is obtained for temperature. With INTERIM driving, the regional model fits best with the SST+BMJ configuration. Both global reanalyses show biases for the temperature time series and bad RMSE values for precipitation. A better skill is seen for the INTERIM product.

Figures 4.9 and 4.10 depict the time series of basin storage variations for EI SST+BMJ and INTERIM, and NR SST+BMJ and NNRP, respectively. The GRACE uncertainty bounds are printed with vertical bars. Every time series is plotted in original form and with a 500 km Gaussian filter applied (G500). An apparent disagreement with the GRACE storage variations is seen for NNRP, NNRP G500, and EI G500. Also the filtered regional time series show large deviations for the November to May periods. Hence, in order to define reasonable atmospheric uncertainty bounds, the regional simulations of NR SST+BMJ, and EI SST+BMJ, and the global time series of INTERIM should be considered. According to figure 4.7 (right panel), the two different SST+BMJ simulations have almost identical statistical properties.

Another important point is contained in the Taylor diagram for storage variation: the selected SST+BMJ runs and INTERIM are closer connected with GRACE CSR than with GRACE GFZ. Typically, the correlation coefficients improve by 0.1 if GRACE CSR is taken for reference.

Seasonal performance For the Sahara basin, the period with the best performance is found for the months from June to November. For storage change, the correlations between GRACE GFZ and regional simulations improve from ≈ 0.45 for the complete time series to ≈ 0.61 for the selected months. A small gain in performance is also seen for INTERIM. NR SST+BMJ and EI SST+BMJ move close to the position of GRACE CSR in the Taylor diagram (fig. 4.7). For precipitation, improvement is seen for the bias corrected RMSE E' and the standard deviation. The correlation measures remain almost the same. For 2m temperature, the changes are minuscule. Only NNRP shows an increase in standard deviation.

4.3.3. Performance of the Regionalization

With NNRP driving and SST+BMJ configuration, the WRF model outperforms its global counterpart. The dry and cold bias of the global reanalysis is corrected. Similar results are obtained when driving the regional model with INTERIM fields. With this set up, slightly wetter conditions are seen. As already found for the Siberian domain, the regional model contains a warm bias. However, with 1 to 1.3 °C, the deviation is significantly smaller for the simulation with SST+BMJ.

4.4. Lake Chad Basin

4.4.1. Validation

Precipitation For the Chad basin, the intra-annual distribution of rainfall is irregular with a dry period in winter and a maximum in August. Figure 4.12 shows high correlation coefficients (≈ 0.9) for all precipitation time series. Large differences exist for the standard deviation and the bias corrected RMSE. This means that the seasonal pattern is usually well resembled but the amplitude is over- or underestimated. GPCC, GPCP, CRUP, and DELP show almost identical curves. Some differences, ranging from 20 to 40 mm month^{-1}, exist for the summer peak values.

Both global reanalyses suggest 20 to 60 mm month^{-1}lower precipitation values than the gridded data sets. Also the regional NR SST+BMJ configuration performs likewise. All other regional simulations overestimate rainfall, especially in the summer. With SST+KF and SST+KF+FDDA the summer values are vastly exceeded by 100 to 150 percent. The bias values for the Chad basin are given in table 4.2. SST+BMJ is the best performing configuration for the EI driving. NR with constant SST is similar to EI SST+BMJ. As already mentioned, EI constant SST cannot be analyzed because WRF does not execute numerically stable. Similar to the Sahara, NR driving always results in less precipitation than the respective EI simulation.

For the Chad basin it is concluded that the performance of the KF cumulus scheme in WRF is unfit. With BMJ the monthly rainfall time series fit better to the gridded observations. Different to Siberia The application of different global boundary conditions has an important impact on the water balance of the regional model. The global reanalyses show a pronounced dry bias.

2 meter temperature For the Chad basin, different results are mainly found for the temperature minimum in January. While the regional simulations are 3 to 4 °C too warm, the global reanalyses are 2 to 3 °C below the observations. NNRP has a cold bias throughout the year. The BMJ configurations (EI and NR) of WRF return the warmest conditions, being too warm for all seasons. KF and KF+FDDA are very close to the observations during the summer periods. Beside the absolute bias, the regional simulations remain within a similar range of uncertainty when compared to DELT. The global reanalyses have slightly different statistical properties with increased standard deviation (figure 4.12, top).

In terms of 2m-temperature, KF and KF+FDDA outperform the BMJ cumulus scheme. However, with regard to precipitation, KF cannot be considered as reasonable, especially for the summer months, where large precipitation overestimation contradicts the good fit for temperature.

4.4.2. Water Storage Variations

Model comparison In figure 4.11 the span in basin storage variations in the Chad basin is presented for GRACE, global reanalyses, and regional simulations. According to GRACE and the global reanalyses, the monthly rates oscillate from -50 to 50 mm month^{-1}. The different configurations of WRF result in values of -20 to 200 mm month^{-1}. Similar to Sahara and Amazon, the large storage replenishing rates are found during the rainy season. In the dry winter months (December to February), all three products show similar amounts of uncertainty.

The CSR and JPL GRACE time series are very congruent. The GFZ GRACE solution contains a stronger amplitude and is responsible for the peak in 2003 and 2004. The overall uncertainty bounds for GRACE range between 10 and 50 mm month^{-1}. The global reanalyses have their largest variability in early summer. Most of the peak values are caused by the NNRP time series.

As visualized in figure 4.12 (right panel), the correlation coefficients for storage change reach values between 0.55 to 0.85. With respect to GFZ, JPL and CSR yield a R of approximately 0.85. The SST+KF and SST+KF+FDDA simulations result in two to three times increased standard deviation values. Also the bias corrected RMSE reaches 40 to 60 mm month^{-1}.

Reasonable models The evaluation of the basin averaged temperature and precipitation time series leads to the conclusion that regional simulations with BMJ cumulus scheme outperform the KF configuration. However, none of the two BMJ simulation fits exactly to the observed

Table 4.2.: Chad basin: bias for monthly time series of precipitation (mm month^{-1}), temperature (°C), and storage change (GRACE GFZ RL 04, mm month^{-1}) (2003/01 – 2006/12). Gridded observation data versus global reanalyses and regional simulations.

	CRUP	GPCC	GPCP	DELP	CRUT	DELT	GRACE
INTERIM	−6.65	−7.88	−8.55	−9.21	−0.43	−0.84	−2.93
EI SST+KF	78.29	77.06	76.39	75.74	0.57	0.15	70.86
EI SST+KF+FDDA	86.60	85.37	84.70	84.04	0.50	0.09	77.54
EI SST+BMJ	22.93	21.71	21.03	20.38	1.35	0.94	25.46
NNRP	−9.97	−11.20	−11.87	−12.53	−1.98	−2.40	18.24
NR KF	17.23	16.00	15.33	14.67	3.03	2.62	38.19
NR SST+KF	44.06	42.83	42.16	41.50	1.16	0.75	44.06
NR SST+KF+FDDA	75.42	74.20	73.52	72.87	1.10	0.69	68.95
NR SST+BMJ	1.62	0.40	−0.28	−0.93	1.76	1.35	9.39

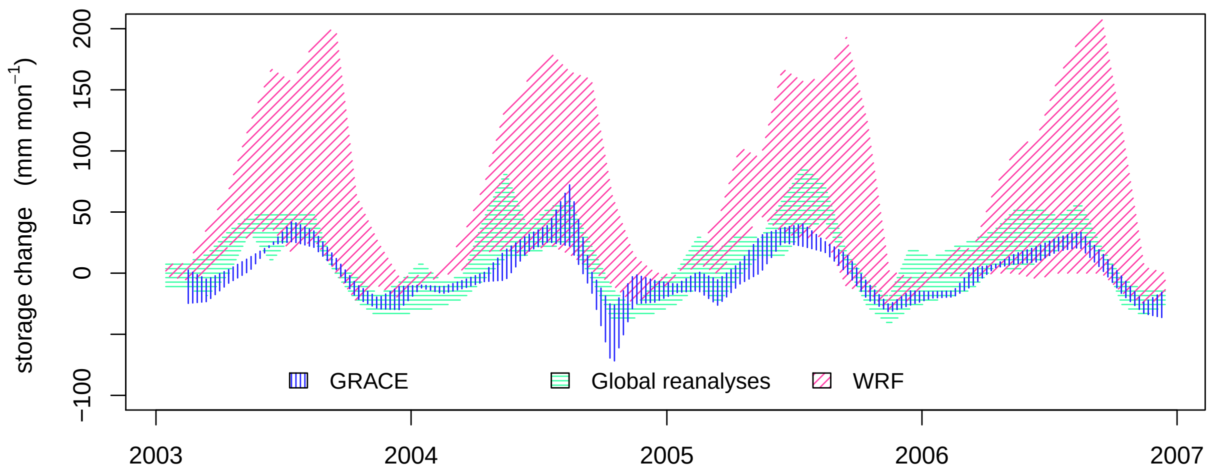

Figure 4.11.: Lake Chad basin: total uncertainties in basin water storage change, derived from GRACE (GFZ, CSR, JPL, release 4, Swenson & Wahr (2006) de-striping filter & 500 km Gaussian smoothing applied), global reanalysis (INTERIM, NNRP), and WRF. All atmospheric fields of $-\nabla \cdot \vec{Q}$ are smoothed by a 500 km Gaussian filter.

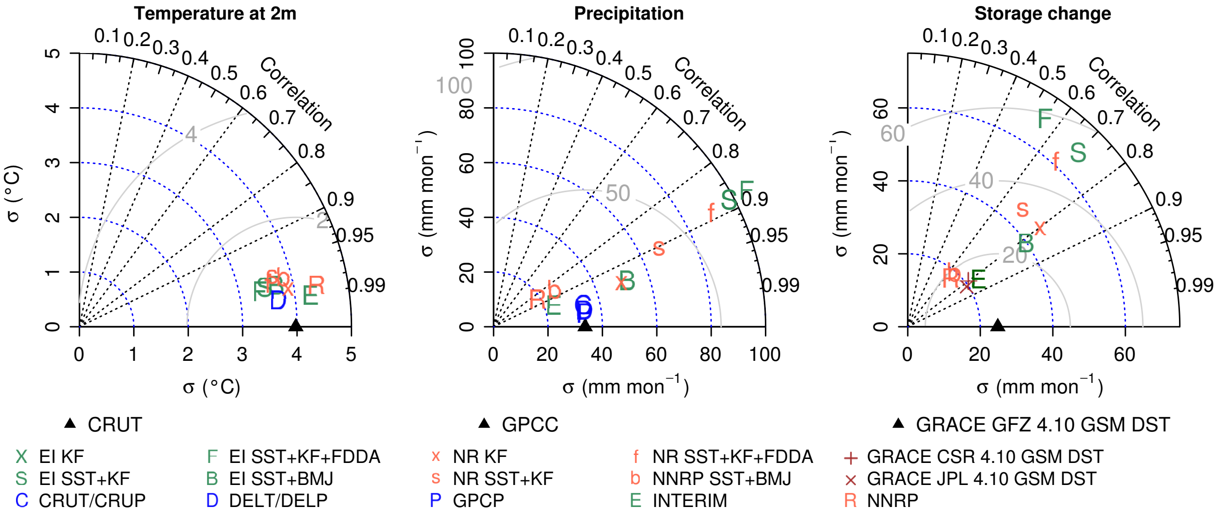

Figure 4.12.: Lake Chad basin: Taylor diagram for 2m temperature, precipitation, and water storage change.

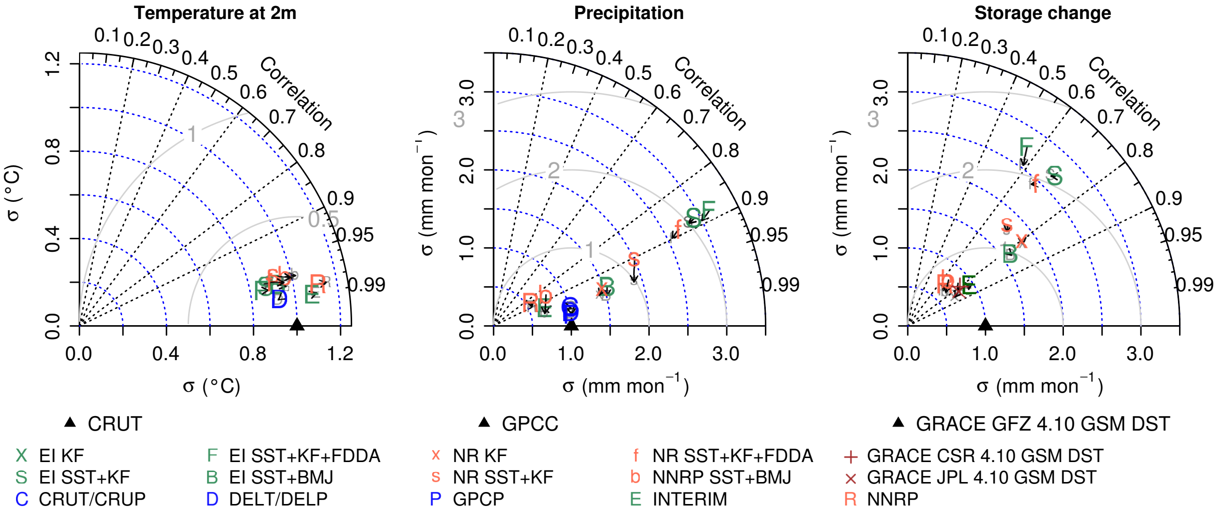

Figure 4.13.: Lake Chad basin: Taylor diagram for 2m temperature, precipitation, and storage change. Arrows show improvement if only considering the periods from July to February

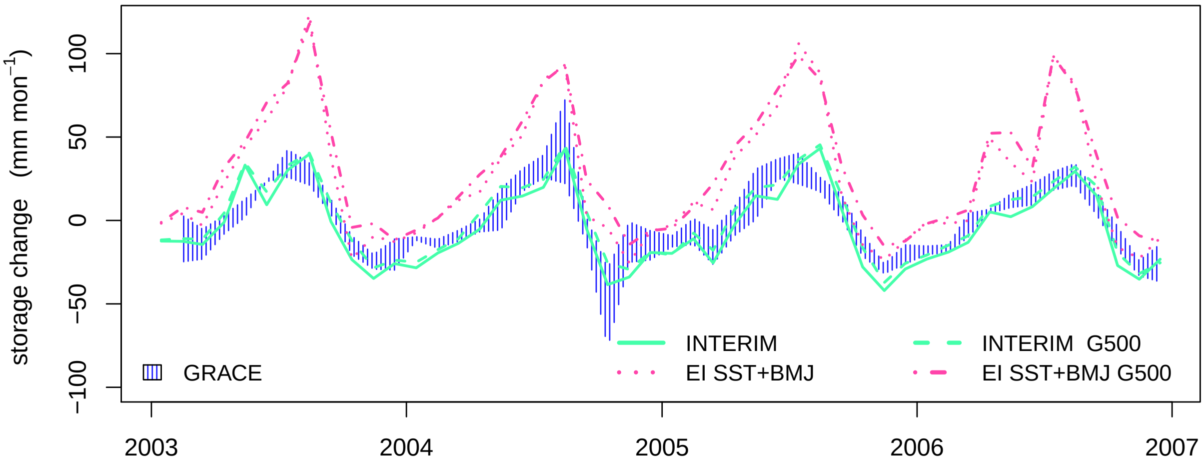

Figure 4.14.: Lake Chad basin: water storage variations and most suitable global and regional atmospheric models. ECMWF global reanalysis and downscaling.

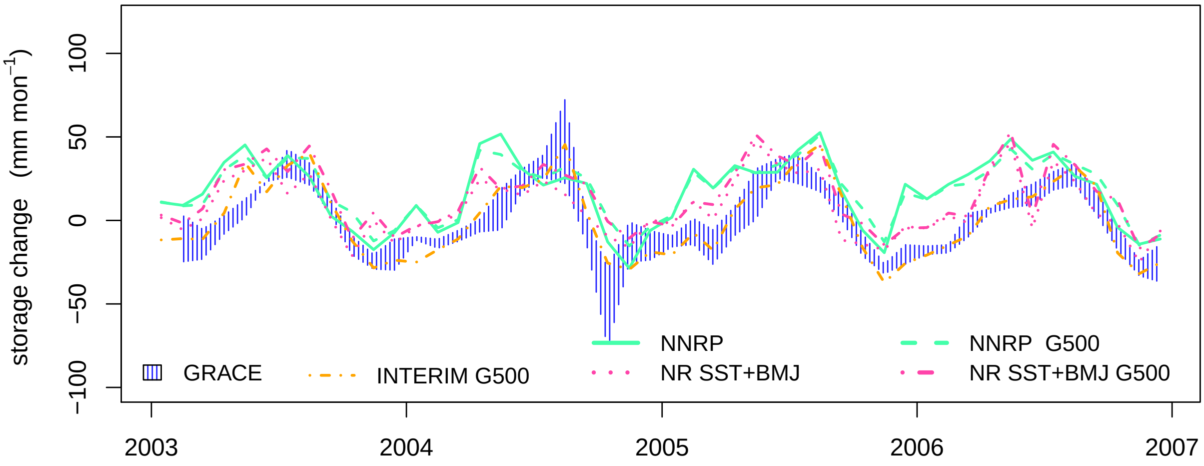

Figure 4.15.: Lake Chad basin: water storage variations and most suitable global and regional atmospheric models. NNRP global reanalysis and downscaling.

precipitation (compare fig. 4.12, center). Thus, for the moment, both are accepted in terms of reasonableness. For the global reanalyses, the ranking is more clear. For temperature and precipitation, INTERIM performs better than NNRP in terms of correlation and bias.

The selected time series of storage variation for EI SST+BMJ and INTERIM, and NR SST+BMJ and NNRP are presented in the figures 4.14 and 4.15. The most obvious difference is seen for the GRACE estimates and the EI SST+BMJ runs. Contrastingly, the global time series of ERA INTERIM fits very well to the GRACE uncertainty bounds. NNRP shows less agreement with the satellite data. Deviations are mainly seen for the months of spring, with a general tendency of higher storage input rates. The corresponding regional simulation (NR SST+BMJ) sticks closely to its global counterpart, but shows increased coherence with GRACE when NNRP returns large deviations.

With regard to the overestimation of precipitation by EI SST+BMJ, it is assumed that the amplitudes in EI SST+BMJ storage variation are unreasonably high. Therefore, the range of atmospheric uncertainty should be defined by INTERIM and NR SST+BMJ. If NNRP is added to the evaluation, atmospheric uncertainty exceeds the GRACE range.

For the Chad basin, with Gaussian filtering of the atmospheric derived storage variations (G500, dashed and dotted lines) the time series become slightly shifted towards the GRACE estimates.

Seasonal performance For NNRP, INTERIM, and NR SST+BMJ the mean correlation coefficient for the 2003-2006 time series of storage change is 0.68. By removing all March to June values from the time series, the correlation coefficient increases to 0.78. Figure 4.13 visualizes the changes (arrows) in the statistical measures for the subset of all July to February values for the period of 2004-2006. In general, the experienced changes are small. Hence, it is assumed that the simulation quality for the selected reasonable models is more or less constant with time.

4.4.3. Performance of the Regionalization

For the Chad basin, the regional model simulations add substantial skill to their global driving reanalyses. Similar to the Saharan basin, compared to INTERIM, the NNRP driven downscaling agrees better with the global observations of precipitation, but only if the SST+BMJ configuration is applied. The downscaling leads to a significant reduction of the dry bias of the global reanalysis. However, the global cold bias of around -2 °C is turned into a warm bias of similar size.

4.5. Niger Basin

4.5.1. Validation

Precipitation In figure 4.16 the time series of observed and modeled precipitation are compared for the Niger basin. The distribution within the Taylor Diagram is broadly similar with that from the Chad basin but correlation coefficients are more widespread. A dry bias is seen for the global fields. All regional simulations exceed the observed curves. Table 4.3 list the respective bias amounts. Like for the Chad basin, the strongest deviations are obtained with the SST+KF and SST+KF+FDDA configuration of the regional model. In terms of phase correlation, all simulations show a reasonable performance (>0.9). With SST+BMJ maximum coefficients of 0.98 are achieved. Different as for the Chad basin, NR SST+KF contains a positive bias. However, this configuration matches best with the gridded observations. According to the Taylor depiction NR const. SST performs also well.

Altogether, the BMJ cumulus scheme outperforms the KF method for both global driving models. For the regional simulations, the best performance is seen with the NR SST+BMJ configuration. While NNRP is topped by its regional counterpart, no skill is added to INTERIM by a downscaling with WRF.

2 meter temperature All regional simulations suffer a warm bias. The highest deviation is seen for NR const. SST with $\approx 2.8\,°C$. SST+KF and SST+KF+FDDA results in a mean overestimation of 0.5 to 0.8 °C. As already seen for the Chad basin, the BMJ scheme leads to higher temperatures than the KF scheme.

In terms of the global reanalyses, INTERIM shows the best coherence with CRUT and DELT (R >0.99). NNRP is less correlated ($R \approx 0.95$). The elevated standard deviation and error corrected RMSE values are due to an amplified seasonal amplitude. The preeminence of INTERIM is further corroborated by the bias results listed in table 4.3. NNRP suggest more than 2 °C colder conditions than observed. INTERIM contains also a cold bias but it only amounts ≈ 0.2 °C.

As can be seen from the left panel of figure 4.16, the time series for the Niger basin reveal a distinctive spread in the Taylor plot. This is mainly caused by differences in the seasonal amplitudes. Compared to the gridded observations, the regional simulations return a damped annual cycle. The best performance is seen for NR const. SST and NR SST+BMJ. NR const. SST is well performing in terms of standard deviation, NR SST+BMJ outperforms with respect to correlation coefficient and bias corrected RMSE.

4.5.2. Water Storage Variations

Model comparison Figure 4.16 depicts the statistical coherence of modeled water storage variation with the hydrological GRACE product from GFZ. The time series is limited to the period of 2003-2005, because discharge data is not available for the subsequent years. Like for the Chad basin analysis, similar performance is seen for the WRF simulations. NR SST+BMJ, EI SST+BMJ, and NR const. SST have similar correlation coefficients of ≈ 0.9. All regional KF runs show less agreement with GRACE (≈ 0.68-0.82). In terms of RMSE and standard deviation NR SST+BMJ has the smallest distance with GRACE GFZ on the Taylor plot. As the time-series plot of figure 4.19 illustrates, the deviations result from higher storage input rates during the rainy season. Concerning the global reanalysis fields, INTERIM resembles the GFZ and CSR GRACE solutions best. NNRP is almost uncorrelated and phase shifted, as can be seen from figure 4.19. The uncertainty bound for the different GRACE solutions varies between 2 mm month^{-1} in winter and spring and 40 mm month^{-1} during the rainy season.

The bias values with respect to GRACE GFZ are printed in table 4.3. The lowest values are found for INTERIM (6.15 mm month^{-1}) and NR SST+BMJ (31.46 mm month^{-1}). Despite for NR const. SST, a straight correlation between GRACE and precipitation bias is found for the regional simulations. This does not apply to the global fields.

Reasonable models INTERIM and NR SST+BMJ are the best cohering time series with respect to GRACE. The analysis of plausibility in terms of temperature and precipitation provides a similar conclusion. The respective time series are given in figures 4.18 and 4.19. Gaussian smoothing (G500) increases the correlation for GRACE and INTERIM. During the episodes where a close agreement exists also the regional time series become shifted towards GRACE.

Table 4.3.: Niger basin: bias for monthly time series of precipitation (mm month^{-1}), temperature (°C), and storage change (GRACE GFZ RL 04, mm month^{-1}) (2003/01 – 2006/12). Gridded observation data versus global reanalyses and regional simulations.

	CRUP	GPCC	GPCP	DELP	CRUT	DELT	GRACE
INTERIM	−10.79	−7.32	−14.28	−8.95	−0.18	−0.33	6.15
EI SST+KF	85.14	88.61	81.65	86.98	0.53	0.38	82.80
EI SST+KF+FDDA	89.72	93.20	86.24	91.56	0.52	0.37	86.66
EI SST+BMJ	54.89	58.36	51.40	56.73	1.03	0.88	64.06
NNRP	−16.75	−13.27	−20.23	−14.91	−1.97	−2.12	34.98
NR KF	10.15	13.62	6.66	11.99	2.74	2.59	52.05
NR SST+KF	78.30	81.77	74.81	80.14	0.80	0.65	79.85
NR SST+KF+FDDA	109.76	113.23	106.27	111.60	0.74	0.59	106.50
NR SST+BMJ	20.89	24.36	17.40	22.73	1.47	1.32	31.46

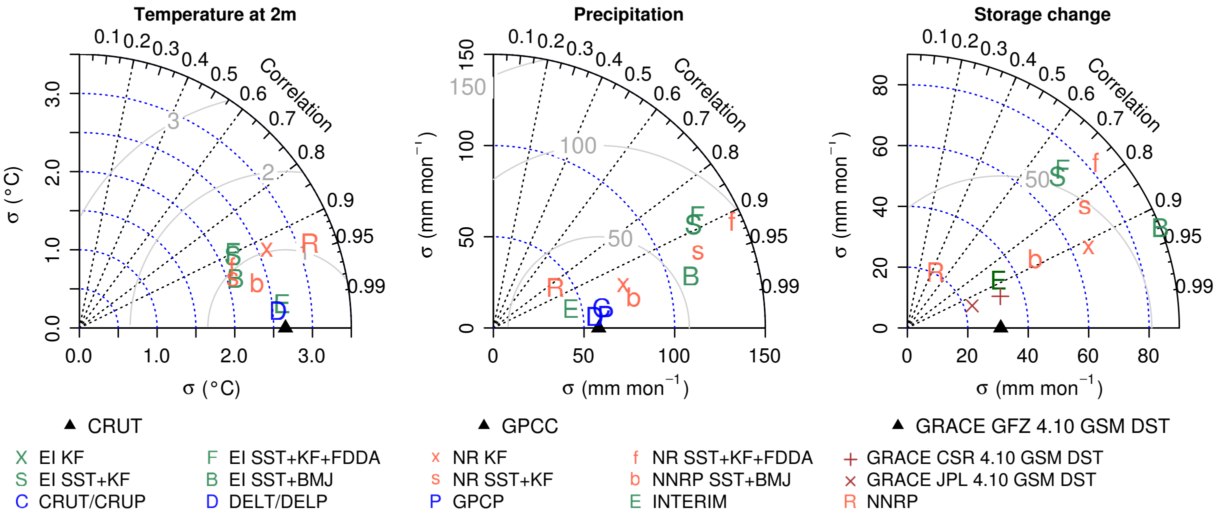

Figure 4.16.: Niger basin: Taylor diagram for 2m temperature, precipitation, and water storage change.

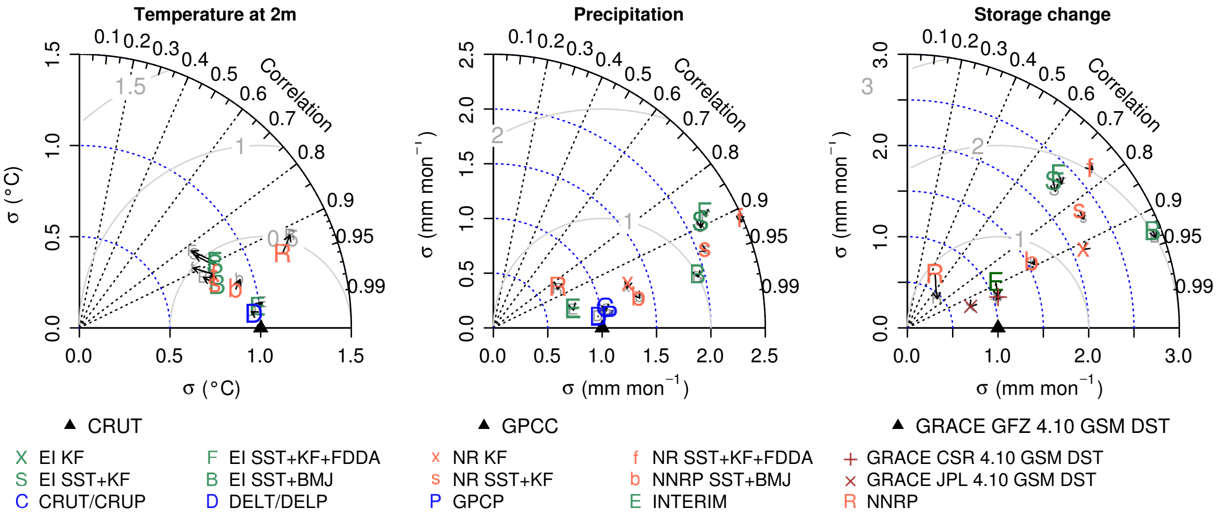

Figure 4.17.: Niger basin: Taylor diagram for 2m temperature, precipitation, and storage change. Arrows show improvement if only considering the periods from June to March

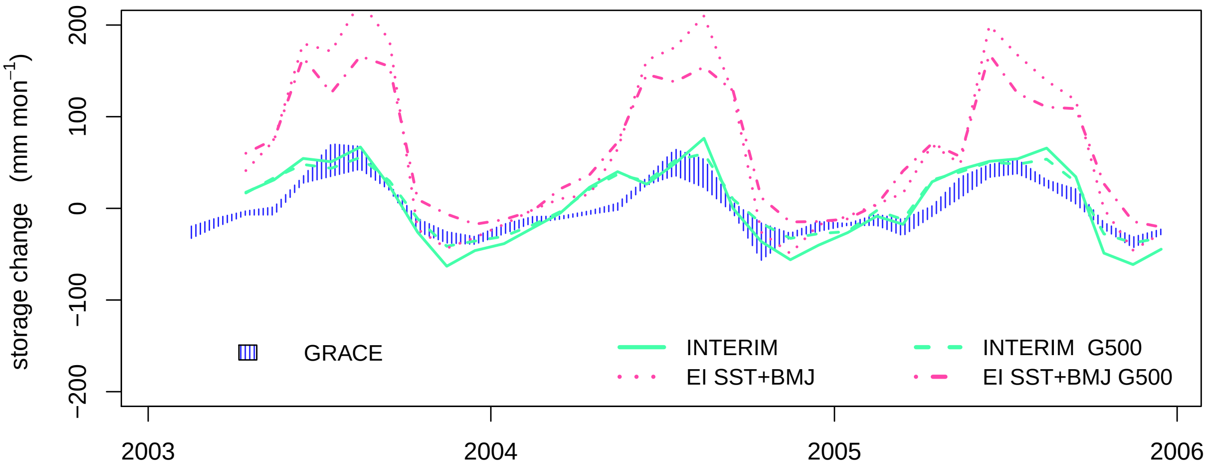

Figure 4.18.: Niger basin: water storage variations and most suitable global and regional atmospheric models. ECMWF global reanalysis and downscaling.

However, for the summer months, the deviations are further increased. For NNRP the peaks are evened. But no correction is seen for the experienced anti cyclic seasonal pattern.

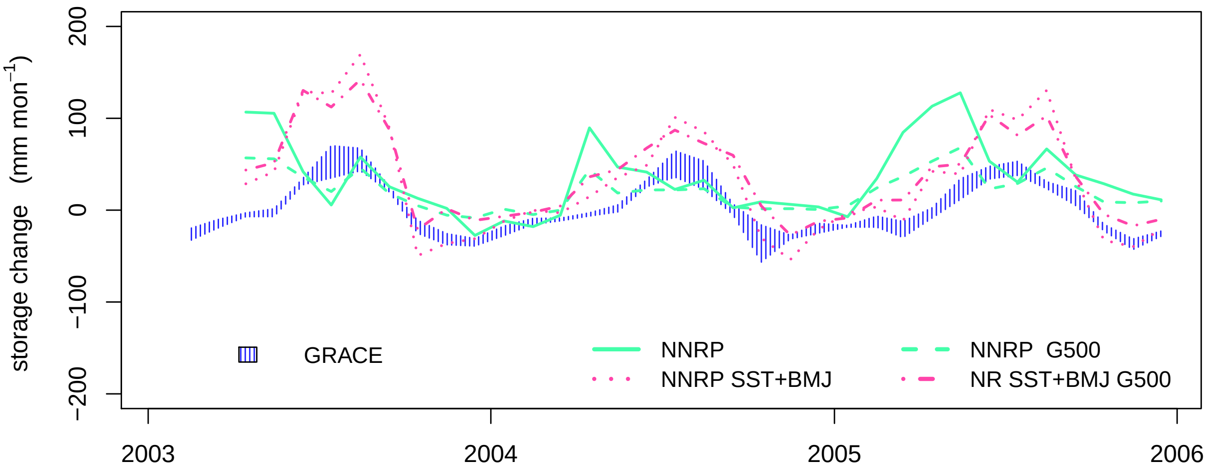

Figure 4.19.: Niger basin: water storage variations and most suitable global and regional atmospheric models.NNRP global reanalysis and downscaling.

Seasonal performance With respect to GRACE, the mean correlation coefficient for water storage variations of INTERIM and NR SST+BMJ is 0.9. This value can be increased to a maximum of 0.93, if only monthly values from June to March are considered. However, the increment is caused by the global time series only. As visualized in figure 4.17, NR SST+BMJ remains almost constant in the Taylor depiction. A slight gain in coherence is seen for the Kain-Fritsch parametrized regional simulations. Contrastingly, the same time series experience a drop in correlation in the temperature plot. A similar effect is recognized for the global reanalysis of NNRP. For precipitation, no distinct difference is seen between the full time series and the selected subset. Thus, the seasonal performance of INTERIM and NR SST+BMJ is constant over the years.

4.5.3. Performance of the Regionalization

For the Niger basin, the downscaling does not result in clear improvement of the global reanalyses. Besides the temperature overestimation, that was also seen in a similar range for the Saharan and the Chad basin, the precipitation is overestimated. Large bias values are especially observed for the monsoon period. Again, NNRP driven simulations fit better to the global observation data sets. However, the global NNRP reanalysis contains a remarkable dry and cold bias that is about the negative amount of the overestimation by the regional model.

4.6. African Domain: Performance of Regionalization

Altogether, it can be stated that INTERIM performs best in the comparison of the global reanalyses. For the regional simulations, NR+SST+BMJ is the configuration that agrees best with the observations of precipitation and temperature. For the Saharan and the Chad basin, with this setup of the regional model, the global driving reanalyses is clearly outperformed. The NR const. SST run is shelved because of an inferior correlation and much stronger bias. The

INTERIM driven WRF simulations yield a serious wet bias for the rainy periods. In general it is found that precipitation is vastly overestimated for the tropical and monsoonal regions during the rainy season.

5

Australian domain

With 8,500,000 km^2, Australia forms the smallest continent on earth. In 30 km horizontal resolution, the regional model domain comprises 23,491 cells. This is only one third compared to the North African domain or almost identical with the Amazonian domain. Therefore, Australia is the only study region that can be modeled as a complete unit, with domain boundaries defined over water only. Climatologically, this study region is very similar to the North African domain.

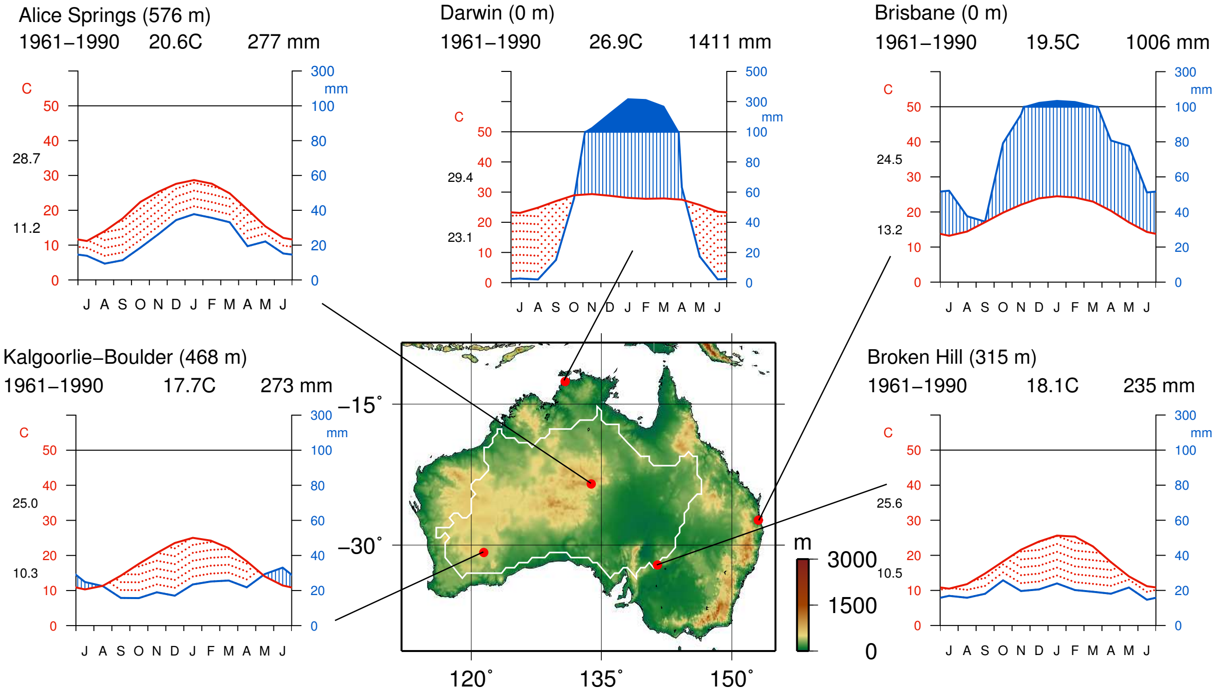

Figure 5.1.: Domain configuration and climate diagrams.

5.1. Domain Characteristics

Climate The Köppen-Geiger climate classification defines the major part of Central Australia as hot arid desert. North of 20 ° S and east of 145 ° E, the conditions transform into steppe with a slight increase in annual rainfall. More humid climates occur along the coast and reach a few hundred kilometers inland. The eastern coastal regions are warm and temperature, fully humid with warm or hot summer temperatures. The south and southwest are summer dry and along the northern regions are influenced by equatorial and winter dry conditions. The properties of the western and northwestern regions are similar dry like for the center of the continent. Beside this general classification, the year to year climate is strongly affected by the adjacent oceans. Changes in SST and circulation can cause periods of severe drought but also positive anomalies. Further information about precipitation anomalies can be found in Drosdowsky (1993) or Taschetto & England (2009).

Hydrometeorology The climate diagrams in figure 5.1 give a good sketch about the distribution of rainfall over Australia. In the tropical northern regions most of the rainfall occurs during summertime with an annual total of 1500 to 2000 mm. Along the east cost, the precipitation regime is a bit more even and the sums are in the order of 1000 mm per year. Towards the inland these values are strongly reduced. However, even for the deserts, the amount of precipitation is higher than 100 to 200 mm yr^{-1}. In some places of the Sahara values of 30 mm or even less are experienced. Nevertheless, potential evaporation exceeds precipitation by far.

Study region The central Australian region that is chosen for the evaluation with GRACE observations of water storage variations is depicted in figure 5.1. The area, defined by the white line, covers 3,880,436 km^2. All runoff is directed towards the inside. No discharge leaves the surrounding border. Therefore, the hydrological water balance equation becomes simplified like for the Sahara or the Lake Chad basin.

5.2. Validation

Topography Australia's topography is mainly even. Mountains exist along the eastern coast and in the western part. The highest elevation reaches 2,228 m.a.s.l. Therefore, for most parts of the continent, luv and lee effects are not too important for the formation and distribution of large scale precipitation. The comparison of terrain heights for the different atmospheric models (fig. 5.2) shows deviations mainly for the maximum heights. For the coarse resolution of NNRP this effect becomes very pronounced, especially for the eastern mountain ridges. Positive elevation values are found for the Timor Sea between the mainland and the Indonesian islands.

Precipitation In figure 5.3, the deviations in annual precipitation are presented for the global observations products and the global reanalysis models. The station network of GPCC (a) is comparatively dense for the eastern and southwestern regions. Like for the North African domain, large gaps exist for the deserts regions in the center of the continent. Compared to GPCC, CRUP (b) shows a dry bias for large areas. East of 120 ° E and in the eastern coastal regions, the values are lowered by 100 to 200 mm. DELP (d) agrees reasonably with GPCC. Many areas lie within the ±25 mm range. Stronger deviations are seen along the eastern coastline and around 20 ° S 130 ° E. GPCP (e) returns wetter conditions for most parts of Australia. Especially along the coastline, the observations exceed those of GPCC by up to 300 mm.

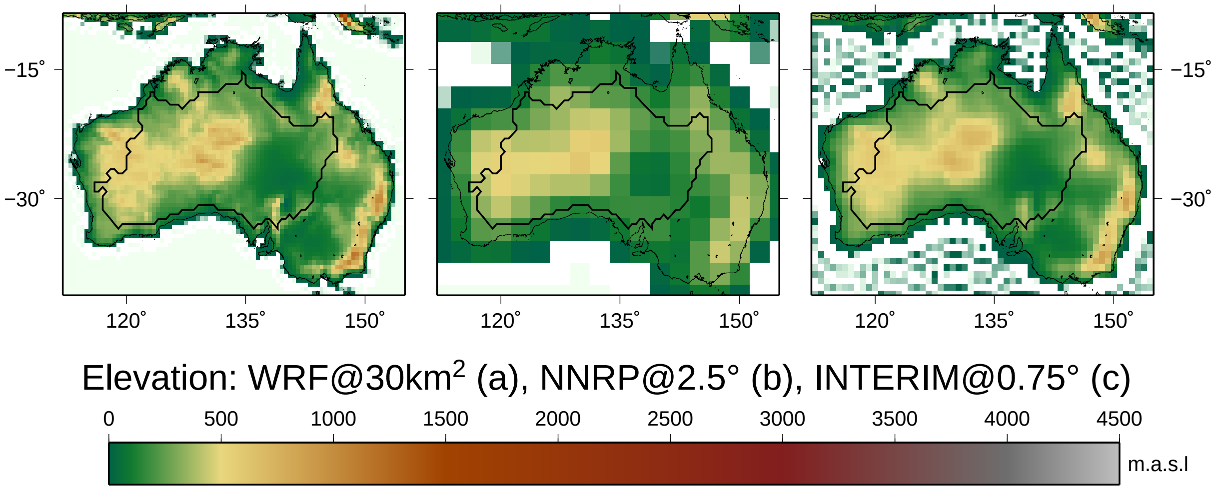

Figure 5.2.: Australian domain: DEM configuration for WRF (a) and the reanalysis models of NCAR/NCEP (b) and ECMWF ERA-INTERIM (c).

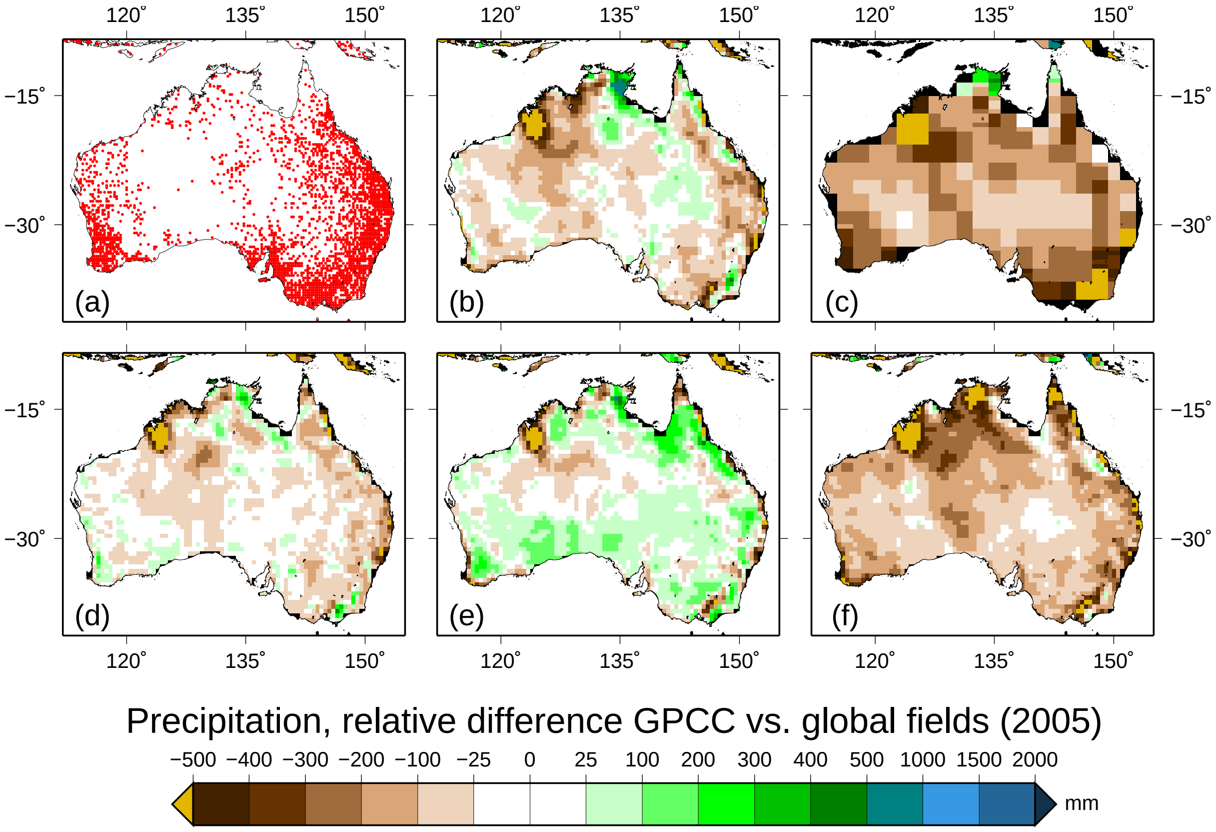

Figure 5.3.: Australian domain: relative difference in annual precipitation observations and global re-analyses with respect to GPCC. (a) GPCC Station network, (b) CRUP, (c) NNRP, (d) DELP, (e) GPCP, (f) INTERIM.

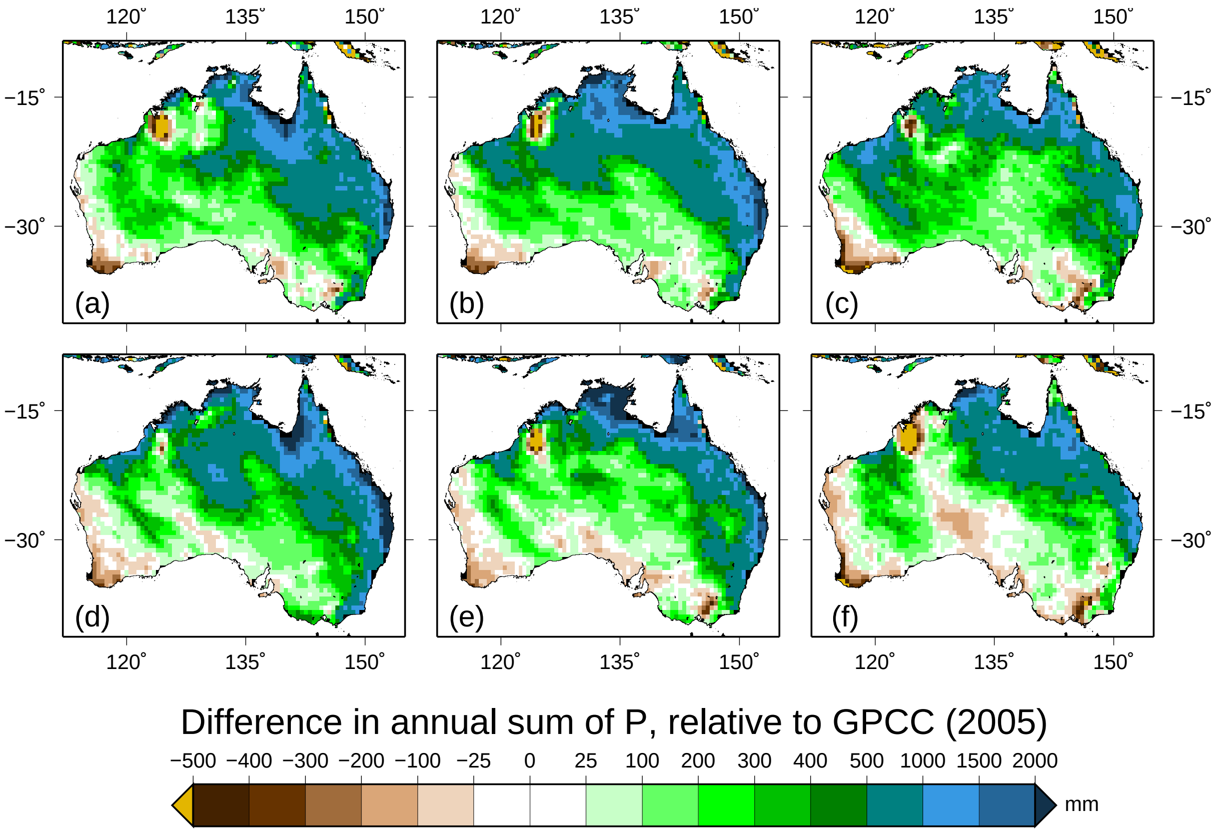

Figure 5.4.: Australian domain: deviation in annual precipitation of downscaled reanalyses with respect to GPCC. (a) NR SST+KF , (b) NR SST+KF+FDDA, (c) NR SST+BMJ, (d) EI SST+KF, (e) EI SST+KF+FDDA, (f) EI SST+BMJ.

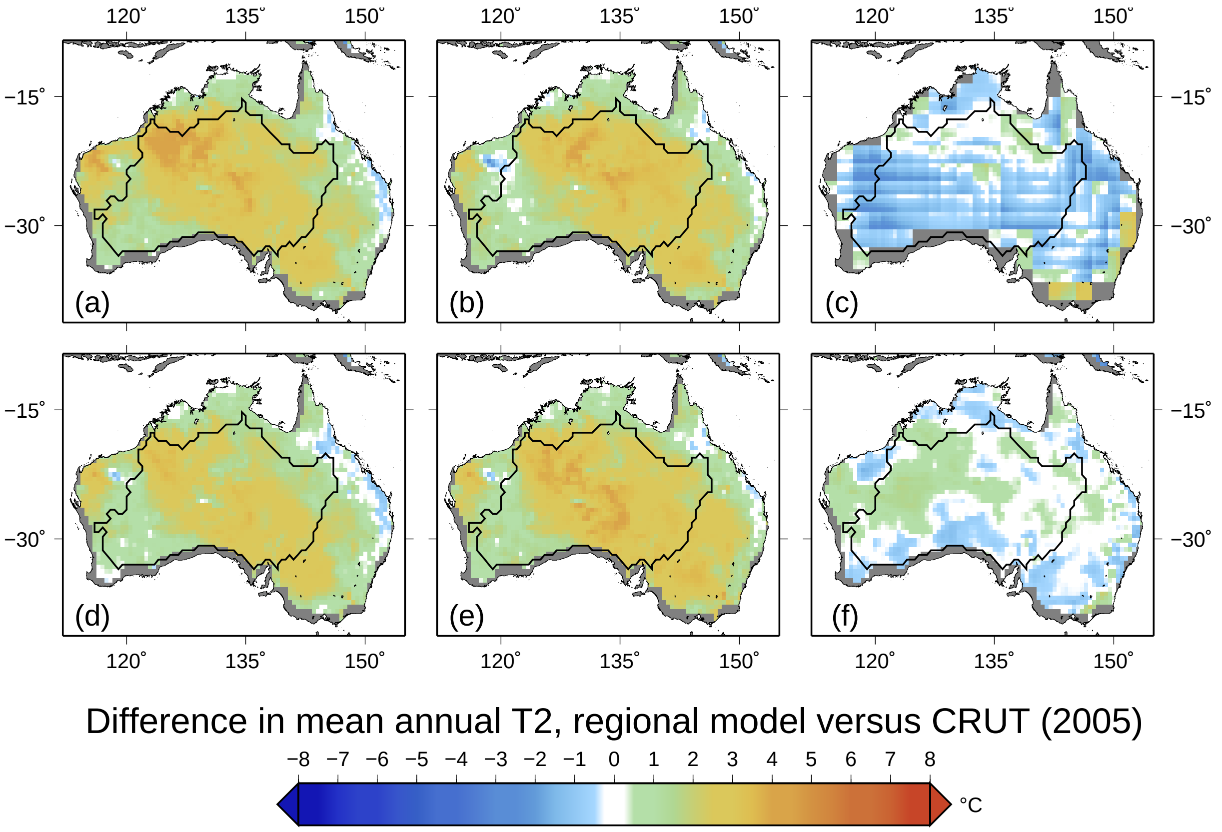

Figure 5.5.: Australian domain: relative differences in annual mean 2m-temperature of downscaled reanalyses with respect to CRUT. (a) NR SST+KF , (b) NR SST+BMJ, (c) NNRP, (d) EI SST+KF, (e) EI SST+BMJ, (f) ERA-INTERIM.

The global reanalysis fields contain a visible dry bias. NNRP returns 100 to 400 mm decreased amounts of precipitation over large extents. In INTERIM the regions of significant negative deviation are concentrated over the north and at some narrow regions along the coasts. All maps in figure 5.3 contain a spot at the same position in the north where precipitation is more than 500 mm below that of GPCC. This is likely to be an error in the GPCC observations. The sparse station density in this region corroborates this assumption.

In summary, it can be stated that for the arid inland locations, the relative uncertainties based on the different observation data lie between 30 and 50 percent. GPCP seems to overestimate precipitation for the coastal regions and the fields from the global reanalysis models are clearly biased towards dryer conditions.

The deviation patterns for the regional WRF simulations are visualized in figure 5.4. For the different model configurations, a similar southwest to northeast gradient is obtained. Along the eastern and northeastern coast the values of GPCC are exceeded by 1500 mm and more. The strongest overestimation is seen for NR SST+KF+FDDA (b) and EI SST+KF (d). When gridded nudging is activated and INTERIM driving is used (e), the areas with 500 to 1500 mm exceeding become considerably smaller. With the BMJ cumulus parametrization, precipitation along the northern coast is better resembled for NNRP driving (c) but along the latitude of 120 ° E, a new maximum is produced. The feature remains also when ERA INTERIM boundary conditions are used (f).

Independent from the used driving data, only for the outermost southwestern part of Australia, the precipitation results from the regional model agree well with the global observation fields. The analysis of precipitation patterns reveals that the regional model has structural problems to resemble the observed annual patterns. Virtually all of the high rainfall rates are obtained during the southern summer months from November to January. The effect is retrieved with both model drivings. However, the deviation strength depends on the physical configuration of WRF. The largest exceedance lies outside of the defined study area. Hence, for the aggregated time series, the deviations should remain within reasonable boundaries. The dryer regions in the south and southwest will compensate for a certain amount of the overestimation that is obtained for the northern part. Disagreement between moisture flux derived water storage variations and GRACE is expected for the November to January period.

Although suffering from the seasonal wet bias, for the Central Australian Basin, with the EI SST+KF+FDDA configuration the most reasonable results are obtained in terms of bias, RMSE (compare fig. 5.6 and tab. 5.1). NR SST+BMJ returns the best performance for the correlation coefficient.

2 meter temperature The north to south deviation gradient obtained from WRF precipitation, is not found for the temperature field. The results of the regional simulations exhibit a very uniform spatial distribution for all three configurations of the regional model. The annual mean deviation fields for 2005 are shown in figure. 5.5. The SST+KF+FDDA runs were omitted because they are almost identical to SST+KF. For all regional simulations, except for the easternmost regions, a warm bias of 0.5 to 3.5 °C is found. Values of 0.5 to 1.5 °C are obtained for most of the coastal regions. The Central Australian plane is about 3 °C warmer than suggested by the observations of CRUT. Furthermore, this region contains spots where the temperature is 4 to 5 ° higher than suggested by CRUT. For both model drivings, no changes are seen when the gridded nudging option is activated. With BMJ cumulus parametrization (b,e), the general deviation patterns remain similar to those of KF. Substantial colder values are seen with NNRP

Table 5.1.: Central Australian basin: bias for monthly time series of precipitation (mm month^{-1}), temperature (°C), and storage change (GRACE GFZ RL 04, mm month^{-1}) (2003/01 – 2006/12). Gridded observation data versus global reanalyses and regional simulations.

	CRUP	GPCC	GPCP	DELP	CRUT	DELT	GRACE
INTERIM	−6.33	−10.63	−11.21	−7.55	0.50	0.37	4.68
EI SST+KF	17.90	13.60	13.02	16.67	2.80	2.67	15.37
EI SST+KF+FDDA	16.94	12.64	12.06	15.71	2.92	2.79	15.82
EI SST+BMJ	20.21	15.91	15.32	18.98	2.94	2.81	14.65
NNRP	−10.30	−14.60	−15.18	−11.53	−0.23	−0.36	3.84
NR KF	10.78	6.48	5.90	9.55	3.76	3.63	15.63
NR SST+KF	18.69	14.39	13.81	17.46	3.16	3.03	16.81
NR SST+KF+FDDA	23.07	18.77	18.18	21.84	3.00	2.87	17.59
NR SST+BMJ	19.28	14.98	14.40	18.05	2.97	2.84	13.67

driving for a stripe along the 120th meridian. As the corresponding precipitation map (fig. 5.4, c) shows, this cold region matches with the elevated rainfall amount of NR SST+BMJ.

The comparison for the time series of the Central Australian basin is shown in the left Taylor Diagram of figure 5.6. The regional simulations exhibit similar performance measures. The seasonal signal is well observed, leading to high correlation values. Compared to the observation data sets, the seasonal amplitude is too small for the results of the regional model. This is caused by the overestimation of temperature during southern hemisphere winter of up to 5.5 °C. Despite of NR const. SST, the summer values and the peak in January are better resembled for all considered configurations of WRF. Nevertheless, a warm tendency of 1 to 2 °C is experienced for these periods. Typical values for the annual bias lie between 2.7 and 3.6 °C for the regional time series and the global data of CRUT and DELT. The measures for the year 2005 can be found in table 5.1. NR const. SST returns a seasonal amplitude similar to CRUT. In the Taylor Diagram, this is depicted by a short distance (i.e. a low RMSE). However, the bias values are relatively high for all months, ranging from 3 to 5 °C. Thus, the NR const. SST configuration has to be rejected in terms of reasonableness.

As already experienced for the other study regions, the global reanalysis fields yield to colder conditions for the annual mean temperature. INTERIM exhibits smaller deviations and, except for the warm bias in the central to western part of Australia, the overall pattern is mainly outbalanced. NNRP contains a more distinct cold bias, ranging from -0.5 to -3 °C. Similar, to the results from the regional simulation, the temperature deviations are not in coherence with those of precipitation.

The analysis of the basin time series shows a very good match between the global observations and INTERIM. Small deviations between 0.5 and 1 °C exist only for the warmest summer months. Not so for NNRP. With respect to CRUT, the amplitude is 2 to 3 °C larger. In winter, a cold bias of about 2 °C is experienced. During summer, NNRP is around 1 °C warmer than CRUT. The mean annual deviation lies around -0.3 °C, in the opposite direction to INTERIM.

5.3. Water Storage Variations

Model comparison Figure 5.8 depicts the uncertainty range in terrestrial water storage variation for GRACE and the atmospheric moisture budget approach for the Central Australian basin.

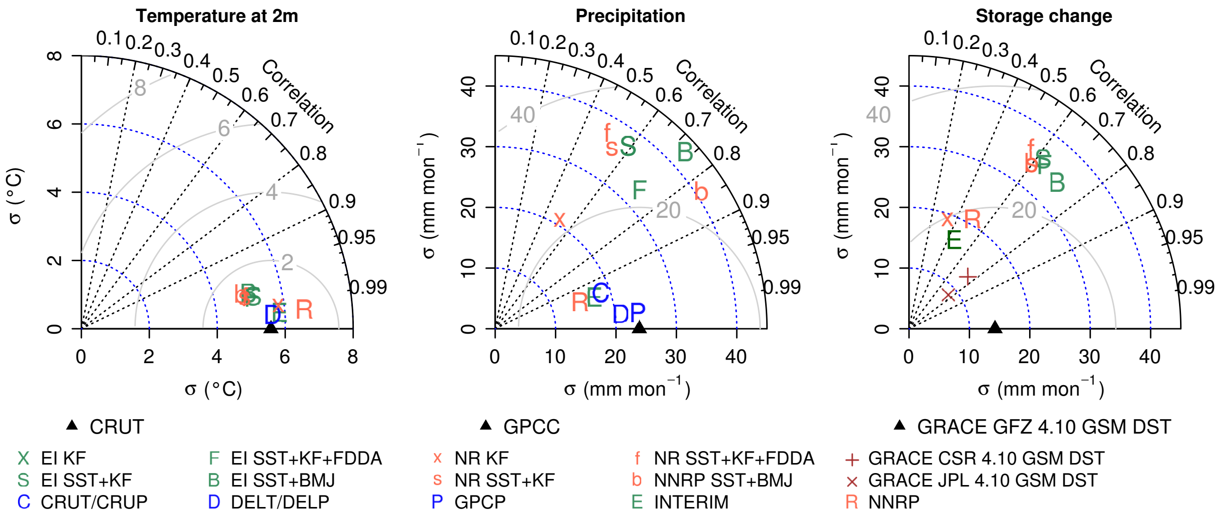

Figure 5.6.: Central Australian basin: Taylor diagram for 2m temperature, precipitation, and water storage change.

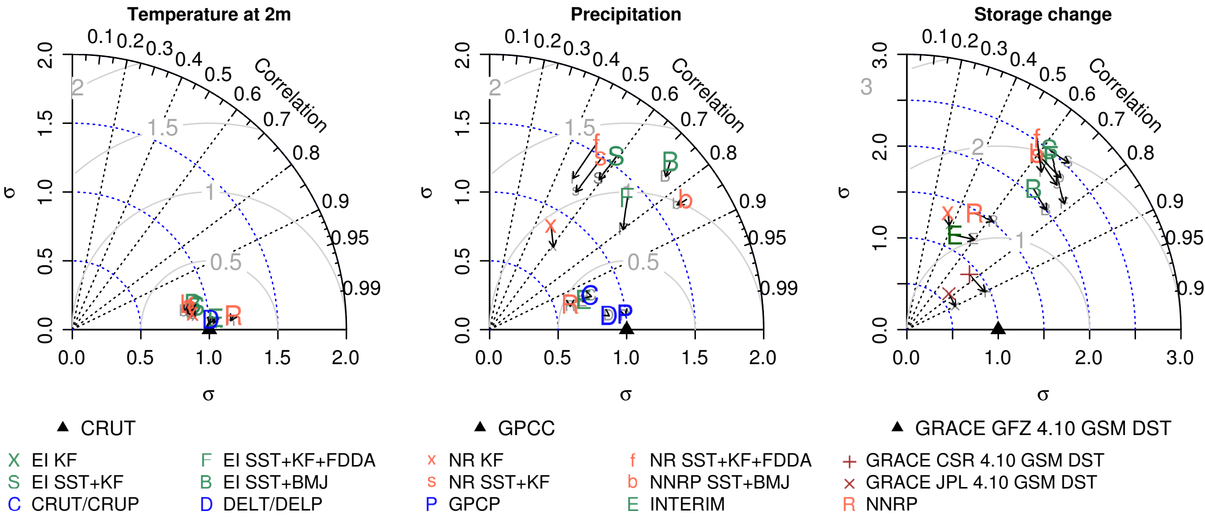

Figure 5.7.: Central Australian basin: Taylor diagram for 2m temperature, precipitation, and storage change. Arrows show improvement if only considering the periods from January to August

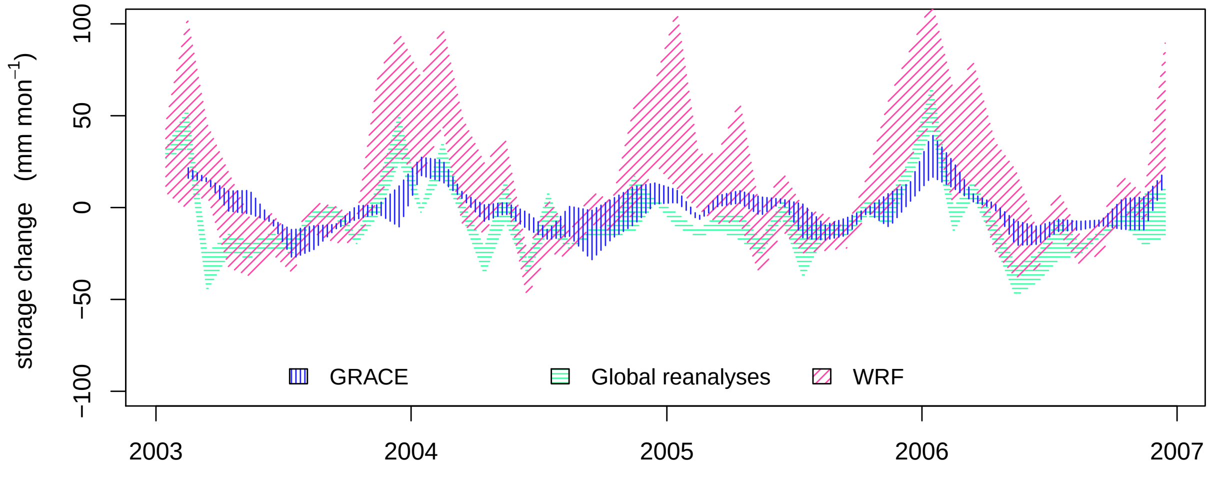

Figure 5.8.: Central Australian basin: total uncertainties in basin water storage change, derived from GRACE (GFZ, CSR, JPL, release 4, Swenson & Wahr (2006) de-striping filter & 500 km Gaussian smoothing applied), global reanalysis (INTERIM, NNRP), and WRF. All atmospheric fields of $-\nabla \cdot \vec{Q}$ are smoothed by a 500 km Gaussian filter.

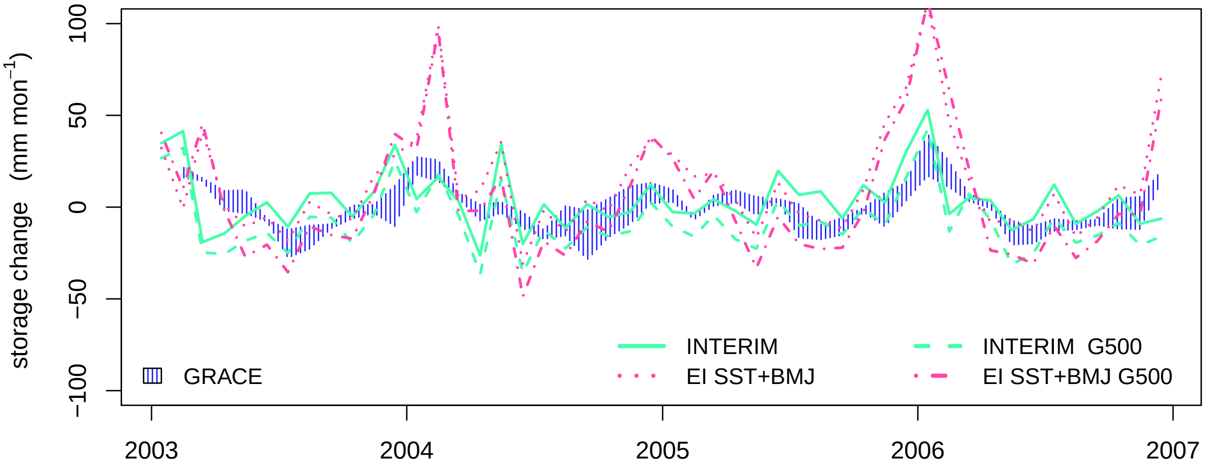

Figure 5.9.: Central Australianbasin: water storage variations and moist suitable global and regional atmospheric models.

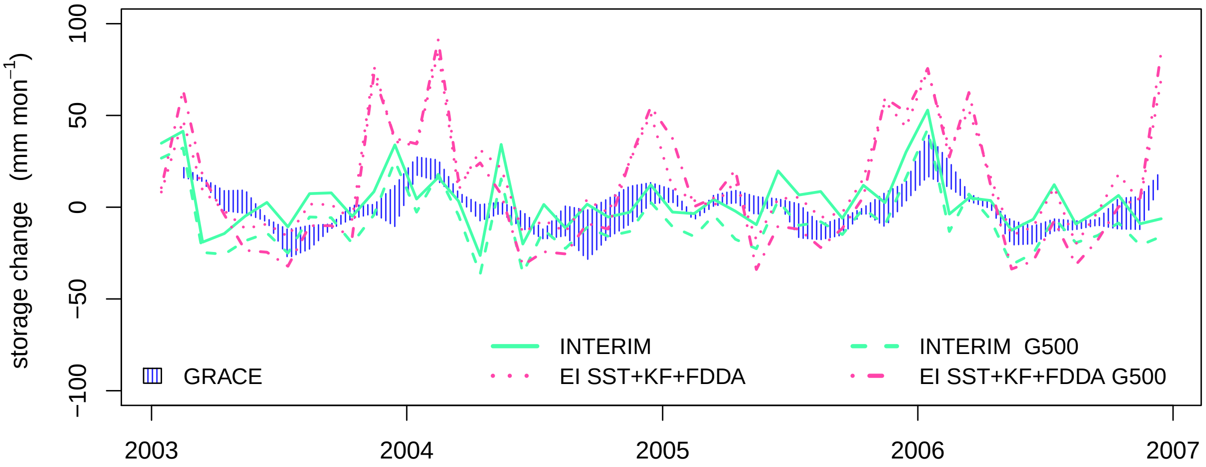

Figure 5.10.: Central Australianbasin: water storage variations and moist suitable global and regional atmospheric models.

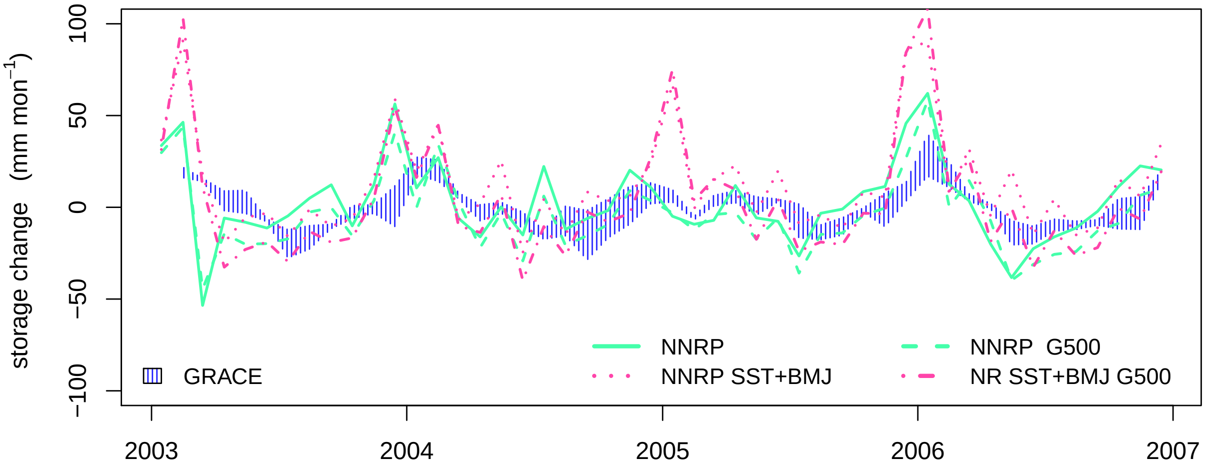

Figure 5.11.: Central Australianbasin: water storage variations and moist suitable global and regional atmospheric models.

All time series show a common seasonal course. Storage recharge usually takes place from December to February or March. For the rest of the year the storage change rate is negative. GRACE varies between -28 and +40 mm month^{-1} with an inter product uncertainty range of 2 to 27 mm month^{-1}, for the 2003-2006 time series of GFZ, CSR and JPL. The global reanalyses show storage change rates between -56 and 70 mm month^{-1} with an inter model uncertainty of 1 to 44 mm month^{-1}. The largest differences are obtained for the regional simulations with a range from -48 to 112 mm month^{-1} and uncertainties between 10 and 100 mm month^{-1}.

The Taylor Diagram on the right side of figure 5.6 depicts the statistical relation of the considered time series of water storage. The pattern of the storage change diagram differs substantially from that for precipitation. In terms or the regional simulations, the best coherence with GRACE GFZ is obtained with EI SST+BMJ. Except for NR const. SST, All other configurations are located around a correlation coefficient of 0.6 and a RMSE value of 30 mm month^{-1}. NR const. SST shows no temporal correlation with the GRACE solutions. Except for NR const. SST, all regional simulation contain a similar wet bias around 15 mm month^{-1}. The values are in similar range to the bias with the precipitation observations.

The global reanalyses are closer related to GRACE with regard to standard deviation and RMSE. However, with values around 0.45 the correlation is rather weak. GRACE itself shows the typical triangle configuration with a reduced standard deviation for JPL. The inter-correlation of the different GRACE products is similar to that of the Chad basin.

Figure 5.9 shows the two time series that are closest related to GRACE. The global and the regional curve share common tendencies. However, the regional model returns much stronger deflections with a positive and negative maximum in January and June, respectively. Spatial filtering increases the storage change rates of the global time series by an amount similar to the inter-GRACE uncertainty bounds. The shift takes place only in one direction so that negative rates become larger. The regional curve is only altered during the cold season from April to October. Altogether, the uncertainty bounds of the atmospheric derived time series exceed those of GRACE.

Reasonable models The validation of basin aggregated time series of precipitation and temperature showed that the global reanalysis of ERA INTERIM outperforms the NCAR/NCEP NNRP product only marginally. The image is further corroborated by the global time series depicted in figure 5.8 and 5.9 to 5.11. Although INTERIM performs better with respect to precipitation and temperature observations than NNRP, the difference in atmospheric moisture budget is very small between the two. Thus, the time series seem to define realistic uncertainty constraints for the global reanalyses and the Central Australian.

In terms of the regionally modeled time series, some configurations of WRF can be defined to be unreasonable. This applies to NR const. SST, the EI SST+KF, and NR EI SST+KF+FDDA. The remaining EI SST+KF+FDDA and the two SST+BMJ configurations return the best coherence with the observations. But as the spatial deviation patterns show, they are far from being perfect. A look at the time series plots of figures 5.9 to 5.11 shows that also for these three regional simulations no significant difference exists with respect to water storage change. Compared to GRACE, EI SST+BMJ gives the best coherence measure although it reaches only the third rank with respect to precipitation. Thus, apart from the large summer peak rates, the three regional time series are considered as reasonable uncertainty measures.

Seasonal performance For the basin averaged time series, the seasonal variation in performance must be assessed from the two different viewpoints of correlation and bias. If all monthly values from September to December are omitted, the correlation coefficient of GRACE and atmosphere derived water storage variation becomes maximized. As visualized by the Taylor diagram of figure 5.7, improvement is seen for all global and regional time series. The gain in performance is not only restricted to storage change. Also for precipitation the coherence is strengthened. EI SST+KF+FDDA clearly outperforms NR SST+BMJ for the selected subset. With respect to storage variation, the overall ranking of the regional results is not changed. But the three WRF simulations that are considered to give the most reasonable results are located close by in the Taylor plot. For the global time series, the performance measures are not significantly altered. No changes are seen for global and regional time series with respect to the temperature.

If not the temporal correlation measure but the mean bias is considered, the best result is obtained for the subset of all April to October values. As figures 5.9 to 5.11 show, the largest difference (>20 mm month^{-1}) between GRACE, reanalyses, and WRF exists for the Australian summer months from November to March.

The high input rates of the regional simulations are related to moisture advection from the tropical regions in the north. Figure 5.12 shows the monthly sum of vertically integrated moisture convergence in combination with the monthly and vertically averaged wind field for December 2005. Positive values depict conditions where precipitation exceeds evapotranspiration. The spatial patterns can be related to the deviation pattern of modeled versus observed precipitation. It is likely, that the high amounts of moisture convergence are caused by the northern boundary conditions of the global driving fields but also by local evaporation from the ocean surface in the regional atmospheric model. High evaporation rates are found for the north and northwest of the Australian mainland. The different configurations of the regional model affect

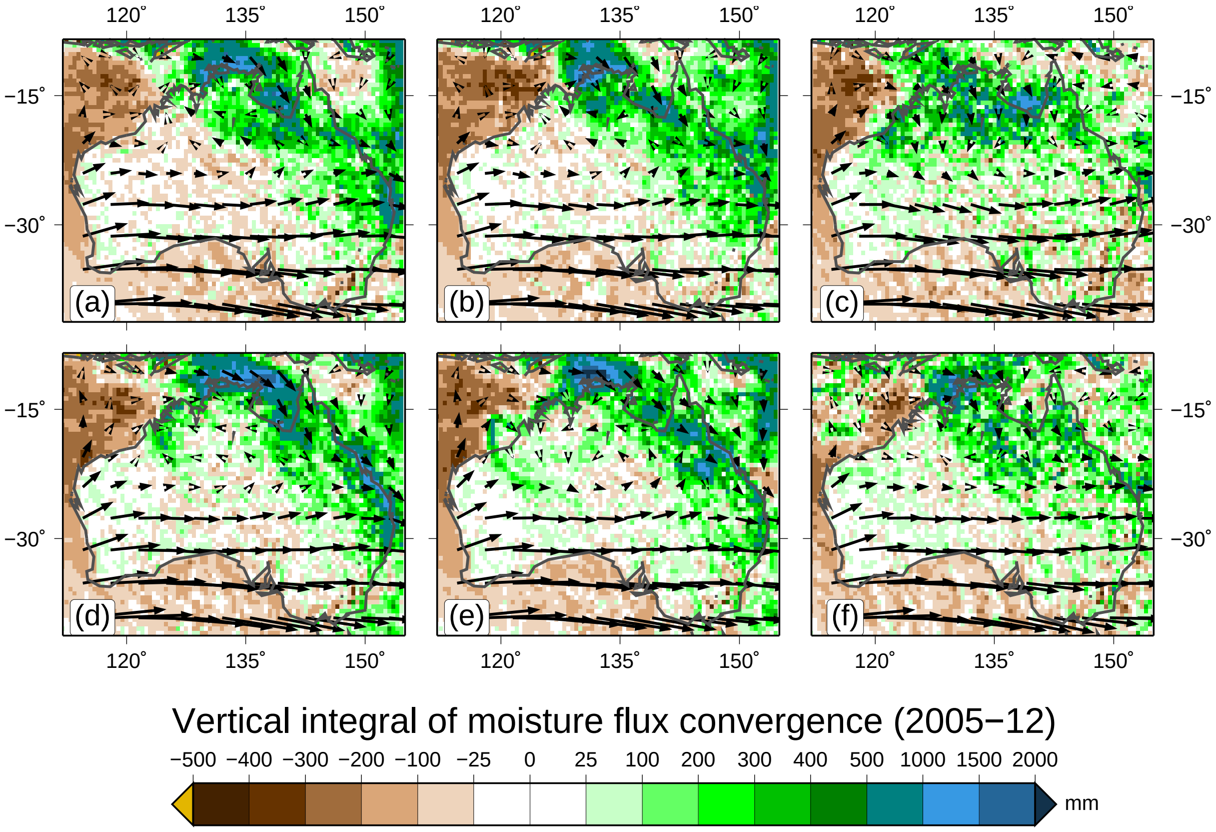

Figure 5.12.: Central Australian basin: vertically integrated moisture flux divergence and vertically averaged wind field (arrows). (a) NR SST+KF, (b) NR SST+KF+FDDA, (c) NR SST+BMJ, (d) EI SST+KF, (e) EI KF+FDDA, (f) EI SST+BMJ.

the circulation patterns in the norther part of the continent where wind speed is relatively slow. This leads to disparate distributions of moisture convergence amounts. The strongest difference is seen between the KF and BMJ cumulus configuration (fig. 5.12 a,b vs. c and d,e vs. f).

It is suggested that by ocean evaporation, too much water is introduced into the regional atmospheric model during these specific months. The ocean boundary is problematic in terms of the water budget as it provides an infinite source. The analysis shows, that the regional model returns unrealistic water fluxes for the summer months for the northern Australian domain. Thus, despite the chosen configuration, the global fields are not outperformed by the regional downscaling approach for these periods. For the remaining months, the two global and the selected regional fields show a similar coherence with GRACE. But mostly, GRACE lies within the uncertainty bounds of the atmospheric water budget derived terrestrial storage variation.

5.4. Performance of the Regionalization

Similar to the findings for the Siberian and the North African domain, the performance of the regional model is not constant with time. The warm bias in temperature varies typically from 1 to 4 °C within a year. Precipitation is strongly overestimated for the Australian summer. Remarkably, the temperature bias reaches its minimum for those periods. During fall and especially for the years 2003-2004, the WRF simulations improve the dry bias of the global reanalyses. With different parametrization of the regional model, a relative improvement of the results is observed. However, for the deviating winter months, it seems that an improved ocean model, leading to a better representation of oceanic moisture advection, could significantly reduce the general precipitation bias.

6

Amazonian domain

The Amazon river is the largest river of the world in terms of volumetric discharge and basin extent. The seasonal amplitude of water storage variations is very large. For the atmospheric water budget analysis, the chosen domain represents equatorial, humid, and monsoonal climatic regions.

6.1. Domain Characteristics

Climate According to the climate classification of Köppen–Geiger (Kottek *et al.* , 2006), the Amazonian river basin subdivides into three major climate zones. The diagrams in figure 6.1 depict the spatial variability. Strong summer precipitation is a main characteristic for the whole domain region. It is linked to an upper tropospheric high pressure system that moves to the north in the winter time. Hence the southern and eastern part of the amazon basin face a dry season in winter (May-August) (Molion, 1987; Labraga *et al.* , 2000). The annual precipitation sum varies from 1,000 mm yr^{-1} in the southeast to more than 5,000 mm yr^{-1} in the northwest (Sombroek, 2001).

Because most of the incoming short wave radiation is converted into evapotranspiration (latent heat flux), the annual variations of air temperature are moderate (26.6± 0.5 °C, Manaus 72 m.a.s.l.) for the monsoonal and humid areas whereas for the winter dry regions the dynamic is more distinct (24.9±1 °C, Aragarcas 345 m.a.s.l.).

Hydrometeorology The high amount of annual precipitation is mainly a result of atmospheric water vapor convergence and local evapotranspiration (Labraga *et al.* , 2000). Lenters & Cook (1995) found that the majority of Amazonian water has a zonal origin, distributed with the northeasterly trades and their counterclockwise rotation. Local evapotranspiration contributes to the atmospheric moisture with 30-34 % (Labraga *et al.* , 2000; Trenberth, 1998). Costa & Foley (1999) provide a comparison of the Amazonian water budget, derived from two atmospheric reanalysis models. Total annual precipitation defined as 100 %. For NCAR/NCEP and ECMWF, evapotranspiration amounts 62/58 % and contributes to rainfall with 30/25 %, discharge represents 38/42 % of precipitation, respectively.

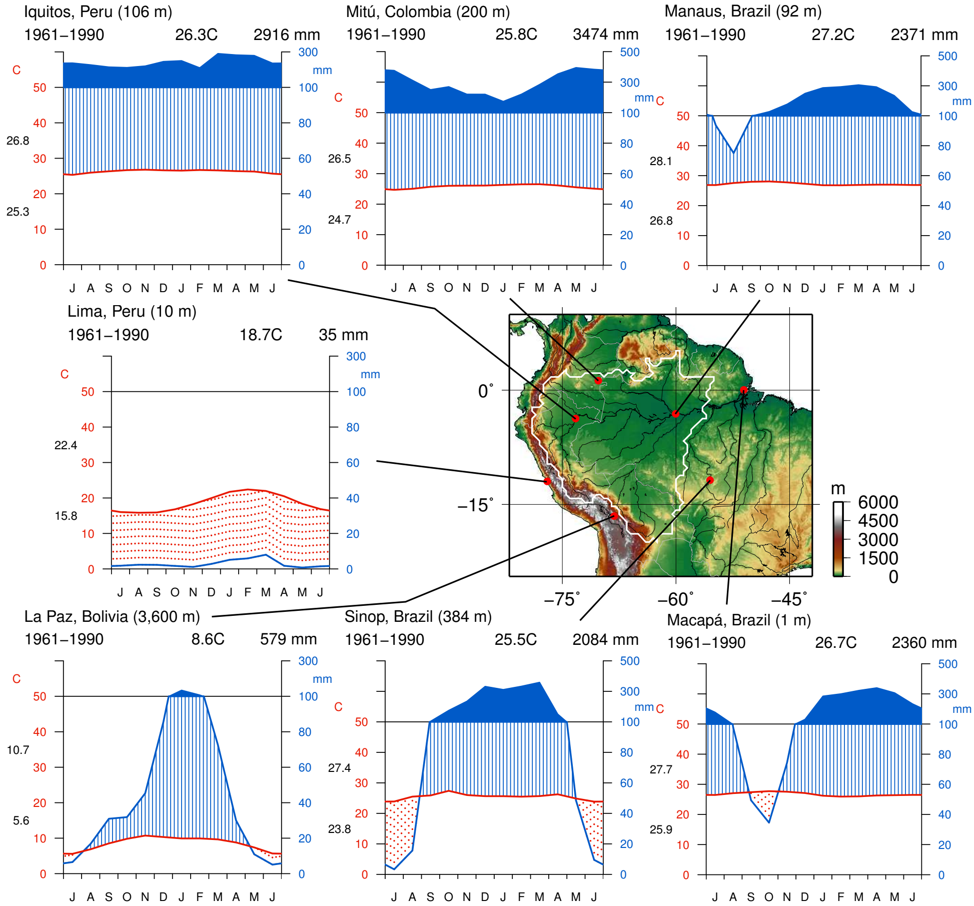

Figure 6.1.: Amazonian domain, orography and climate. The white contour depicts the Amazonian river basin upstream of Óbidos.

Because of the large water storage capacity of the central flood plains, the annual variation in evapotranspiration is minimal. Even during dry periods, there is sufficient water supply for the tropical vegetation. Hence, the temporal variations that are seen in precipitation input propagate into the river discharge, although becoming largely smoothed. The hydrograph at Óbidos (not shown) has its maximum in winter (April to July) (Fekete *et al.* , 2000). This is remarkable because, the southern and southeastern part of the basin is facing its dry season, at this time.

River basin The catchment area of the Amazon river covers 7,050,000 km^2. The elevation ranges from the Atlantic Ocean to over 5000 m.a.s.l. in the Andean mountains. about 10,000 tributaries contribute to the main stream. The comparison of Costa & Foley (1999) concludes with a mean annual discharge to the Atlantic of 190,000 to 200,000 $\text{m}^3\ \text{s}^{-1}$. The main branch has a length of about 6,500 km.

The lower reach of the river is influenced by ocean tides. The *Pororoca* called wave is a worldwide known phenomenon. Therefore, measuring the discharge is very complicated at the last kilometers of the stream and thus the last gauging station that is referenced by the GRDC is located at Óbidos, Brazil, 537 km before the outlet. The catchment area and the length of the upstream mainstem reduce to 4,622,624 km^2 and 3,869 km, respectively. However, with 176,177 $\text{m}^3\ \text{s}^{-1}$ (1,197 mm yr^{-1}), the mean basin discharge is almost equal to that of the river mouth (Fekete *et al.* , 2000). By defining the Amazon river basin outlet at Óbidos, the contribution of some major tributaries like the Tocantis, the Tapajós, and the Xingu is not being accounted for.

6.2. Validation

Orography The elevation fields of the atmospheric models (Fig. 6.2) differ considerably at the Andean mountain ridge. WRF and INTERIM resolve the highest peaks, whereas NNRP gives a maximum height of hardly 4,000 m. Moreover, the western coastline exceeds the suggested course with whole pixels ($\approx 275km$). The two white inland pixels of NNRP mark negative elevation levels. Like for the other domains, the wave pattern showing up over the ocean in INTERIM is caused by values that are larger than zero. At ECMWF, instead of elevation only the geopotential field is available.

Precipitation Figure 6.3 shows the 2005 annual sum of gridded continental precipitation from global data sets and reanalysis models, relative to GPCC. White refers to deviations of maximum $\pm 100\,mm\,yr^{-1}$. The station network density of GPCC is printed in (a). Every dot depicts one station in a $0.5\,^{\circ}\times\,0.5\,^{\circ}$ gridcell. Within the selected catchment the measuring points are distributed more or less uniformly.

Compared to GPCC, CRUP (b) is 30-40 % wetter in the northern part of the domain (Orinoco region), and 30-50 % dryer over the amazon catchment. DELP (d) suggest a higher amount of precipitation in the center but dryer conditions towards the east. GPCP (e) is wetter at the southeast and up to 2,000 mm dryer in the west. In general, all three products are dryer than GPCC over the Andes.

The re-analysis fields of NNRP (c) and INTERIM (f) show stronger deviation amounts than the gridded data. INTERIM contains spots with three times elevated rainfall but also regions with strongly decreased annual sums. NNRP stays in the same range, albeit the spatial distribution differs a little bit from INTERIM.

The annual fields for the years 2003 to 2006 contain similar spatial deviation patterns. As a conclusion it can be stated that uncertainty of the gridded data sets is in the range of 1,000 mm yr^{-1} which is about 50 % of the annual mean. By averaging over the Amazon catchment, the spatial differences cancel out. The catchment sums for the year 2005 are 2,286 mm for GPCC, 2,077 mm for GPCP, 2,083 mm for CRUP, 2,206 mm DELP, 2,385 mm for INTERIM, and 2,224 mm for NNRP. For 2005 the annual sum of precipitation is 2,163 ± 101 mm and 2,305 ± 114 mm for the gridded data and the reanalysis, respectively. Thus for the Amazon catchment, the reanalysis model have a slight wet bias, but the overall uncertainty is similar to that of the gridded data sets.

Figure 6.4 depicts the 2005 annual precipitation sum observed from WRF, relative to GPCC. The comparison comprises two different model drivings (NNRP (NR), INTERIM (EI)) and three model parametrization setups (abbreviations defined in table A.1). The results exhibit remarkable deviations for the different model runs. KF+SST (a and c) leads to a strong overestimation for the whole domain, except for the west and the northwestern coastal region. Here, the deviations remain within the uncertainty range of the global data sets. When SST is set constant (c and f), the dryer conditions of KF+SST become intensified. For both simulations (KF+SST and KF SST const.) NR driving produces less rainfall than EI. Enabling gridded nudging (b and e) results in a globally reduced precipitation amount. With this configuration, the values of EI are shifted towards the uncertainty range of the global data sets, whereas by using NR model driving, an underestimation of 50-100 % is experienced with respect to GPCC.

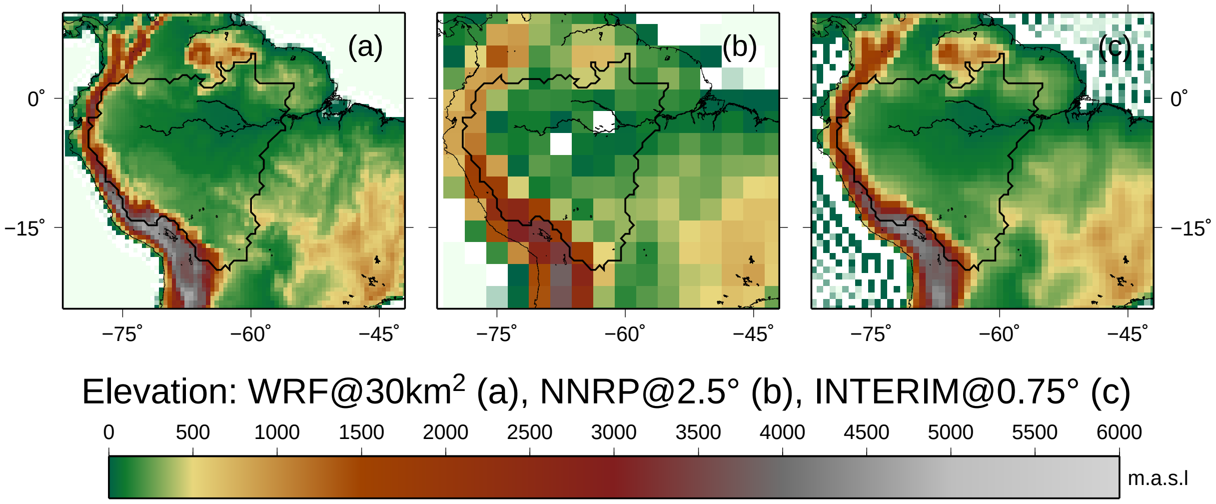

Figure 6.2.: Amazon domain: DEM configuration for WRF (a) and the reanalysis models of NCAR/NCEP (b) and ECMWF ERA-INTERIM (c).

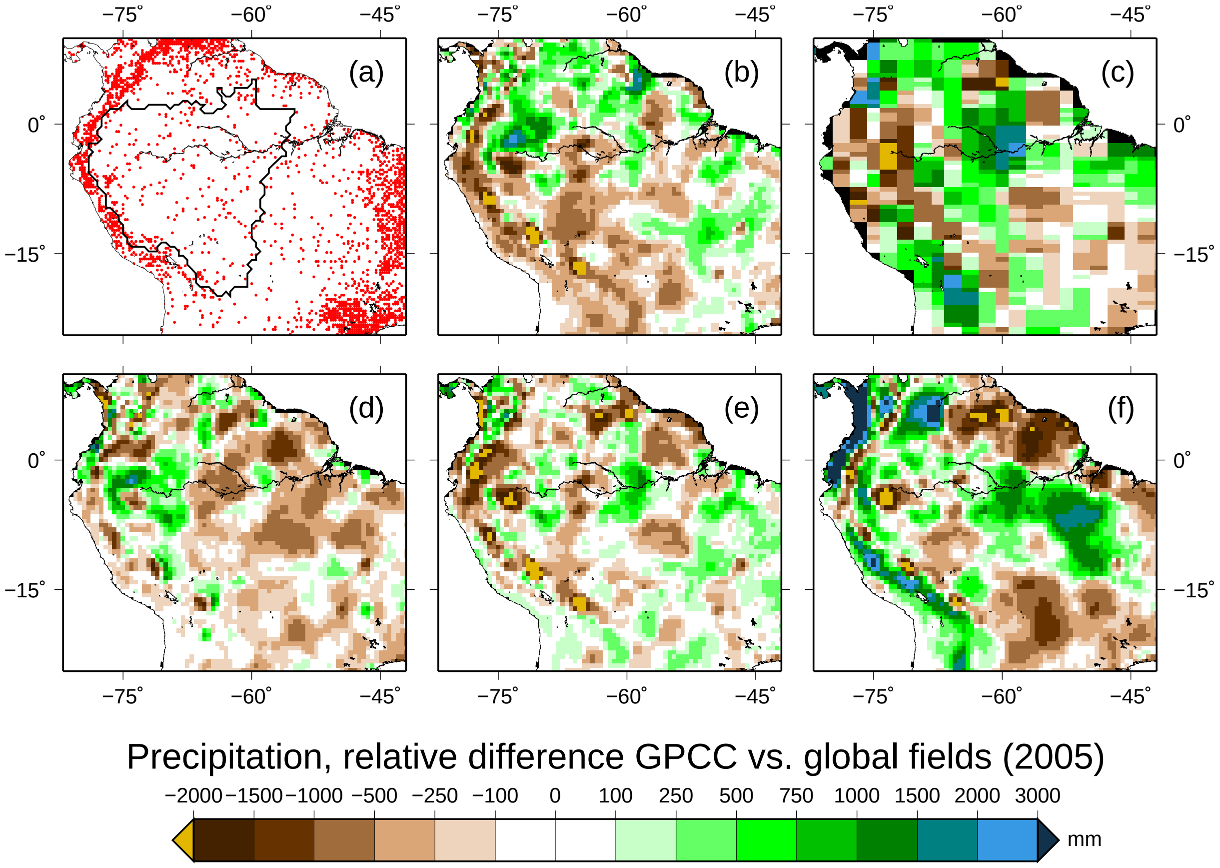

Figure 6.3.: Amazon domain: relative difference in annual precipitation observations and global reanalyses with respect to GPCC. (a) GPCC Station network, (b) CRUP, (c) NNRP, (d) DELP, (e) GPCP, (f) INTERIM.

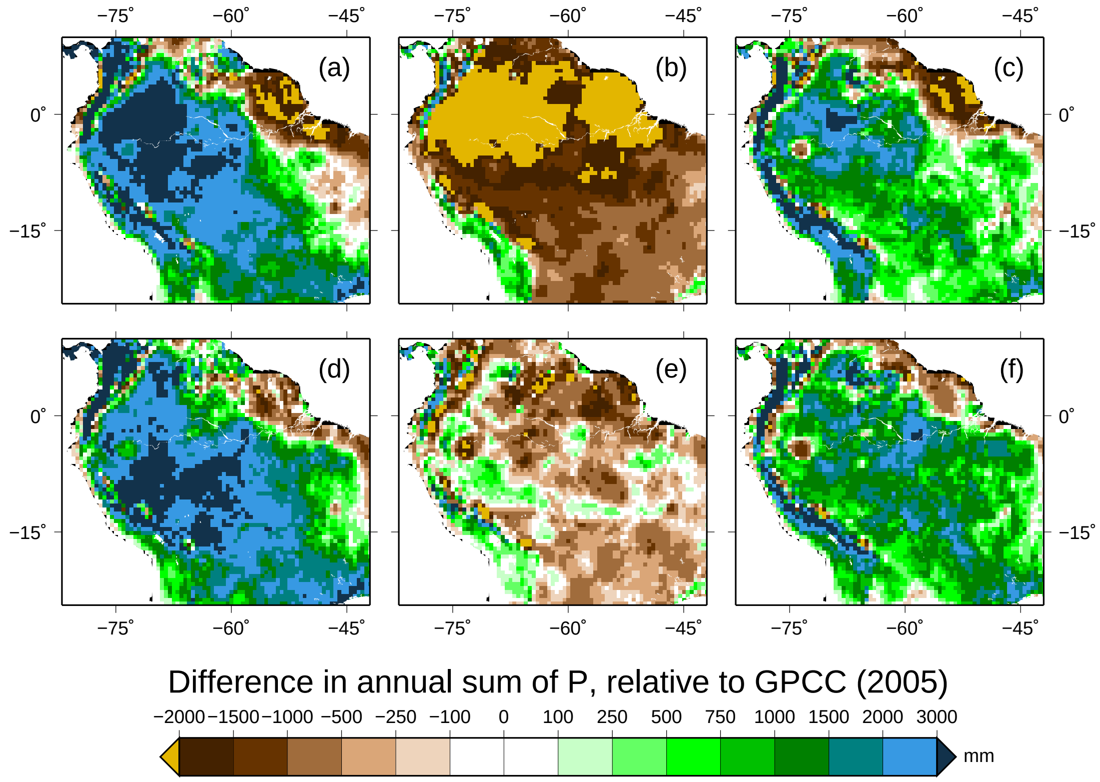

Figure 6.4.: Amazon domain: deviation in annual precipitation of downscaled reanalyses with respect to GPCC. (a) NR SST+KF , (b) NR SST+KF+FDDA, (c) NR KF SST const., (d) EI SST+KF, (e) EI KF+FDDA, (f) EI KF SST const.

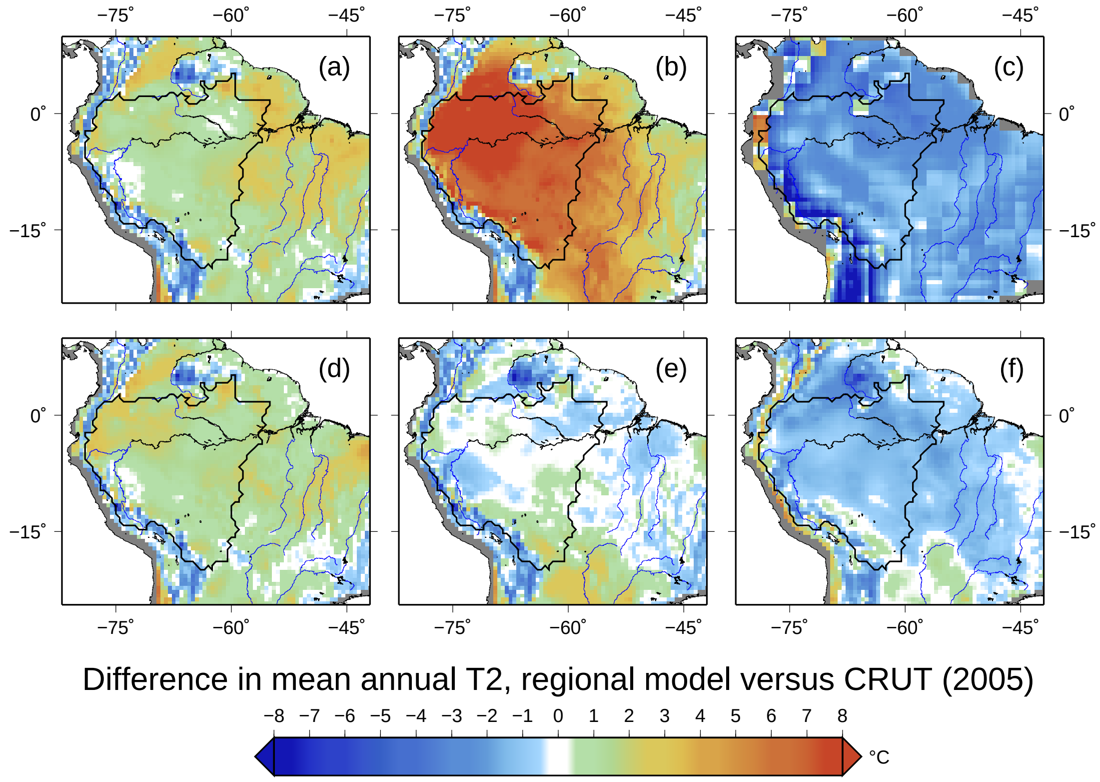

Figure 6.5.: Amazon domain: relative differences in annual mean 2m-temperature of downscaled reanalyses with respect to CRUT. (a) NR SST+KF , (b) NR SST+KF+FDDA, (c) NNRP, (d) EI SST+KF, (e) EI KF+FDDA, (f) ERA-INTERIM.

The Taylor Diagram (Fig. 6.8) compares the statistical properties of the catchment averaged precipitation time series. Again, GPCC is chosen as reference. As already indicated by the spatial analysis, except for EI+SST+KF+FDDA, significant biases are experienced. However, the correlation coefficients remain within the range of the global reanalyses (INTERIM and NNRP). Only NR SST+KF+FDDA departs from the rest. The NR simulation suggest a slight improvement in correlation compared to NNRP. But the uncertainty in the global data sets neutralizes that. The regional simulations with INTERIM driving result in decreased correlation measures, except for EI SST+KF+FDDA. Only this regional model configuration is able to produce reasonable result in terms of basin-averaged time series within the uncertainty range of the evaluation data sets. The most inappropriate setup of WRF seems to be with constant SST. Without the constraint of spectral nudging, the BMJ cumulus scheme tops the KF. The strong deviation of the NR SST+KF+FDDA configuration does not seem to be a problem of the regional model and might be caused by deficiencies in the NNRP driving data.

2 meter temperature For the Amazon region both data sets, CRUT and DELT, are in close agreement. Deviations are generally less than 1 °C throughout the domain. Hence, CRUT is chosen for the evaluation of the regional simulations and the global reanalysis models.

The comparison of global fields and CRUT (Fig. 6.5) yields colder conditions for the modeled variables. INTERIM underestimates temperature by 0.5 to 1 °C, NNRP contains a cold bias of 1 to 3 °C. For the Andean mountains, both reanalyses are warmer than the observations.

The deviation patterns of the annual 2-meter temperature of the regional simulations relate well to the results of the precipitation analysis. For both, EI and NR, KF+SST (a and d) leads to an overestimation of up to 3 °C, except for the mountainous regions where CRUT suggests colder values. However, precipitation overestimation correlates with temperatures increased by about 1 °C. For higher values the amount of rain is underestimated by the model. The large negative bias obtained from NR SST+KF+FDDA (Fig. 6.4, b) goes along with a 5 to 8 °C overestimation in temperature. While the SST+KF simulations are very similar, with constant SST strong deviations are experienced depending on the driving data used. No maps are shown for SST const. Nevertheless, with this configuration EI is very close to EI SST+KF (d) and NR has resembling spatial patterns with NR SST+KF+FDDA (b) although the maximum is shifted

Table 6.1.: Amazon basin: bias for monthly time series of precipitation (mm month^{-1}), temperature (°C), and storage change (GRACE GFZ RL 04, mm month^{-1}) (2003/01 – 2006/12). Gridded observation data versus global reanalyses and regional simulations.

	CRUP	GPCC	GPCP	DELP	CRUT	DELT	GRACE
INTERIM	19.13	7.87	30.40	14.61	−1.12	−1.25	−9.12
EI KF	159.07	150.89	172.55	156.79	1.72	1.58	84.76
EI SST+KF	209.27	198.02	220.54	204.75	0.98	0.84	124.12
EI SST+KF+FDDA	−14.79	−26.05	−3.52	−19.31	−0.19	−0.32	−24.15
EI SST+BMJ	131.92	120.67	143.19	127.40	0.46	0.32	46.31
NNRP	9.73	−1.53	20.99	5.21	−2.56	−2.70	−52.65
NR KF	10.40	−0.86	21.66	5.88	2.99	2.85	−20.83
NR SST+KF	235.84	224.58	247.10	231.32	0.87	0.73	146.17
NR SST+KF+FDDA	−123.96	−135.22	−112.69	−128.48	5.06	4.92	30.03
NR SST+BMJ	145.06	133.80	156.32	140.54	0.29	0.15	53.89

towards the East. SST+BMJ (not shown) is almost identical to SST+KF (a and d) but with a much lower bias.

The statistical properties for the catchment averaged time series are depicted in table 6.1 and figure 6.8. As can be seen from the Taylor diagram, most of the variables have a correlation coefficient between 0.8 and 0.9. The main differences manifest in the bias corrected RMSE and in the absolute bias. For the 2003–2006 period, NNRP and INTERIM are about 2.6 and 1.2 °C colder than the global data sets. Contrarily, all regional simulation show a warm bias. Depending on the parametrization, the values range from ≈ 0.3 to ≈ 5.7 °C. In terms of correlation, the regional model is not able to add value to the global fields. EI SST+KF+FDDA attains the best result with respect to bias, correlation, and bias corrected RMSE. Without gridded nudging applied, for precipitation, it seems that constant SST leads to a better resembling than SST+BMJ. This is not the case, because the spatial patterns look much better with SST+BMJ. Const. SST causes a northeast to southwest gradient over the catchment. Coincidentally, by averaging, the differences cancel out. A good result for the wrong reasons. Hence, also for temperature, SST+BMJ serves best for an unconstrained simulation. NR driving is critical, when FDDA is turned on.

6.3. Water Storage Variations

Ensemble comparison The remarkable deviations that are found for temperature and precipitation patterns and time series persist also for the dynamics of water storage change. Figure 6.6 gives an overview on storage variations derived from GRACE and $-\nabla \cdot \vec{Q} - D$. For the global reanalyses, the uncertainty range remains almost constant with time. The ensemble of WRF simulations generates a larger range for the rainy season, but is in return more confident for the Winter months (May–August). Compared to the hydro-meteorologic models, the GRACE ensemble (GFZ, CSR, JPL) displays a relatively small uncertainty. In general, all three data types are common in terms of seasonality. This leads to high correlation measures for most of the time series with respect to GRACE. The statistical properties of the single time series are de-

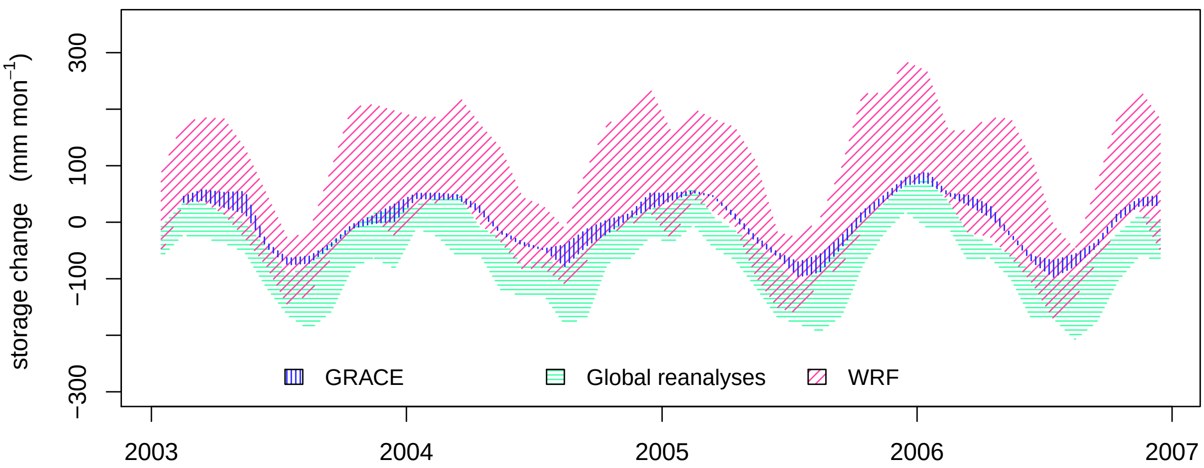

Figure 6.6.: Amazon basin: total uncertainties in basin water storage change, derived from GRACE (GFZ, CSR, JPL, release 4, Swenson & Wahr (2006) de-striping filter & 500 km Gaussian smoothing applied), global reanalysis (INTERIM, NNRP), and WRF. All atmospheric fields of $-\nabla \cdot \vec{Q}$ are smoothed by a 500 km Gaussian filter.

picted in the right panel of the Taylor Diagram (Fig. 6.8). It is obvious that storage change and precipitation share common features. However, some time series have differing performance. E. g. the NR SST+KF+FDDA simulation that shows a high disagreement for temperature and precipitation, far away from the corresponding global NNRP fields, is now very close to NNRP and also to GRACE. Therefore this simulation should be rejected, although it seems to be in good agreement with the satellite data. A comparison of $P - E$ (symbol **'1'** in fig. 6.8) and $-\nabla \cdot \vec{Q}$ shows significant deviations. As NR SST+KF+FDDA is relaxed towards the global fields of moisture, temperature, and wind, it is logical that global and regional model are very close by in the diagram. With EI SST+KF+FDDA, the deviations in $P - E$ and $-\nabla \cdot \vec{Q}$ are of minor extent. Again, global and regional time series are very connected to each other. With other settings of WRF, the correlation with GRACE is surprisingly uniform (≈ 0.9), except for the EI KF and EI SST+KF runs.

Reasonable models By comparing the performance of the different WRF simulations and their respective global fields with gridded observations of temperature and precipitation, viable configurations and models can be separated from physically unrealistic representations of the hydro-meteorological cycle.

For NNRP, fields from the global model are closest to the observation data sets. With the tested configurations, by dynamic downscaling, no significant improvement is seen for time series correlation and the bias corrected RMSE is strongly increased. The same applies to ECMWF driving, except for the EI SST+KF+FDDA setup of the regional model. For precipitation, correlation of the global and the regional model remains within the uncertainty range of the four gridded observation data sets. In the winter months (May–August) when rainfall has its annual minimum, the global model shows a tendency of overestimation while the regional simulation results in too dry conditions. In INTERIM, T2 is biased by approximately -1.2 °C. However, the time series is very congruent with CRUT. EI SST+KF+FDDA contains a bias of 0.25 °Cbut produces warmer summer and colder winter conditions compared to the observations. Overall, despite their drawbacks, INTERIM and EI SST+KF+FDDA are the most reasonable global and regional model representations of hydrometeorology for the Amazon basin.

Figure 6.7 depicts the corresponding time series of spatially filtered (G500), and unfiltered basin averages of water storage variations and their relation to GRACE. To INTERIM, spatial

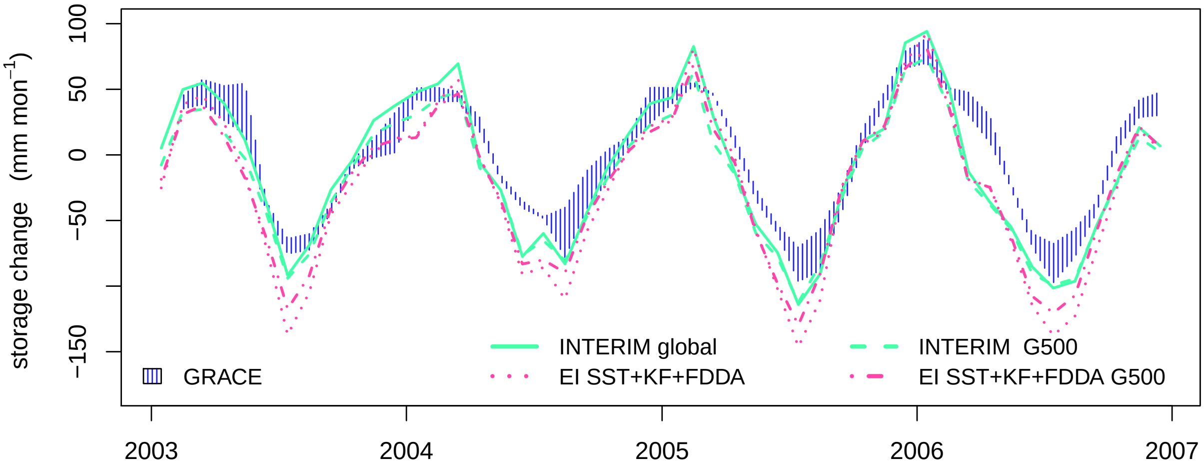

Figure 6.7.: Amazon: basin water storage variations and moist suitable global and regional atmospheric models.

filtering is most effective at the input peaks of the rainy season. Moisture flux derived storage variations indicate dryer conditions as it is the case for GRACE. This is mainly caused by elevated depletion values in the Winter season. EI SST+KF+FDDA is almost identical to the INTERIM. In Winter, the amount of storage depletion is larger for the regional model.

The long term mean (2003–2006) of storage variation ranges from -1.1 to 0.8 mm month^{-1} for the different GRACE products. Interim and EI SST+KF+FDDA show a negative balance of -9.8 and -23 mm month^{-1} for the unfiltered fields and -17.8 and -22.1 mm month^{-1} for the filtered fields, respectively. It cannot be clearly defined how much of this deviation is caused by uncertainty in the discharge measurements. However, the bias between the global reanalysis and the regional simulation leads to the conclusion that the water budget of the latter is not exactly balanced.

Seasonal performance The coherence of the time series for temperature, precipitation, and storage change varies for specific months and seasons. The correlation coefficient for precipi-

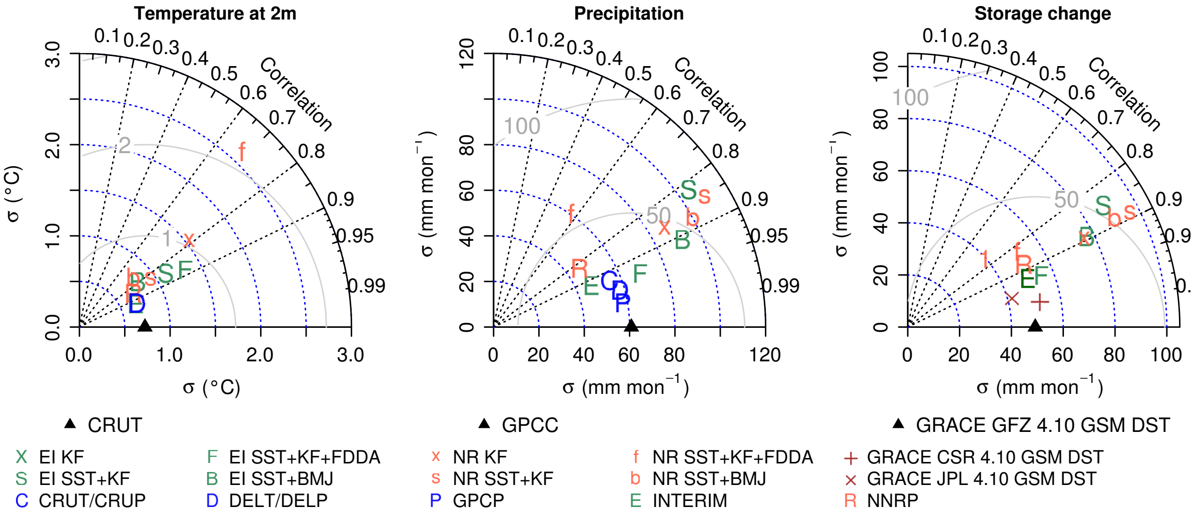

Figure 6.8.: Amazon basin: Taylor diagram for 2m temperature, precipitation, and water storage change.

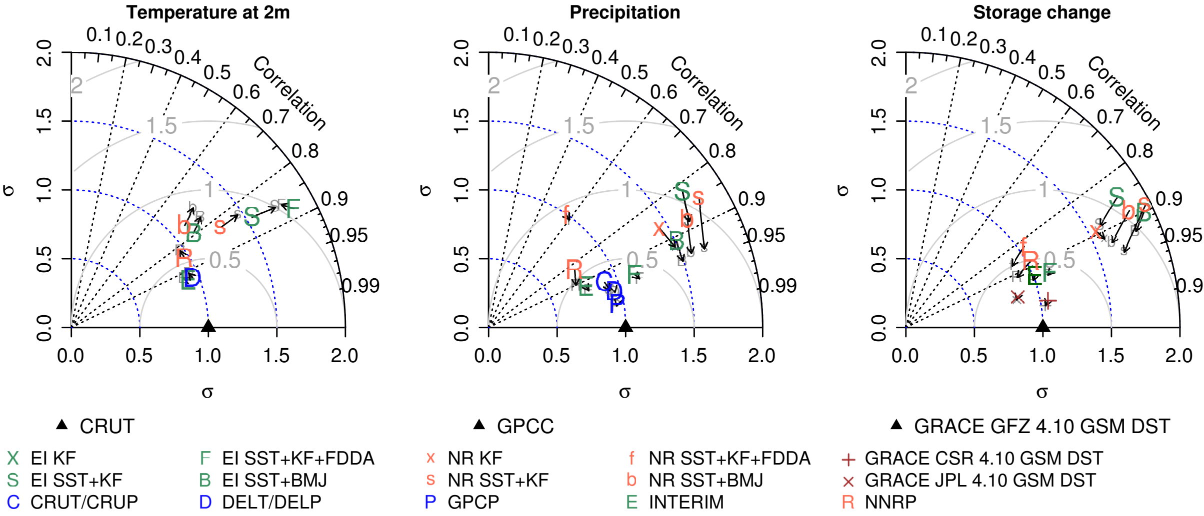

Figure 6.9.: Amazon basin: Taylor diagram for 2m temperature, precipitation, and storage change. Arrows show improvement if only considering the periods from January to September

tation of EI SST+KF+FDDA and GPCP increases from 0.95 to 0.98, if all October to December values are neglected. Of course, changes are also experienced for the water storage variations. Figure 6.9 shows the effects of neglecting specific months of the time series. The plots are normalized to the standard deviation of the reference data set. The arrowheads indicate how standard deviation, correlation coefficient, and bias corrected RMSE will change if only the January to September values for the years 2003 to 2006 are considered.

Large differences in model performance are seen for the regional simulations. The correlation coefficient for precipitation improves by 0.05 to 0.1. Simultaneously, the RMSE is reduced. For the basin storage dynamics, similar patterns are found. Remarkably, by improving the water budget of the regional model, the representation of temperature is deteriorated. The global time series show only modest alteration. However, slight approvement is perceived. EI SST+KF+FDDA realigns similar to the global variables.

6.4. Increased Regional Model Resolution

In WRF, several physical processes are computed via generalization schemes on the sub-grid scale. E.g. convective cloud and precipitation processes or exchange in the planetary boundary layer cannot be resolved by meshes larger than 4 km. The standard resolution of WRF in this study is 900 km^2, or an edge length of 30 km, respectively. For the Amazon river, except for EI SST+KF+FDDA, the water storage variations derived from the regional atmospheric model vastly overestimate summer rainfall. There arises the question whether an increase in horizontal model resolution leads to more reasonable results. Unfortunately, the computational demand for a 4 km simulation of the Amazonian domain is too high. As a compromise, a one year simulation in 10 km is performed with direct downscaling (no nesting) of the global fields from ERA-INTERIM. Hence, the cumulus parametrization scheme cannot be turned off. But the refinement allows for a better representation of spatial heterogeneity in the regional model.

For testing the effect of increasing the spatial resolution, the EI SST+KF configuration is reprocessed for the year 2001. This covers only the period that is considered for ordinary model spinup. However, from the other regional simulations it is experienced that the conspicuous deviations in water storage dynamics already commence during the first year.

Precipitation and temperature For the year 2001, the spatial deviation patterns for precipitation and 2-meter temperature with respect to GPCC and CRUT are depicted in the figures 6.10 and 6.11. (a) represents the 10 km run, (b) the standard 30 km run, and (c) the respective field of the global driving model, ERA-INTERIM.

For precipitation the 10 km simulation (a) reveals remarkable deviations in the spatial distribution pattern. The area where rainfall exceeds GPCC by more than 2,000 mm yr^{-1} becomes reduced. The white colored region in the eastern part of the domain is also increased. In the northeastern part of the river basin, the results change from under- to overestimation. Despite the experienced improvements, the 10 km WRF is close to the skill of the 30 km runs (fig. 6.4 (e)) albeit still worse than the global reanalysis (c).

In terms of the near surface air temperature (fig. 6.11), the 10 km WRF simulation outperforms the coarser one. Large scale. Most of the too warm regions in (b) vanish when the increased model resolution is applied (a). However, overestimation is still seen for the eastern and northwestern part of the domain. Within the boundaries of the Amazon basin, the annual bias is considerably reduced and the deviations range from -0.5 to about +1 °C.

The basin averaged time series (fig. 6.12) corroborate those results. The dotted line of the

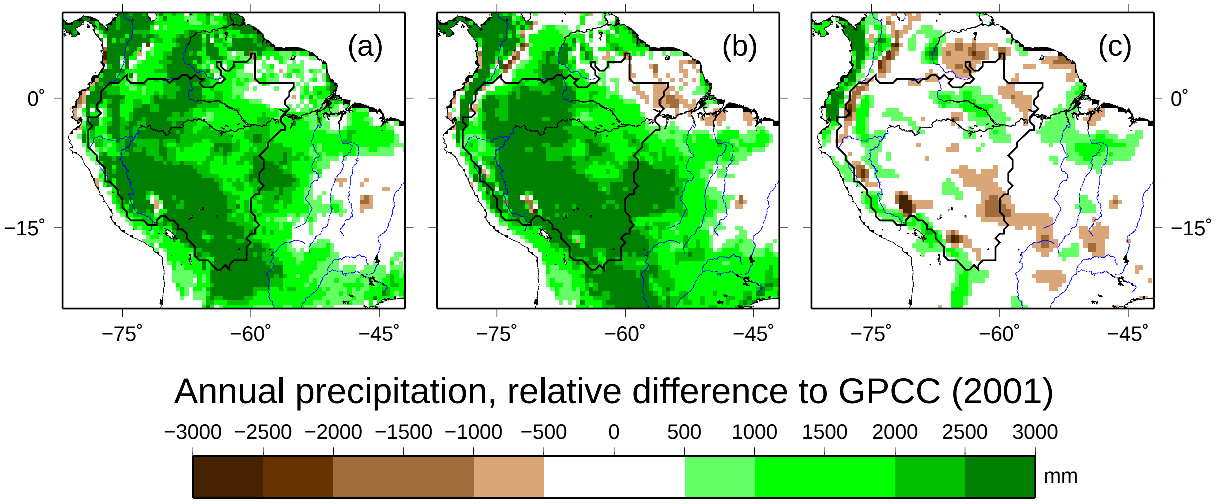

Figure 6.10.: Deviation in 2001 annual precipitation with respect to GPCC: EI SST+KF 10 km (a), EI SST+KF 30 km (b), ERA-INTERIM global reanalysis.

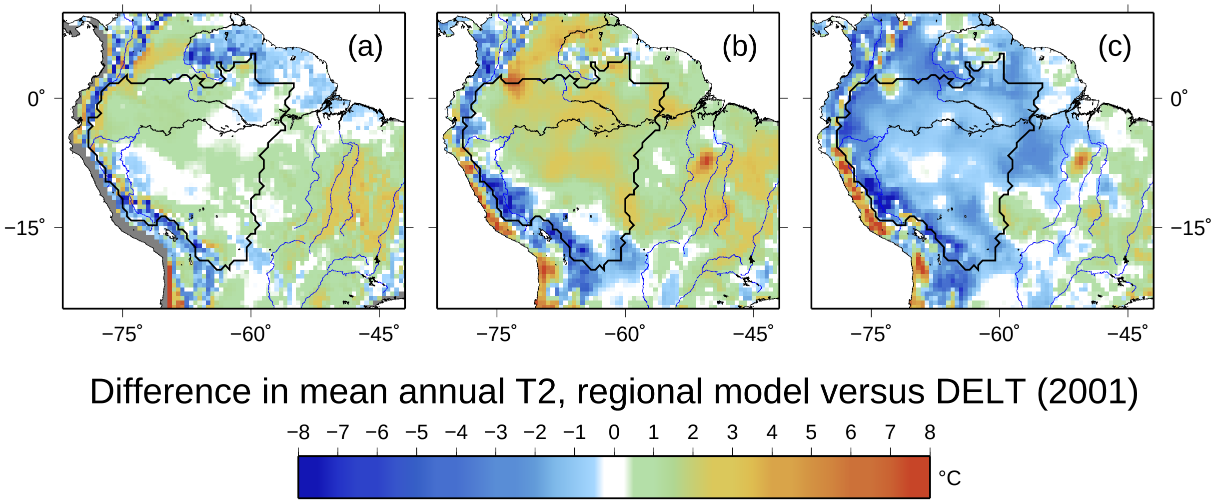

Figure 6.11.: Deviation in 2001 mean annual 2m-temperature with respect to DELT: EI SST+KF 10 km (a), EI SST+KF 30 km (b), ERA-INTERIM global reanalysis.

10 km simulation is always below its 30 km counterpart. However, especially in southern hemisphere summer, the deviation with the observed line (DELT) is still high.

The annual course for precipitation shows a similar annual response. With respect to GPCC, large overestimation is perceived during the summer period. In winter the absolute differences become smaller, although the relative errors remain high. The comparison of the two WRF simulations with 10 and 30 km does not lead to a decided preference. The deviations between the two time series seem to occur randomly.

Altogether, it can be stated that the spatial patterns for precipitation and temperature improve with increasing horizontal resolution of the regional atmospheric model. However, if the basin averaged time series are considered an improvement is only seen for temperature. It would be of interest to further increase the model resolution, so that cumulus parametrization becomes obsolete. As this implies a computational very expensive task (30 km = 24,436 cells, 10 km = 294,385 cells, 5 km ≈ 1,500,000 cells), such a simulation cannot be performed within the frame of this study.

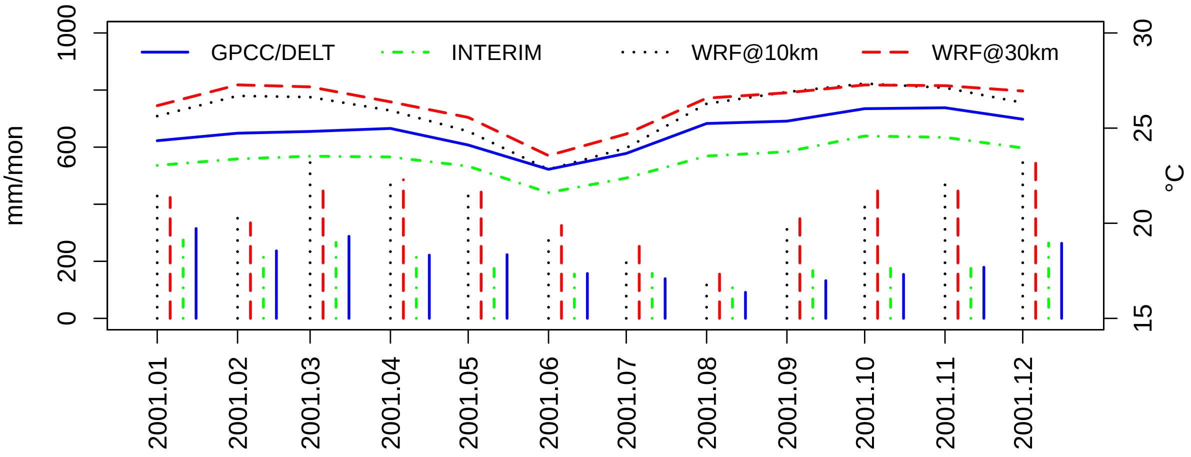

Figure 6.12.: Amazon basin: time series of monthly precipitation (horizontal bars) and 2-meter air temperature (lines).

Storage Variations The time series of water storage variations for the Amazon basin are given in figure 6.13. Two 30 km WRF runs are compared with the global reanalysis and with the 10 km simulation. GRACE observations do not exist before the year 2003. EI SST+KF+FDDA and INTERIM show a good agreement with GRACE for the period from 2003 to 2006. Therefore, these two time series are chosen as reference here.

The figure shows clearly that, apart from the first three months, both simulations yield almost identical results. With the 10 km configuration, the regional model even increases storage input for January to March. It is not clear whether this is a spin up effect that is likely to disappear for similar periods of subsequent years. Nevertheless, by increasing the horizontal model resolution no gain in performance is seen for the water storage variations.

Conclusion The analysis of the resolution effect showed hardly any improvements in terms of the spatial distribution of rainfall. For temperature the results are more promising. For precipitation the catchment averaged time series could not be crucially enhanced. Only in terms of the temperature bias, a small reduction is noticed.

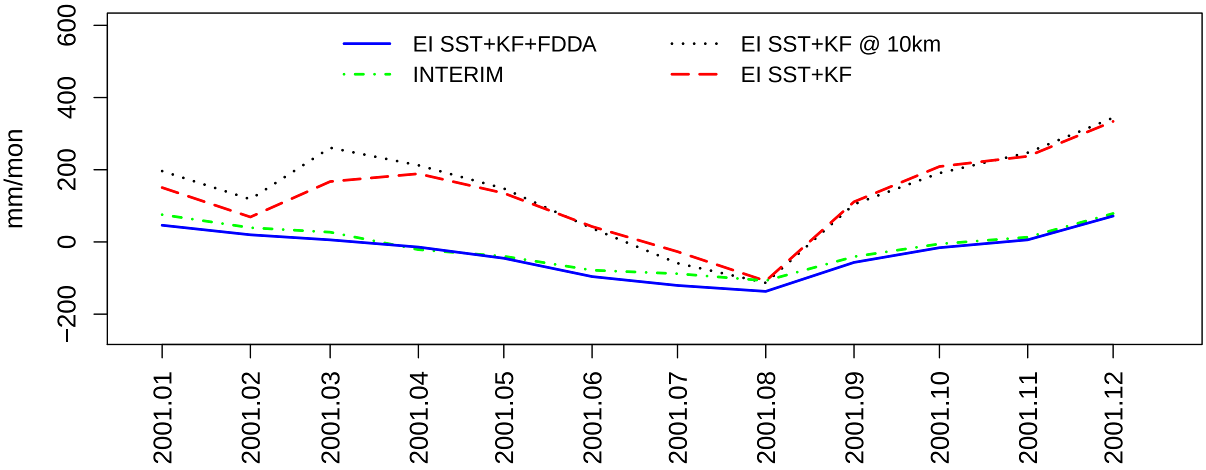

Figure 6.13.: Amazon basin: time series for monthly storage change.

It seems that it is not the physics of the cumulus schemes that are responsible for the huge precipitation bias. For none of the other study regions such strong deviations are perceived. Moreover, it is likely that some of the model's state variables like soil or air temperature are causing the cumulus physics to overproduce precipitation.

6.5. Sensitivity of the Nudging Variables

By using the gridded nudging option (FDDA) in WRF the most reasonable results are obtained for the Amazonian domain. The nudging option was tested with two different convective parametrization schemes, Kain-Fritsch (KF) and Betts-Miller-Janjic (BMJ). Gridded nudging can be applied to three of the prognostic variables of the atmospheric model, namely wind, temperature, and moisture. In the following the effect of nudging to a single variable of the global reanalysis is analyzed.

Figures 6.14 and 6.15 illustrate the impact on precipitation and 2-meter temperature, caused

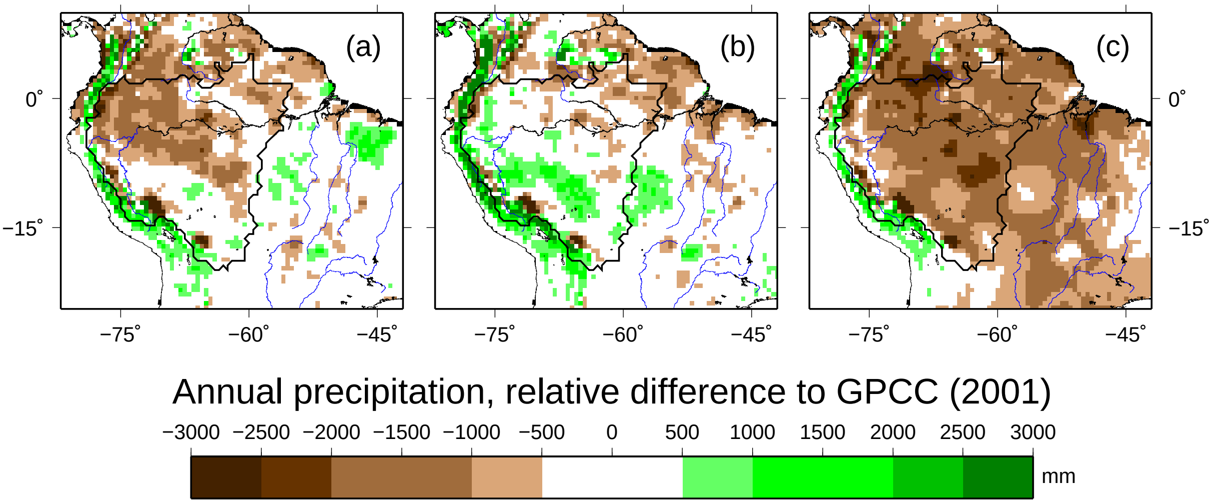

Figure 6.14.: Spatial deviation patterns in annual precipitation sum: EI SST+BMJ with nudging against, temperature (a), wind (b), and moisture (c) of the global reanalysis (ERA-INTERIM)

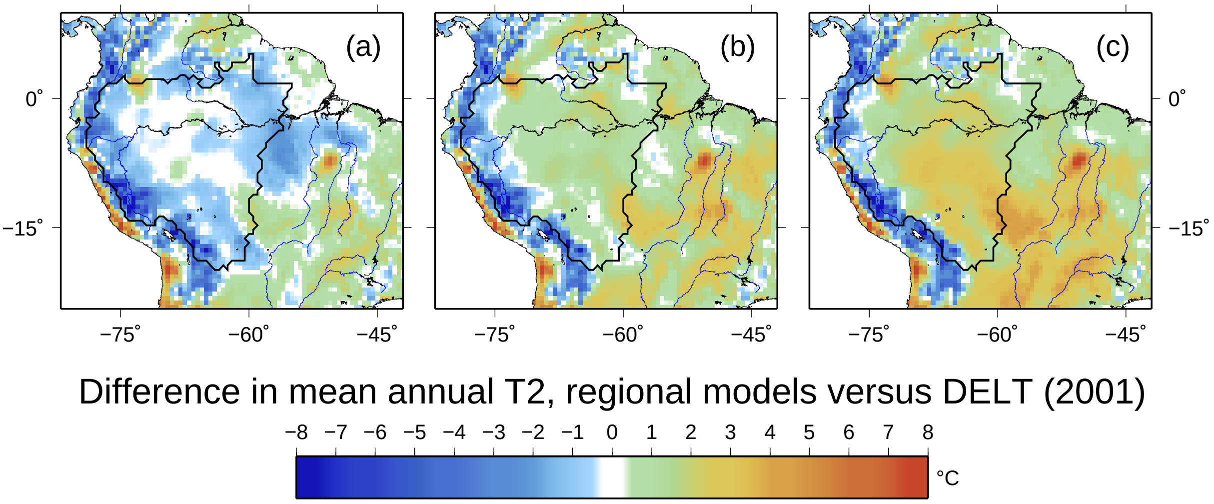

Figure 6.15.: Spatial deviation patterns in annual mean temperature: EI SST+BMJ with nudging against, temperature (a), wind (b), and moisture (c) of the global reanalysis (ERA-INTERIM)

by nudging against temperature (a), wind (b), and moisture (c). For both variables remarkable differences are obtained. Precipitation is considerably underestimated throughout the domain when moisture nudging is applied (c). If constrained to the global model's temperature, precipitation is too low in the northern part. A good agreement with GPCC is seen south of -5 °N. Wind appears to be the most effective nudging parameter with respect to precipitation for the Amazonian domain. Besides some dry spots in the northeast and too wet conditions at the Andean mountain ridge, this configuration brings the regional model closest to observed reality as far as rainfall is considered.

For the 2-meter temperature fields (fig. 6.15) the result are not as encouraging. With temperature nudging (a) large parts of the domain show a cold bias of 0.5 to 2 °C. This is not surprising as the global field (fig. 6.11 (c)) is also much colder than the observations suggest. By nudging against moisture, the results are in a similar range to the bias that is obtained if nudging is turned completely off. Wind seems to be the most important nudging parameter that affects the precipitation. In terms of 2-meter temperature the improvements are inferior. Only for the central region of the domain the positive bias is reduced but remains still in the range of 0.5 to 1.5 °C.

The results of this analysis lead to the conclusion that the water balance problem of the regional model is mainly due to horizontal transport processes. It seems that the large scale atmospheric circulation patterns are not reasonably represented within the non-nudging WRF simulation. Such features do not necessarily emerge within a regional simulation. Hence, spatial information about large scale dynamics can provide additional skill. However, by nudging against wind only, the temperature bias problem is not solved. But as the temperature field of the global reanalysis is about two degrees lower than the observations, the regional simulation could be affected to strong, like it is seen in figure 6.15 (a). Nudging constraints should always be kept as small as possible and thereby preserve the opportunity for the regional model to develop its own physical representation of a domain.

6.6. Regional Water Balance Closure

In the regional atmospheric model WRF, the prognostic variables depend largely on the lateral boundary conditions. Nevertheless, vertical exchange of energy and water at the land surface is of similar importance. E.g. the specific humidity is affected by evapotranspiration or the cumulus parametrization depends on the latent and sensible heat flux. A realistic description of land surface exchange and fraction processes requires a sophisticated physical formulation. The NOAH-LSM, used in this study, is a one dimensional (column) model. Besides the heat fluxes, it provides upward longwave and shortwave radiation. These processes are dependent on the attributes of the underlying soil and in turn, the soil exchange processes are influenced by the available moisture. Therefore, infiltration and runoff generation mechanisms must also be described within the NOAH-LSM.

Consequently, the description of water fluxes in the NOAH-LSM enables the balancing of the water outflow at the lower boundary of the regional atmospheric model. Unfortunately, no concept for horizontal transport of surface and subsurface water exists in the NOAH-LSM at horizontal resolutions above 5-10 km. This prohibits an evaluation of modeled runoff against observed discharge. In order to redress this problem, a basic runoff routing approach is implemented within this study and applied for the Amazonian river basin. Therefore, the closure of the water balance of the regional atmospheric model can be checked with respect to the discharge measurements.

Routing concept In WRF, the net falling precipitation is fractionated into soil infiltration water and infiltration excess. The latter is defined as surface runoff. The infiltrating water enters the soil, and in case of storage excess, horizontal drainage and percolation into the groundwater occurs. Both fluxes are summed up in a single variable that is defined as subsurface runoff. Runoff water leaves the regional model without the possibility of returning. Reinfiltration or rewetting of the soil is not implemented within NOAH-LSM. Thus, the sum of the two variables depicts the total runoff per cell, composed of a quick and slow response term.

The lateral translation of runoff depends on the topographical conditions of the basin and the river channel configurations. For this study it is assumed that only one single stream exists per grid cell. The cell to cell flow is realized by the kinematic wave approximation of the Saint-Venant Equations. The flow network is derived from the HYDRO1K data set of the *U.S. Geological Survey* (EROS, 2008) .

Distributed routing model For this study, it is assumed that, for the channel routing of water in the Amazon basin, inertial and pressure forces are negligible. These restrictions are necessary for the application of the kinematic wave approximation of the one dimensional Sain-Venant equations (Chow *et al.* , 1988). The combined continuity and momentum equation of the kinematic wave model is given by

$$\frac{\partial Q}{\partial x} + \alpha\beta Q^{\beta-1}\frac{\partial Q}{\partial t} = q \tag{6.1}$$

where Q, α, β, and q denote the channel flow, two channel parameters, and the diffuse channel inflow, respectively.

A linear implicit scheme is used for the numerical solution of Eq. 6.1. The finite-difference equations rely on the backward-difference method so that

$$\frac{\partial Q}{\partial x} \approx \frac{Q_{i+1}^{j+1} - Q_i^{j+1}}{\Delta x} \tag{6.2}$$

and

$$\frac{\partial Q}{\partial t} \approx \frac{Q_{i+1}^{j+1} - Q_{i+1}^{j}}{\Delta t} \tag{6.3}$$

with the distance index $_i$ and time index $_j$. The values for Q and q are derived with

$$Q \approx \frac{Q_{i+1}^{j} + Q_i^{j+1}}{2} \tag{6.4}$$

$$q \approx \frac{q_{i+1}^{j+1} + q_{i+1}^{j}}{2} \tag{6.5}$$

By substituting these equations into Eq. 6.1 and by solving for the unknown Q_{i+1}^{j+1} the numerical approximation of the kinematic wave model is

$$Q_{i+1}^{j+1} = \frac{\frac{\Delta t}{\Delta x} Q_i^{j+1} + \alpha\beta Q_{i+1}^{j}\left(\frac{Q_{i+1}^{j}+Q_i^{j+1}}{2}\right)^{\beta-1} + \Delta t\left(\frac{q_{i+1}^{j+1}+q_{i+1}^{j}}{2}\right)}{\frac{\Delta t}{\Delta x} + \alpha\beta\left(\frac{Q_{i+1}^{j}+Q_i^{j+1}}{2}\right)^{\beta-1}} \tag{6.6}$$

Derivation of flow directions The river network for the Amazonian domain is determined using the HYDRO1K data set. HYDRO1K is topographically derived from GTOPO30, containing consistent stream and drainage basin information with global coverage. The products are provided by the U.S. Geological Survey's Center for Earth Resources Observation and Science (EROS). Because of the differing horizontal resolution of HYDRO1K (30 ') and the WRF domain grid (30 km), the stream network needs an upscaling. For that purpose, the network scaling algorithm (NSA), as proposed by Fekete *et al.* (2001), is applied. With that approach, the flow directions are obtained from drainage area gradients instead of elevations gradients. This method prevents the formation of dead-ends due to equal elevation values. The flow direction is assigned from cells with lower drainage area to the adjacent cell with the highest drainage area. Eight flow directions are distinguished for every cell. The derived river network for the Amazonian domain is depicted in figure 6.16.

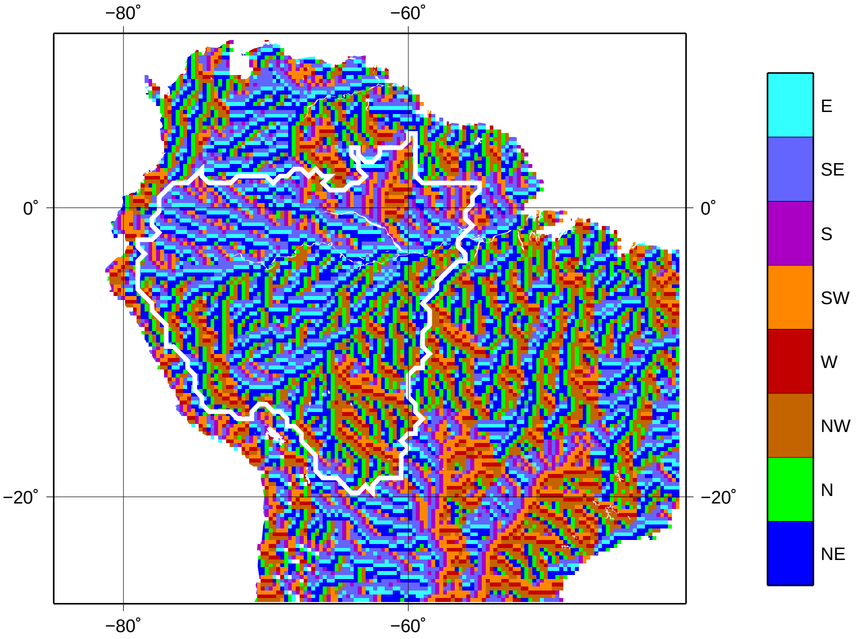

Figure 6.16.: River network for the Amazonian domain as derived from the HYDRO1K data set. The white polygon depicts the basin of the Amazon river upstream of gauge Obidos.

Parameter determination The kinematic wave model contains the two channel dependent parameters α and β. α can be determined with the following formula that is derived from Manning's equation

$$\alpha = \left(\frac{nP^{2/3}}{1.49\sqrt{S_O}} \right)^{\beta} \tag{6.7}$$

n, P, and S_0 denote the bed roughness coefficient, the wetted perimeter, and the slope, respectively. For the whole Amazon river basin, the channel parameters are crudely estimated, as a detailed determination would go beyond the scope of this study. Therefore, it is assumed that the wetted perimeter decreases steadily from river mouth towards upstream. The maximum value is set to $P = 15,000\,\mathrm{m}$, assuming 10 km width and 10 m depth at the outlet. According to the table values given by Chow *et al.* (1988), Manning's roughness coefficient is chosen as 0.1. This value is typical for slow floating natural streams. The slope values are derived from the digital elevation model. The ratio between the sub-basin area at a cell (f_a) and the total basin area ($fa_0 = 5,879,716\,\mathrm{km}^2$) is used for the diminishing of the wetted perimeter.

$$P_a = \frac{f_a}{f_0} P_0 \tag{6.8}$$

Thus, for a cell with no adjacent inflow, P decreases to a minimal value of 2.3 m. The constant β value has a strong effect on the translation of the discharge peak and needs to be calibrated with respect to the observations.

Model forcing Besides static information like e.g. the flow direction grid or the slope, the runoff routing scheme ingests time variable data of the cell runoff production. The field depicts a six hourly integral of the combined surface (SFROFF) and subsurface runoff (UDROFF), produced by WRF. At the beginning, the model is initialized with zero runoff. Hence, it is required to account for a certain spin up time.

Calibration Two basic parameters can be considered for a calibration of the runoff routing scheme. These are Manning's roughness coefficient and the translation or retention parameter β. For the period of 2002-01 to 2005-12, the best results are achieved with $n = 0.1$ and $\beta = 0.63$. However, with this setup, the hydrograph shows too quick response with an immediate raising and declining of the flow rates. An improvement is obtained if the perimeter function (eq. 6.8) is not considered as a linear function but with a logarithmic decrement of the river width.

$$P_a = \frac{\log(f_a)}{\log(f_0)} P_0 \tag{6.9}$$

Results Figure 6.17 presents the effects for applying the developed runoff routing scheme. In the upper panel, the observed hydrograph of Obidos is compared to three different time series of discharge. The dashed line depicts the basin aggregated runoff (WRF SFROFF+UDROFF), prior to routing. As can be seen, the peak in runoff generation occurs about two months before the discharge reaches its maximum at the Obidos gauge (solid line). The dashed line shows the simulated hydrograph that is produced with the kinematic wave routing approach. It takes about three to four months for the runoff of the remote areas to reach the location of the gauge. The correlation for the amplitude and seasonality of the simulated time series and the observations is strong. However, the simulated curve has a significant dry bias of about -40 mm month^{-1} for the period 2002-2006. This bias seems to be caused by underestimated precipitation in the regional simulation during the dry season from July to September. The lower panel of figure 6.17, visualizes the respective accumulated masses for observed discharge and total runoff. The center panel shows the different components of the total runoff. Apparently, the surface portion is very small.

A view on table 6.2 reveals a bias of (-255 mm year $^{-1}$) between the simulated precipitation of WRF EI SST+KF+FDDA and the observations of GPCC. Thus, the underestimated precipitation amount in the regional atmospheric model explains a significant portion of the bias that is observed for discharge. The dashed-dotted line in the upper panel of figure 6.17 shows how the coherence of the discharge observations and the routed WRF runoff increases if the constant bias for precipitation is added to the regional discharge time series (dotted line). After this additive adjustment, the obtained Nash-Sutcliffe efficiency is 0.724.

As shown in table 6.2, the precipitation bias of the regional simulation contributes 95% to the bias with GRACE but only around 50% to the bias in discharge. For the EI SST+KF+FDDA

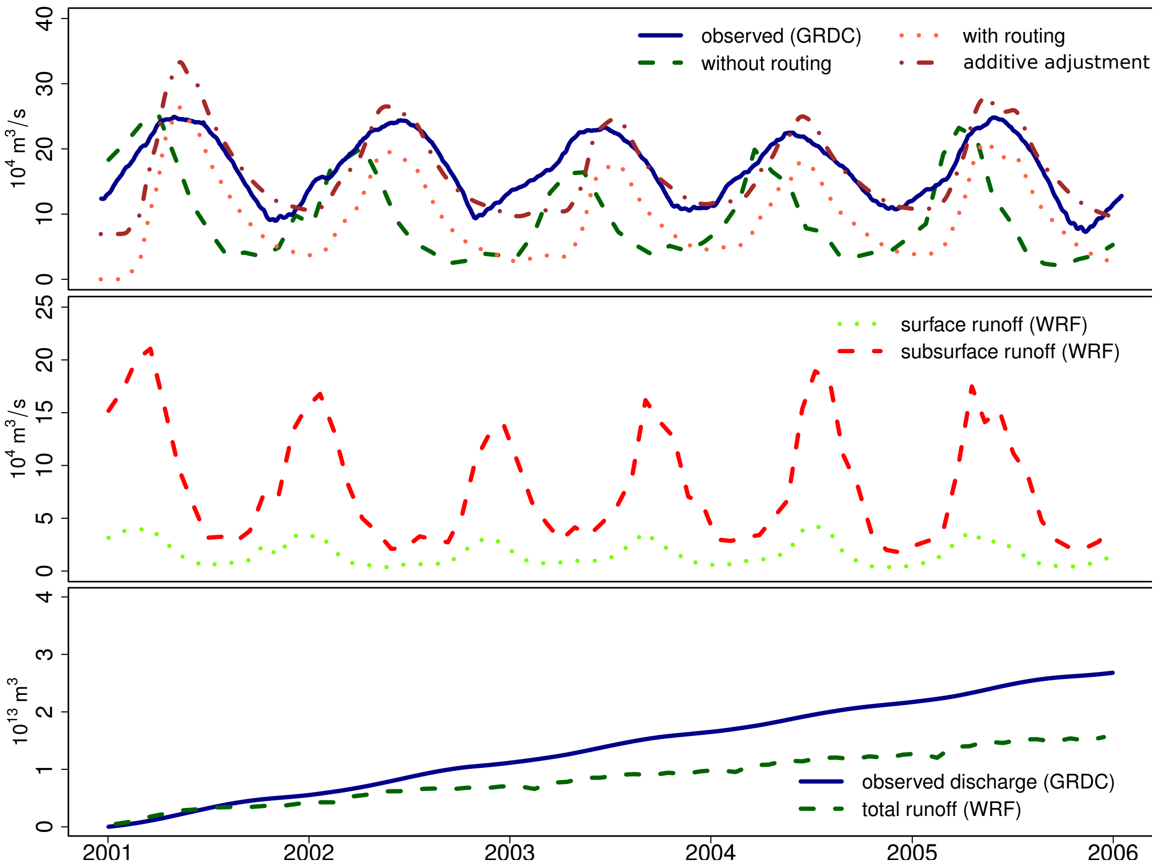

Figure 6.17.: Discharge and runoff budget for the Amazon river. Upper section: runoff from WRF before (dashed) and after (dotted) routing with the kinematic wave scheme and observed discharge from GRDC (solid). Center section: basin aggregated time series of WRF SST+EI+KF+FDDA surface and subsurface runoff, input to the routing scheme. Lower section: accumulated runoff for observations (GRDC) and WRF simulation.

run, evapotranspiration amounts 1220 mm year $^{-1}$. For a complete closure of the water balance, 230 mm year $^{-1}$ are missing besides precipitation. This equals around 19 mm month^{-1}.

Discussion The extension of the regional atmospheric model with lateral runoff routing capability introduces an additional measure for the evaluation of the water budget for a river basin. The comparison of observed and simulated discharge at the Obidos gauge shows a reasonable agreement for phase and amplitude. Moreover, the comparison shows a more or less constant underestimation for the time series of the regional model. Partly, this deviation can be explained by the observed dry bias in precipitation. With an increment of water input by

Table 6.2.: Water budget for the Amazon river basin. Comparison of observed data with regional EI SST+KF+FDDA WRF simulation. Units in mm year $^{-1}$

		P		R	dS/dt	$(-\nabla\cdot\vec{Q}-GRDC)$
Simulation	WRF	2035	WRF	668	WRF	-300
Observation	GPCC	2345	GRDC	1165	GRACE GFZ	-10
Difference		-255		-485		-270

precipitation or respectively moisture flux, the storage variations will improve with respect to GRACE. However, after a correction for the precipitation bias, the regional water budget could not be closed. The discrepancy could be partly caused by overestimated evapotranspiration or respectively moisture divergence. Additionally, the discharge observations for Obidos are not free from uncertainty.

6.7. Performance of the Regionalization

Like for the tropical regions of Northern Australia and Africa, the regional simulations tend to massively overestimate the precipitation amount of the rainy season. Thus, most of the regional model setups show a worse performance compared to their global driving reanalyses. However, with gridded nudging a significant improvement is seen for the ERA-INTERIM driven WRF run. Besides a slight dry bias, the regional model reaches at least the quality of the respective global reanalysis in terms of the annual precipitation sum. For the representation of the 2m-temperature is significantly improved and the cold bias of the global reanalysis is clearly outperformed. Although good results can be obtained with the gridded nudging setup of WRF, conceptually, this configuration is not ideal for this regional water budget study as it suppresses the development of individual patterns and physical conditions independent from the global driving data.

7

Overriding Results

The analysis of the different study regions showed that results are globally non-uniform with a large dependence on the climatic characteristic of the locations. This chapter is intended to provide also some general findings and global characteristics in the comparison of the GRACE solutions and the hydrometeorological analysis.

Variability of GRACE solutions An important finding is that the range between the different GRACE solutions strongly varies with time. Figure 7.1 depicts the absolute monthly deviations within the GRACE collective for the ten largest study regions of the global data set (the selected locations are listed in tab.B.2 in the appendix). As the accuracy of the GRACE solutions should improve with increasing area only the largest regions were selected for this comparison. It is found that the temporal variations do not follow a certain repetitive pattern. The values range

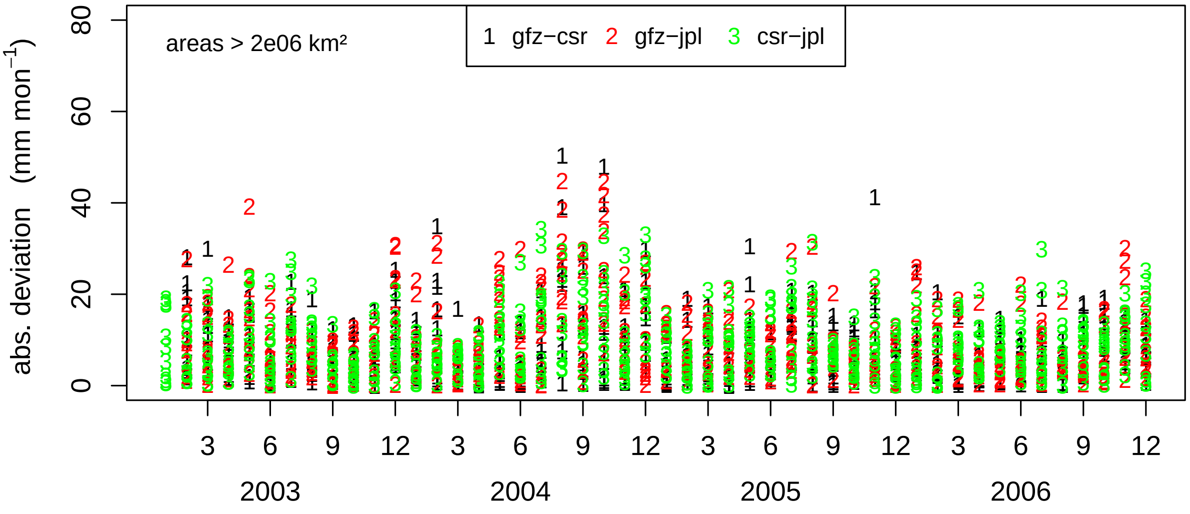

Figure 7.1.: GRACE collective of GFZ, CSR, and JPL (release 4, Swenson & Wahr (2006) destriping method, 500 km Gaussian isotropic filter). Inter product deviations for the ten largest study regions (basin area >2,000,000 km^2)

between 0 and 50 mm month^{-1} for the terrestrial water storage change. The largest deviations occur in the second half of 2004. The smallest range is found for a few months with 0 to 18 mm month^{-1}. It is also seen that the deviation amount is not correlated with the intensity of the storage change rates of a month.

GRACE versus global reanalyses For most of the considered study regions, the GRACE solution of JPL deviates from that of GFZ and CSR in terms of the standard deviation. E.g. this can be seen from the basin Taylor diagrams of the rivers Amazon (fig. 6.8) and Niger (fig. 4.16). The Box and Whisker plots of figure 7.2 give an overview about the statistical properties of the three different GRACE products with relation to the global reanalyses of INTERIM and NNRP. The comparison encompasses the monthly storage change rates for the 33 catchments that are larger than 100,000 km^2. The JPL GRACE solution differs from CSR and GFZ by a smaller interquartile range and shorter whiskers. This can be related to decreased amplitudes. Compared to the GRACE products, the reanalysis derived storage variations exhibit larger amounts of scattering. Therefore, the quality of the JPL GRACE solution can be called into question. The strongest spread and the largest outliers are observed for NNRP. In addition to that, the median deviates from zero, and a slight dry tendency is observed. For NNRP the mass balance does not seem to be properly closed. Differences are also seen for the outlier distributions. The spread is much larger for the reanalyses than for three GRACE products. Gaussian filtering (500 km, G500) of INTERIM and NNRP reduces the total spans and the statistical properties harmonize better with GRACE. Therefore, the larger variability in the atmospheric water budgets can be attributed to the elevated spatial resolution.

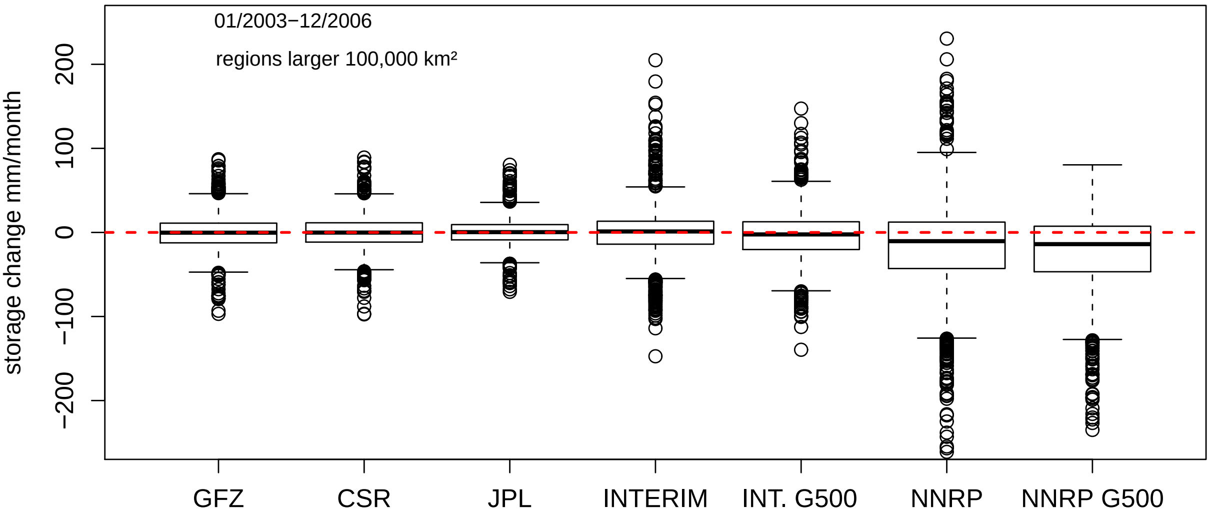

Figure 7.2.: Box and Whisker plot for terrestrial water storage change rates. GRACE collective of GFZ, CSR, and JPL (release 4, Swenson & Wahr (2006) destriping method, 500 km Gaussian isotropic filter) versus global reanalyses (INTERIM and NNRP, unfiltered and filtered).

Bias coherence in regional simulations Another central question is to check whether a possible structural coherence between the bias of regional model precipitation and GPCC and the bias of regional model storage change and GRACE, exist. For this purpose, the monthly deviations of all regions that are contained in the regional simulations are plotted in a single scatter diagram (figure 7.3). However, distinction is made for the driving data type and the physical parametrization of the regional model.The different setups consist of the two model drivings (ERA-INTERIM (EI) and NCAR/NCEP reanalysis (NR)), two different cumulus schemes (Kain-Fritsch (KF), and Betts-Miller-janjić (BMJ)), and the gridded nudging option (FDDA). According to table B.1 these are all regions with available runoff data for the period 2003-2006 and with an area of more than 1,000,000 km^2.

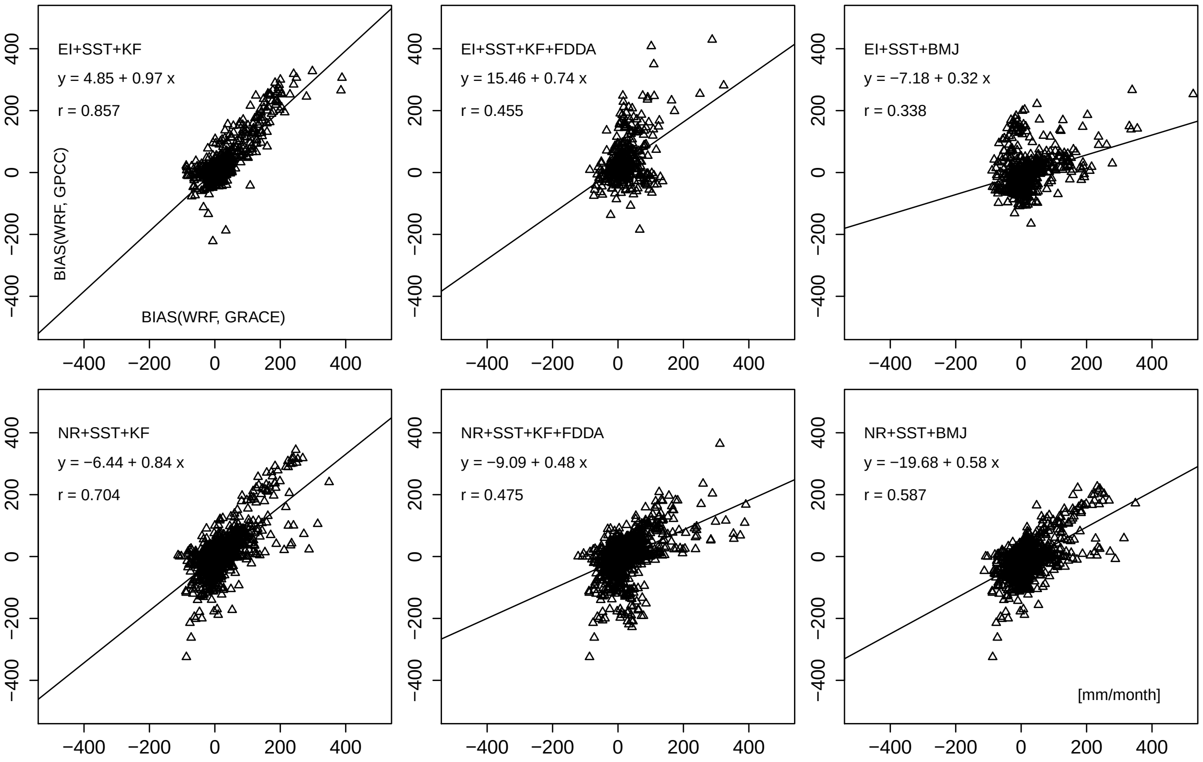

Figure 7.3.: Relation of precipitation bias and storage change bias in WRF for all basins with known discharge and area $> 10^6\,\mathrm{km}^2$. Monthly rates in mm month^{-1} for the period 2003-2006. X-axis: bias of $-\nabla \cdot \vec{Q} - R$ (WRF) vs. GRACE-GFZ; y-axis P (WRF) vs. GPCC. EI = ERA-INTERIM, NR = NCAR/NCEP reanalysis, SST = varying sea surface temperature, KF = Kain Fritsch cumulus scheme, BMJ = Betts-Miller-Janjić cumulus scheme, FDDA = gridded nudging.

The results show that, regardless of the driving data type, the comparison of the two bias measures exhibits a strong linear coherence between precipitation bias and storage change bias for the SST+KF configurations of WRF. A weaker coherence is found for the other regional simulations. EI+SST+BMJ seems to have mostly random scatter ($r = 0.338$).

The fact that the biases of the two variables P and $\frac{dS}{dt}$ show significant coherence leads to the assumption that the deviations are mainly caused by a mismatch of precipitation amounts within the regional atmospheric model. Therefore, the SST+KF configuration of WRF cannot be recommended for water budget studies.

8

Summary and Discussion

The presented results provide an overview on the water budgets of global atmospheric reanalyses and their respective dynamically downscaled fields. It is found that the performance of the regional atmospheric model is affected by different factors. The most important ones are the climatic conditions within the modeling domain, the type of global driving data, and the configuration of the regional model.

In this chapter it is discussed how the mentioned factors affect the results of the regional model and what might be the reasons for that. Moreover, the water storage variations derived from global and regional atmospheric water budgets are related to the satellite product.

8.1. Dynamic Downscaling Approach

8.1.1. Impact of Global Driving Data

Two different sets of global atmospheric reanalyses are dynamically downscaled with the regional atmospheric model WRF. The comparison and evaluation of the global fields reveals important differences between the two products of ERA-INTERIM and NCAR/NCEP NNRP. Besides the horizontal and vertical **model resolution**, remarkable deviations are obtained for the spatial patterns of modeled and observed monthly fields of 2-meter temperature and precipitation. Of course it must be remembered that the water budget of the global reanalyses is only coupled in one direction. Evapotranspiration and precipitation are calculated with a forecast model. None of the resulting water and energy fluxes are transferred back to the global assimilation model. The 2-meter temperature is computed as a diagnostic by interpolating between the skin temperature and the lowest layer of the three dimensional potential temperature fields.

For the studied domains of the regional model, it cannot be stated that one of the two used **model drivings** is superior in terms of performance. While for the Siberian domain it is found that INTERIM driving resembles the observed best, NNRP input is the best choice for the North African domain as the INTERIM driven simulations tend to overestimate precipitation and thus the storage input. Also for Australia, with NNRP a good performance is seen, but also with INTERIM reasonable results are achieved. For the Amazonian domain, only INTERIM driving in combination with spectral nudging returns a realistic water budget.

The performance of a certain regional atmospheric model driving seems to be related to the **climatological properties** of a domain. NCAR/NCEP NNRP outperforms for the dry and hot conditions of the Sahara and the Central Australian basin. ECMWF ERA-INTERIM gives more appropriate results for the polar climates. For the transition zones between desert and tropical characteristics an individual validation against observations is necessary for a ranking of the two driving scenarios. Under tropical conditions, INTERIM driving tends to overestimate convective precipitation. For the Amazon basin, this is corrected by spectral nudging.

As summary, it can be stated that the results of the regional downscaling are strongly affected by the chosen driving conditions. The validation with global gridded observations indicates that none of the boundary fields can be taken as a global optimum. An individual selection, depending on the climatic region, is necessary.

8.1.2. Impact of Regional Model Configuration

As described in section 2.3.1, the WRF modeling system contains numerous selectable modules for the different physical compartments. Some of these modules can be chosen by logical reasons like the ability to represent the physical processes with sufficient detail. For some compartments no favorable configuration can be assessed.

The parametrization of **convective motion and precipitation generation** is necessary for horizontal model resolutions smaller than (5 km)^2. The Kain-Fritsch (KF) scheme tends to overestimate convective precipitation under warm and moist conditions. Large discrepancies between simulations and observations are obtained during the rainy and monsoon periods over the Amazon and West Africa. For the Siberian domain, with KF the basin averaged time series fit well to the observations. For hot and dry regions like the Sahara, the Betts-Miller-Janjic (BMJ) scheme outperforms KF with respect to time series correlation and mean bias. Similar results are obtained for intermittent tropical conditions, e.g. for the basins of Lake Chad or Niger. For the Central Australian desert basin, the combination of KF+FDDA and INTERIM driving gives the best coherence with the observations. With NNRP the best results are obtained with the BMJ scheme.

The **sea surface temperature (SST)** is important for the calculation of open water evaporation in the regional model. Two options can be selected for the calculation of the SST. Either it is assumed that the values remain constant as initialized at model start or WRF computes and updates the field at every model time step. The results showed, that a variant SST is vital to the correct representation of the water budget in the regional model. A constant field usually results in large bias values and in a unreasonable representation of the annual cycle. Hence, with constant SST, substantiated results can only be obtained for the deserts where advection of moisture with oceanic origin is unimportant. The combination of INTERIM driving and constant SST leads to numerical problems within WRF.

Some model domains are located in zones that are largely affected by global circulation mechanisms and large scale patterns. Usually, the regional model connects to the global driving fields only through lateral boundaries. This information is not always sufficient for the development of reasonable structures in the regional domain. **Four dimensional data assimilation (FDDA)**, also known as gridded or spectral nudging provides an opportunity to constrain the regional solution for selected three dimensional variables of the global driving fields. The FDDA option strongly affects the water budget for the Amazonian domain. Remarkably, the most effective nudging variable is temperature and not wind or moisture. This suggest a strong coherence between overestimated convective precipitation with the Kain-Fritsch scheme and elevated air temperature. The combination of NNRP driving and gridded nudging returns irrational warm conditions and according to that largely overestimated amounts of rainfall. For the Siberian domain no remarkable impact on the results is found if the FDDA option is activated. Also for the North African domain no substantial difference is seen. However, especially the monsoonal conditions along the southern coast of West Africa do not improve by nudging. For Australia a slight improvement is experienced with FDDA and INTERIM driving but substantial errors remain for the northerly moisture advection during summer. Altogether, the analysis shows that the sensitivity of the FDDA option is only occasional. From the perspective of physical modeling, it is desired that the regional model resembles the conditions well without being dependent on the global model. With WRF this seem to be the case for all domains but the Amazonian. The problem with the spatial resemblance of temperature over the Amazon could also be caused by other reasons like erroneous water and energy exchange processes within the land surface and the surface exchange modules. Deduced from the results of this study, the conclusion is drawn that the use of the FDDA option in WRF should be avoided whenever possible. This will lead to a better representation of the modeled system in terms of physical pureness.

Another crucial point in regional atmospheric modeling is the selection of the **spatial model resolution**. Especially the horizontal discretization is bound to the problem of available computational capacity. The standard resolution within this study is chosen with (30 km)^2. The reprocessing of the INTERIM driven SST+KF simulation for the Amazonian domain resulted in a slight improvement of the precipitation and temperature fields. It is likely that the cumulus and planetary boundary layer parametrization schemes become more accurate with higher detail in the model. However, a better physical representation is expected with a spatial resolution that obsoletes the parametrization schemes ($<$ 5 km). Due to insufficient available computational power, this configuration could not be tested.

8.1.3. Performance of the Regional Atmospheric Model

The Weather Research and Forecasting modeling system WRF is a complex tool with many interchangeable modules and even more configuration options. The application on continental scale regions has not been the main intention of its developers. However, the chosen model resolution is not beyond the stated capabilities of WRF but the use of physical parametrization schemes is inevitable.

The validation analysis of regional simulations and global observation products leads to the conclusion that **driving and physical configuration** needs to be adapted and evaluated for every domain, individually. If this approach is followed, the model results class among the uncertainties of the observations. The seasonal cycle are usually well resembled for precipitation and temperature. However, it is experienced that the amplitudes differ for some regions or periods. Thus, it is often seen that the correlation coefficient for temperature is close to one but with a noticeable warm bias. Similar positive tendencies are also obtained for precipitation. It it assumed that the generation of rainfall in the convective schemes depends directly on the temperature gradient between surface skin and atmosphere. It is not yet clear what causes the elevated 2-meter temperature in WRF. The variable T2 is interpolated during run time between the surface skin temperature and the lowest layer of the three dimensional temperature field. No errors are found in the implementation of the algorithm. The positive bias is mainly seen during night and in winter. Especially for the Siberian domain this leads to a mean annual bias of about 5 °C. Similar findings were made by Hines *et al.* (2010). Even with a special version of the WRF model, adapted to polar regions, a significant warm bias was observed. It is concluded that the deviations are mainly a result of oceanic influence.

An infinite source of water input to the model is given by the **ocean areas**. Especially in the **tropics**, sea evaporation imports a lot of water into the regional modeling system. The amount of water that evaporates depends on the sea surface temperature (SST) and the wind. The SST is ingested from the respective global driving model with an 6 hourly interval and linearly interpolated to the time step of WRF. The coarse signal is then overlaid by short term variations that are computed within the regional model. Deviations in the global SST field affect therefore the amount of water in the regional domain. Within this study no alternative data set of SST is tested, although the results would be interesting.

8.1.4. Regional Downscaling versus Global Fields

The **quality of the global driving data** is major issue for the dynamic downscaling approaches. Without accurate boundary information for wind, moisture, and temperature the regional atmospheric model will fail to produce physically reasonable conditions. Additional information is obtained by remodeling the atmospheric processes in a spatially refined domain. New patterns of motion and exchange will emerge due to the increased detail as compared to the global driving model. Furthermore, the regional model provides the opportunity to select certain schemes for different physical compartments. If different regions are dealt with, the configurations will be individually adapted and no global optimum must be found. The application of WRF-ARW with INTERIM and NNRP driving showed that the configuration for each regional domain has to be adapted separately.

In order to assess whether regional downscaling adds value to its global driving, it is important to analyze the **spatial patterns** instead of looking at basin averaged time series only. In this study the regional fields are validated against the prevalent global observation products for 2-meter temperature and precipitation. For certain regions, the accuracy of these data sets is drastically reduced because of a lack of measuring stations. This is especially the case for the inland regions of North Africa and Australia.

With respect to the **spatial patterns of precipitation and temperature**, varying performance is seen for the selected study regions. Except for the summer period, for Australia, reasonable results are obtained with the regional model. The same applies for the Amazonian domain if gridded nudging is used. With this configuration, WRF outperforms the global reanalysis of ECMWF ERA-INTERIM in terms of the temperature bias. However the resulting precipitation fields show a slight dry tendency. The downscaled results remain within the uncertainty bounds spanned by the observations. For the North African domain, the NNRP driven regional simulation with variable SST and BMJ cumulus scheme adds also value to the driving data. Except for the southern coastal region of Western Africa, the downscaled fields correct the bias tendencies of the global fields. Like for Australia, the temperature is about 1 to 2 °C warmer than found in the observations. But it must be taken into account that the global fields of INTERIM and NNRP are 1 to 2 °C too cold. For Siberia the global reanalyses suggest wetter conditions than observed in reality. The regional simulations are able to correct the bias but produce dryer conditions than seen with GPCC. However, the resulting patterns are in agreement with CRUP and DELP and hence within the uncertainty bounds of the observations. While the global reanalyses contain a warm and cold bias for the eastern and western domain, respectively, a large warm bias is seen for the regional simulation. Thus it must be stated that the regional model contains structural problems for the 2-meter temperature during polar winter. Thus, no additional skill could be added to the global fields.

The study shows that the performance of the regional atmosphere model is different, depending on the region of application and the driving data used. The **identification of suitable model**

configurations requires a proper evaluation with physical concepts and a validation with observations. If reasonable results are obtained, compared to the global input, the outcome provides a convenient measure of uncertainty for the atmospheric approach of assessing the terrestrial water storage variations.

8.2. Evaluation with GRACE

GRACE versus Hydrometeorological Uncertainty

With the Gravity Recovery and Climate Experiment GRACE, global observations of terrestrial water storage change became available for the first time in scientific history. But, as expressed in the methods section, several problems exist with the extraction of the hydrological signal from the continuous gravity field measurements. For a consistent evaluation, the three prevalent GRACE products from GFZ Potsdam, CSR Texas, and JPL Pasadena were selected as a collective representation. The three products are taken as a measure of uncertainty of the data processing of GRACE. It was shown that the extent of the uncertainty bounds have no structural dependencies. Moreover, the JPL solution could be identified to be unrealistic in terms of representing the terrestrial water storage change signal.

For the studied regions, the **comparison between the atmospheric water budgets and GRACE** solution gives a distinct picture. Despite biases and differences in the peak-to-peak amplitudes, the correlation for the wave periods is found to be rather strong. While the collective of GRACE solutions for water storage variations shows similar bounds of uncertainty for all studied basins, differences are seen for the atmospheric water budget approach. The tightest atmospheric constraints are observed for the Siberian basin (Lena & Yenisei). Apart from a few outliers in the NNRP reanalysis strong reliability is observed. The peak depletion rates, that are likely related to erroneous runoff data because of ice congestion events, are not seen in the GRACE solutions. For the arid Saharan and Central Australian basin, the uncertainty bounds of GRACE and the atmospheric water budgets exhibit a similar range. Tighter atmospheric constraints are obtained for the Lake Chad and the Niger basin, if INTERIM is taken as global reanalysis and NNRP is used to drive the regional model. However, the curves for GRACE and atmospheric water budget do not always overlay. Yet no explanation was found for these repetitive occurrences of mismatches. Similar results are obtained for the Amazon river basin.

Altogether, **the atmospheric water budget approach provides valuable constraints** for an evaluation with the GRACE solutions. However, for regions with low terrestrial water storage variations, typically 20 mm month^{-1} and below, both methods share a similar range of uncertainty. Still, also for regions where tight atmospheric constraints are observed, structural deviations are found between the atmospheric water budget approach and the GRACE observations.

Interesting results are obtained with respect to **isotropic filtering** of the $\nabla \cdot \vec{Q}$ fields. The application of a 500 km Gaussian filter leads to distinct effects for the different study regions. A gain in coherence with GRACE storage variations is seen for the river basins of Amazon and Niger. Almost no changes are found for the time series of the Siberian domain (Lena & Yenisei) and the Lake Chad basin. For the Central Australian basin, spatial smoothing affects mainly the global reanalyses. The downscaled fields are not very sensitive to filtering. A relatively large impact is seen for the Saharan basin where the Gaussian smoothing introduces a bias, that increases the gap between the atmospheric approach and GRACE. Altogether, it seems that the impact of spatial filtering depends the shape and surrounding of a certain basin. For small basins and regions with small water storage variations leakage effects will play an important role. For large basins with strong and spatially heterogeneous water storage dynamics, the predominant effect is signal loss by smoothing.

8.3. Closure of the Water Balance

The validation of hydrometeorological modeling systems suffers often from the sparse availability of proper observation data. For WRF, precipitation and temperature are predominantly used for that purpose. Discharge observations provide an additional source of information that could be used to check the water budget at the lower boundary of the model. However, converting the model runoff into station discharge requires a concept that accounts for the lateral transport of water through the catchment.

Therefore a basic **runoff routing scheme** was developed and tested with the regional runoff produced by the WRF model. Besides a dry bias that is caused by rainfall underestimation in the regional model, a good agreement is observed for the simulation and the measured discharge at the gauge of Obidos. For the specific months, where a significant discrepancy exists for the simulations and observations of precipitation and discharge, GRACE deviates in a similar way from the computed water storage budget of WRF. Thus, for these specific months, GRACE can be defined to be more reliable than the results of the regional hydrometeorological simulation. For all other months, the regional model shows a good agreement in terms of precipitation, discharge, and also storage variation.

As a conclusion, it can be stated the inclusion of lower boundary water transport concepts provides valuable additional information that helps to uncover the gaps in the water balance closure. Therefore it is particularly recommended to extend this approach to other study regions of the regional hydrometeorological approach.

9

Final Conclusion and Outlook

9.1. Regional Hydrometeorological Approach

Dynamic downscaling offers a sophisticated method for the refining and improvement of global atmospheric fields. With respect to the NCAR/NCEP reanalysis, substantial improvement was seen in terms of the precipitation bias and also for the coherence with the GRACE solutions. With respect to global atmospheric fields, ECMWF ERA-INTERIM clearly outperformed NNRP for the validation with independent observations of temperature and precipitation. Concerning the driving of WRF, NNRP performs best for dry and arid conditions while INTERIM is more suitable for the tropical regions. Except for the Amazonian domain, the Betts-Miller-Janjić cumulus parametrization led to the best results.

The experienced temperature bias problem of the regional atmospheric model WRF could not be solved, yet. It is assumed that the representation of surface and subsurface water and energy fluxes is not correctly conceptualized. E.g. the shallow soil depth of the land surface model could lead to insufficient heat or water storage capacity. Therefore, the outcome of this study suggests the need for an improvement of the soil vegetation atmosphere transfer processes (SVAT) of the regional atmospheric model WRF. Except for the mentioned shortcomings with the dynamic downscaling, the atmospheric water budget approach provided valuable constraints and uncertainty bounds for the evaluation with the *Gravity Recovery and Climate Experiment* GRACE.

9.2. Applicability of GRACE in Hydrology

A comprehensive evaluation of GRACE water storage variations with atmospheric water budgets was carried out within this study. For the first time in hydrological science, direct observations of the terrestrial freshwater storage variations could be derived. However, the methodology for the derivation of the hydrological GRACE product is complicated and introduces many sources of uncertainty. For example, this becomes obvious if alternative products from different data centers are considered.

If the satellites remain in healthy condition, it is likely that the mission reaches a 10 year lifetime. This span should be sufficiently long for deriving long term means of monthly water storage variations. Of course this implies that the models used for de-aliasing are free of trends or biases.

The comparison with the atmospheric water budgets revealed systematic deviations of different extent, depending on the geographic region and the considered time period of the seasonal cycle. Therefore, the integrity of the GRACE solutions for storage mass variation could be challenged. This is especially the case for the sink basins where $\nabla \cdot \vec{Q}$ is directly related to the variation in water storage but without the problem of uncertainties in the discharge measurements. The presented results suggest, that neither the atmospheric nor the satellite approach are reliable for regions with minimal storage change rates like e.g. the Sahara. Spatial filtering removes a significant portion of the signal. Therefore, the change rates of the unfiltered atmospheric fields should be closer to reality than the de-aliased GRACE solutions.

On the whole, GRACE data should be used carefully for hydrological water budget studies. It is recommended to always have additional independent data sources for evaluation and validation. Because of the momentary uncertainties, observed from the collective of different GRACE products and the deviations with respect to the atmospheric water budgets, it is advised not to use GRACE for the calibration of water balance models, neither for regional nor for global approaches.

9.3. Further Research Demand

Recently, some new global reanalysis products are becoming available. The *Modern Era Retrospective Analysis* (MERRA) of the NASA and the *Climate Forecast System Reanalysis* (CFSR) from NCEP are intended to become new landmarks in terms of spatial and temporal model resolution. Together with ERA-INTERIM, the inclusion of these new products in the evaluation approach will provide additional sophistication for constraining the atmospheric water budget uncertainties.

As an extension of the here presented water budget analysis, it would be very interesting to evaluate patterns of soil moisture and sea surface salinity derived $P-E$ data from the *Soil Moisture and Salinity Mission* SMOS of the ESA (Berger *et al.* , 2002). This is of major interest as this is the first time that these components are observed with this spatial extent.

In order to avoid the issue of convective parametrization in the regional atmospheric model WRF, it would be of interest to prepare a simulation with around 5 km horizontal resolution with deactivated cumulus schemes. Such a high resolution simulation could be performed using the *Noah Distributed Hydrological Modeling System* (NDHMS) of Gochis & Chen (2003). With this hydrologically extended version of the WRF model, a much more complete analysis of the regional water budget becomes possible. However, as this approach is computationally very demanding, it will not be possible to cover a longer time period with this method.

Hence, substantial work should be invested into the improvement of the representation of horizontal surface and subsurface water fluxes in the regional atmospheric model WRF with the aim of meso-scale applicability. With respect to the complete closure of the water balance, also processes like lateral water transport, and groundwater contribution must be implemented. Such an extension of the WRF model is envisaged by a coupling to the mesoscale *hydrological modeling system* of Yu *et al.* (2006).

Regarding the improvement of the GRACE products, further development is already ongoing. This implies the usage of state of the art models for atmospheric and ocean de-aliasing. Additional benefit is expected by the improvement of the de-correlation and spatial filtering methods. In future, space borne observation of terrestrial water storage variations should be continuously available. Therefore, a follow up mission for GRACE is very desirable. However, such a mission should provide a remarkable gain in temporal and spatial resolution e.g. by increasing the number of satellites.

Bibliography

ADLER, ROBERT F., HUFFMAN, GEORGE J., CHANG, ALFRED, FERRARO, RALPH, XIE, PING-PING, JANOWIAK, JOHN, RUDOLF, BRUNO, SCHNEIDER, UDO, CURTIS, SCOTT, BOLVIN, DAVID, GRUBER, ARNOLD, SUSSKIND, JOEL, ARKIN, PHILIP, & NELKIN, ERIC. 2003. The Version-2 Global Precipitation Climatology Project (GPCP) Monthly Precipitation Analysis (1979–Present). *Journal of Hydrometeorology*, **4**(6), 1147–1167, doi:10.1175%2F1525-7541%282003%29004%3C1147%3ATVGPCP%3E2.0.CO%3B2.

AWANGE, J. L., SHARIFI, M. A., BAUR, O., KELLER, W., FEATHERSTONE, W. E., & KUHN, M. 2009. GRACE hydrological monitoring of Australia: Current limitations and future prospects. *Journal of Spatial Science*, **54**(1), 23–36, doi:10.1080/14498596.2009.9635164.

BARRY, R. G. 1968. Vapour flux divergence and moisture budget calculations for Labrador-Ungava. *Cahiers de géographie du Québec*, **12**(25), 91–102.

BERBERY, ERNESTO H., RASMUSSON, EUGENE M., & MITCHELL, KENNETH E. 1996. Studies of North American continental-scale hydrology using Eta model forecast products. *J. Geophys. Res.*, **101**, 7305–7319.

BEREZOVSKAYA, SVETLANA, YANG, DAQING, & KANE, DOUGLAS L. 2004. Compatibility analysis of precipitation and runoff trends over the large Siberian watersheds. *Geophys. Res. Lett.*, **31**(Nov.), doi:10.1029/2004GL021277.

BERGER, M., CAMPS, A., FONT, J., KERR, Y., MILLER, J., JOHANNESSEN, J., BOUTIN, J., DRINKWATER, M.R., SKOU, N., FLURY, N., RAST, M., REBHAN, H., & ATTEMA, E. 2002 (Aug.). *Measuring Ocean Salinity with ESA's SMOS Mission - Advancing the Science*. Bulletin 111. European Space Agency (ESA).

BETTADPUR, SRINIVAS. 2007. *UTCSR Level-2 Processing Standards Document for Product Release 04*. Technical information. Center for Space Research, The University of Texas at Austin. `http://isdc.gfz-potsdam.de/`, visited 2010/01/27.

BORGE, RAFAEL, ALEXANDROV, VASSIL, JOSÉ DEL VAS, JUAN, LUMBRERAS, JULIO, & RODRÍGUEZ, ENCARNACION. 2008. A comprehensive sensitivity analysis of the WRF model for air quality applications over the Iberian Peninsula. *Atmospheric Environment*, **42**(37), 8560–8574, doi:10.1016/j.atmosenv.2008.08.032.

BROHAN, P., KENNEDY, J. J., HARRIS, I., TETT, S. F. B., & JONES, P. D. 2006. Uncertainty estimates in regional and global observed temperature changes: A new data set from 1850. *J. Geophys. Res.*, **111**(June), D12106, doi:10.1029/2005JD006548.

BRUINSMA, SEAN, LEMOINE, JEAN-MICHEL, BIANCALE, RICHARD, & VALÈS, NICOLE. 2010. CNES/GRGS 10-day gravity field models (release 2) and their evaluation. *Advances in Space Research*, **45**(4), 587–601, doi:10.1016/j.asr.2009.10.012.

CASTRO, C. L., SR., R. A. PIELKE, & LEONCINI, G. 2005. Dynamical downscaling: Assessment of value retained and added using the Regional Atmospheric Modeling System (RAMS). *J. Geophys. Res*, **110**, doi:10.1029/2004JD004721.

CHEN, FEI, & DUDHIA, JIMY. 2001. Coupling an Advanced Land Surface-Hydrology Model with the Penn State–NCAR MM5 Modeling System. Part I: Model Implementation and Sensitivity. *Month. Weather Rev.*, **129**(4), 569–585, doi:10.1175/1520-0493(2001)129¡0569:CAALSH¿2.0.CO;2.

CHEN, J. L., WILSON, C. R., FAMIGLIETTI, J. S., & RODELL, MATT. 2007. Attenuation effect on seasonal basin-scale water storage changes from GRACE time-variable gravity. *J. Geod.*, **81**(4), 237–245, doi:10.1007/s00190-006-0104-2.

CHOU, M.-D., & SUAREZ, MAX J. 1994. *Technical report series on global modeling and data assimilation*. NASA Tech. Memo., no. 104606. National Aeronautics and Space Administration, Goddard Space Flight Center. 85pp. Chap. An efficient thermal infrared radiation parameterization for use in general circulation models.

CHOW, VEN TE, MAIDMENT, DAVID. R., & MAYS, LARRY W. 1988. *Applied Hydrology*. McGraw-Hill series in water resources and environmental engineering. McGraw-Hill. 572pp. ISBN 0-07-010810-2.

COSTA, MARCOS, & FOLEY, JONATHAN A. 1999. Trends in the hydrologic cycle of the Amazon basin. *Journal of Geophysical Research*, **104**, 14,189–14,198.

COTTON, W. R., PIELKE SR., R. A., WALKO, R. L., LISTON, G. E., TREMBACK, C. J., JIANG, H., MCANELLY, R. L., HARRINGTON, J. Y., NICHOLLS, M. E., CARRIO, G. G., & MCFADDEN, J. P. 2003. RAMS 2001: Current status and future directions. *Meteorology and Atmospheric Physics*, **82**(1), 5–29, doi:10.1007/s00703-001-0584-9.

CULLATHER, R. I., BROMWICH, D. H., & SERREZE, M. C. 2000. The Atmospheric Hydrologic Cycle over the Arctic Basin from Reanalyses. Part 1: Comparison with Observations and Previous Studies. *Journal of Climate*, **13**, 923–937.

DROSDOWSKY, WASYL. 1993. An analysis of Australian seasonal rainfall anomalies: 1950-1987. II: Temporal variability and teleconnection patterns. *International Journal of Climatology*, **13**(2), 111–149, doi:10.1002/joc.3370130202.

DUAN, X., GUO, J., SHUM, C., & VAN DER WAL, W. 2009. On the postprocessing removal of correlated errors in GRACE temporal gravity field solutions. *Journal of Geodesy*, **83**(11), 1095–1106, doi:10.1007/s00190-009-0327-0.

EROS, USGS. 2008. *HYDRO1k Elevation Derivative Database*. Tech. rept. U.S. Geological Survey Center for Earth Resources Observation and Science (EROS). http://eros.usgs.gov/products/elevation/hydro1k.html.

FAMIGLIETTI, J. S., & YEH, J.-F. 2008. Regional terrestrial water storage change and evapotranspiration from terrestrial and atmospheric water balance computations. *J. Geophys. Res.*, D09180, doi:10.1029/2007JD009045.

FEKETE, BALÁZS M., VÖRÖSMARTY, CHARLES J., & GRABS, WOLFGANG. 2000. *Global Composite Runoff Fields Based on Observed River Discharge and Simulated Water Balances*. Tech. rept. UNH/GRDC.

FEKETE, BALÁZS M., VÖRÖSMARTY, CHARLES J., & LAMMERS, RICHARD B. 2001. Scaling Gridded River Networks for Macroscale Hydrology: Development, Analysis, and Control of Error. *Water Resour. Res.*, **37**, 1955–1967, doi:10.1029/2001WR900024.

FLECHTNER, FRANK. 2007. *GFZ Level-2 Processing Standards Document for Product Release 04*. Technical information. GeoForschungszentrum Potsdam. `http://isdc.gfz-potsdam.de/`, visited 2010/01/21.

FUKUTOMI, YOSHIKI, IGARASHI, HIROMICHI, MASUDA, KOOITI, & YASUNARI, TETSUZO. 2003. Interannual Variability of Summer Water Balance Components in Three Major River Basins of Northern Eurasia. *Journal of Hydrometeorology*, **4**(2), 283–296, doi:10.1175/1525-7541(2003)4<283:IVOSWB>2.0.CO;2.

GOCHIS, D. J., & CHEN, F. 2003. *Hydrological enhancements to the community Noah land surface model.* NCAR Technical Note NCAR/TN-454+STR. NCAR.

GONG, D.-Y., & HO, C.-H. 2002. The Siberian High and climate change over middle to high latitude Asia. *Theoretical and Applied Climatology*, **72**(1), 1–9, doi:10.1007/s007040200008.

GRELL, GEORG A., & DÉVÉNYI, DEZSŐ. 2002. A generalized approach to parameterizing convection combining ensemble and data assimilation techniques. *Geophys. Res. Lett.*, **29**(July), 38–1–38–4, doi:10.1029/2002GL015311.

GRELL, GEORG A., DUDHIA, JIMY, & STAUFFER, DAVID R. 1995 (June). *A Description of the Fith-Generation Penn State/NCAR Mesoscale Model (MM5).* NCAR Technical Note NCAR/TN-398 + STR.

HAGEMANN, STEFAN, ARPE, KLAUS, & BENGTSSON, LENNART. 2005. *Validation of the hydrological cycle of ERA-40.* ERA-40 Project Report Series 24. European Centre for Medium Range Weather Forecasts, Shinfield Park, Reading, RG2 9AX, England.

HINES, KEITH M., BROMWICH, DAVID H., BAI, LE-SHENG, BARLAGE, MICHAEL, & SLATER, ANDREW G. 2010. Development and Testing of Polar WRF. Part III. Arctic Land*. *Journal of Climate*, doi:10.1175/2010JCLI3460.1.

HIRSCHI, MARTIN, VITERBO, PEDRO, & SENEVIRATNE, SONIA I. 2006. Basin-scale water-balance estimates of terrestrial water storage variations from ECMWF operational forecast analysis. *Geophys. Res. Lett.*, **33**(21), L21401, doi:10.1029/2006GL027659.

HIRSCHI, MARTIN, SENEVIRATNE, SONIA I., HAGEMANN, STEFAN, & SCHÄR, CHRISTOPH. 2007. Analysis of seasonal terrestrial water storage variations in regional climate simulations over Europe. *J. Geophys. Res.*, **112**, doi:10.1029/2006JD008338.

HONG, SONG-YOU, DUDHIA, JIMY, & CHEN, SHU-HUA. 2004. A Revised Approach to Ice Microphysical Processes for the Bulk Parameterization of Clouds and Precipitation. *Month. Weather Rev.*, **132**, 103–120, doi:10.1175/1520-0493(2004)132¡0103:ARATIM¿2.0.CO;2.

HONG, SONG-YOU, NOH, YIGN, & DUDHIA, JIMY. 2006. A New Vertical Diffusion Package with an Explicit Treatment of Entrainment Processes. *Monthly Weather Review*, **134**(9), 2318–2341, doi:10.1175%2FMWR3199.1.

HÄCKEL, HANS. 1999. *Meteorologie*. 4th edn. Stuttgart: Ulmer. 448pp. ISBN 3-8252-1338-2.

ILK, K.-H., FLURY, J., RUMMEL, R., SCHWINTZER, P., BOSCH, W., HAAS, C., SCHRÖTER, J., STAMMER, D., ZAHEL, W., MILLER, H., DIETRICH, R., HUYBRECHTS, P., SCHMELING, H., WOLF, D., GÖTZE, H.J., RIEGGER, J., BÁRDOSSY, A., GÜNTNER, A., & GRUBER, TH. 2005. *Mass transport and mass distribution in the Earth system - Contribution of the new generation of satellite gravity and altimetry missions to geosciences.*

JACOBSON, MARK Z. 1999. *Fundamentals of atmospheric modeling*. Cambridge Univ. Press. 656pp. ISBN 0-521-63143-2 ; 0-521-63717-1.

JANJIĆ, ZAVIŠA I. 2000. Comments on ”Development and Evaluation of a Convection Scheme for Use in Climate Models”. *Journal of the Atmospheric Sciences*, **57**(21), 3686–3686, doi:10.1175%2F1520-0469%282000%29057%3C3686%3ACODAEO%3E2.0.CO%3B2.

KAIN, JOHN S. 2004. The Kain-Fritsch Convective Parameterization: An Update. *J. Appl. Meteorol.*, **43**, 170–181, doi:10.1175/1520-0450(2004)043<0170:TKCPAU>2.0.CO;2.

KALNAY, E., KANAMITSU, M., KISTLER, R., COLLINS, W., DEAVEN, D., GANDIN, L., IREDELL, M., SAHA, S., WHITE, G., WOOLLEN, J., ZHU, Y., LEETMAA, A., REYNOLDS, R., CHELLIAH, M., EBISUZAKI, W., HIGGINS, W., JANOWIAK, J., MO, K.C., ROPELEWSKI, C., WANG, J., JENNE, ROY, & JOSEPH, DENNIS. 1996. The NCEP/NCAR 40-Year Reanalysis Project. *Bulletin of the American Meteorological Society*, **77**(3), 437–471, doi:10.1175%2F1520-0477%281996%29077%3C0437%3ATNYRP%3E2.0.CO%3B2.

KANAMITSU, MASAO, EBISUZAKI, WESLEY, WOOLLEN, JACK, YANG, SHI-KENG, HNILO, J. J., FIORINO, M., & POTTER, G. L. 2002. NCEP–DOE AMIP-II Reanalysis (R-2). *Bulletin of the American Meteorological Society*, **83**(11), 1631–1643, doi:10.1175%2FBAMS-83-11-1631.

KIM, JEONGRAE, & TAPLEY, BYRON D. 2002. Error analysis of a low-low satellite-to-satellite tracking mission. *Journal of Guidance, Control, and Dynamics*, **25**(6), 1100–1107.

KLEES, R., ZAPREEVA, E. A., WINSEMIUS, H. C., & SAVENIJE, H. H. G. 2007. The bias in GRACE estimates of continental water storage variations. *Hydrol. Earth Syst. Sci.*, **11**, 1227–124.

KOTTEK, MARKUS, GRIESER, JÜRGEN, BECK, CHRISTOPH, RUDOLF, BRUNO, & RUBEL, FRANZ. 2006. World Map of the Köppen-Geiger climate classification updated. *Meteorologische Zeitschrift*, **15**, 259–263, doi:10.1127/0941-2948/2006/0130.

LABRAGA, J. C., FRUMENTO, O., & LOPEZ, M. 2000. The Atmospheric Water Vapor Cycle in South America and the Tropospheric Circulation. *Journal of Climate*, **13**, 1899–1915.

LENTERS, J.D., & COOK, K.H. 1995. Simulation and Diagnosis of the Regional Summertime Precipitation Climatology of South America. *Journal of Climate*, **8**(12), 2988–3005, doi:10.1175%2F1520-0442%281995%29008%3C2988%3ASADOTR%3E2.0.CO%3B2.

LIU, JIUXING, WU, JIESHENG, & PANDA, DHABALESWAR. 2004. High Performance RDMA-Based MPI Implementation over InfiniBand. *International Journal of Parallel Programming*, **32**(3), 167–198, doi:10.1023/B:IJPP.0000029272.69895.c1.

MASOUD SAJADI, S. 2007 (August). *Weather Research and Forecasting Model 2.2. Documentation: A Step-by-step guide of a Model Run*. Technical Report FIU-SCIS-2007-09-02. School of Computing and Unformation Sciences (SCIS), Florida International University (FIU), 11200 SW 8th St., Miami, Florida 33199, USA.

MATSUURA, KENJI, & WILLMOT, CORT J. 2009a (June). *Terrestrial Air Temperature: 1900-2008 Gridded Monthly Time Series (Version 2.01)*. `http://climate.geog.udel.edu/~climate/`, visited 2010/01/13.

MATSUURA, KENJI, & WILLMOT, CORT J. 2009b (June). *Terrestrial Precipitation: 1900-2008 Gridded Monthly Time Series (Version 2.01)*. `http://climate.geog.udel.edu/~climate/`, visited 2010/01/13.

MLAWER, ELI J., TAUBMAN, STEVEN J., BROWN, PATRICK D., IACONO, MICHAEL J., & CLOUGH, SHEPARD A. 1997. Radiative transfer for inhomogeneous atmospheres: RRTM, a validated correlated-k model for the longwave. *J. Geophys. Res.*, **102**, 16,663–16,682, doi:10.1029/97JD00237.

MOLION, LUIZ CARLOS BALDICERO. 1987. Climatologia dinãmica da região Amazõnica: mecanismos de precipitação. *Revisita Brasileira de Meteorologia*, **2**, 107–117.

NICHOLSON, SHARON E., & GRIST, JEREMY P. 2003. The Seasonal Evolution of the Atmospheric Circulation over West Africa and Equatorial Africa. *Journal of Climate*, **16**(7), 1013–1030, doi:10.1175%2F1520-0442%282003%29016%3C1013%3ATSEOTA%3E2.0.CO%3B2.

NUMAGUTI, ATUSI. 1999. Origin and recycling processes of precipitating water over the Eurasian continent: Experiments using an atmospheric general circulation model. *J. Geophys. Res.*, **104**, 1957–1972, doi:10.1029/1998JD200026.

OKI, TAIKAN, & KANAE, SHINJIRO. 2006. Global Hydrological Cycles and World Water Resources. *Science*, **313**(5790), 1068–1072, doi:10.1126/science.1128845.

PALMÉN, E., & HOLOPAINEN, O. 1962. Divergence, Vertical Velocity and Conversion between Potential and Kinetic Energy in an Extratropical Disturbance. *Geophysica*, **8**(2), 89–113.

PALMÉN, E., & SÖDERMANN, D. 1966. Computation of the Evaporation from the Baltic Sea from the Flux of Water Vapor in the Atmosphere. *Geophysica*, **8**(4), 261–279.

PEIXOTO, JOSE P., & OORT, ABRAHAM H. 1992. *Physics of climate*. American Institute of Physics, New York. Chap. 12.2.2 Balance equations for water, pages 274–277.

PETERSON, THOMAS C., & VOSE, RUSSELL S. 1997. An Overview of the Global Historical Climatology Network Temperature Database. *Bulletin of the American Meteorological Society*, **78**(12), 2837–2849, doi:10.1175%2F1520-0477%281997%29078%3C2837

ROADS, J., KANAMITSU, M., & STEWART, R. 2002. CSE Water and Energy Budgets in the NCEP-DOE Renalysis II. *Journal of Hydrometerology*, **3**(3), 227–248.

RODELL, M., FAMIGLIETTI, J. S., CHEN, J., SENEVIRATNE, S. I., VITERBO, P., HOLL, S., & WILSON, C. R. 2004. Basin scale estimates of evapotranspiration using GRACE and other observations. *Geophys. Res. Lett.*, **31**(Oct.), L20504, doi:10.1029/2004GL020873.

SAHSAMANOGLOU, H. S., MAKROGIANNIS, T. J., & KALLIMOPOULOS, P. P. 1991. Some aspects of the basic characteristics of the Siberian anticyclone. *International Journal of Climatology*, **11**(8), 827–839, doi:10.1002/joc.3370110803.

SCHNEIDER, U., FUCHS, T., MEYER-CHRISTOFFER, A., & RUDOLF, B. 2008. *Global Precipitation Analysis Products*. `http://gpcc.dwd.de`, visited 2010/01/13.

SEITZ, F., SCHMIDT, M., & SHUM, C. K. 2008. Signals of extreme weather conditions in Central Europe in GRACE 4-D hydrological mass variations. *Earth and Planet Science Letters*, **268**, 165–170, doi:10.1016/j.epsl.2008.01.001.

SKAMAROCK, W. C., KLEMP, J. B., DUDHIA, J., GILL, D. O., BARKER, D. M., WANG, W., & POWERS, J. G. 2008 (01). *A Description of the Advance Research WRF Version 3*. NCAR Technical Note NCAR/TN-468+STR. National Center for Atmospheric Research, Boulder, Colorado, USA.

SKAMAROCK, WILLIAM C., & KLEMP, JOSEPH B. 2008. A time-split nonhydrostatic atmospheric model for weather research and forecasting applications. *Journal of Computational Physics*, **227**(7), 3465–3485, doi:10.1016/j.jcp.2007.01.037.

SOMBROEK, WIM. 2001. Spatial and Temporal Patterns of Amazon Rainfall. *AMBIO: A Journal of the Human Environment*, **30**(7), 388–396, doi:10.1639

SWENSON, SEAN, & WAHR, JOHN. 2006. Post-processing removal of correlated errors in GRACE data. *Geophys. Res. Lett.*, **33**, L08492, doi:10.1029/2005GL025285.

SWENSON, SEAN, WAHR, JOHN, & MILLY, P. C. D. 2003. Estimated accuracies of regional water storage variations inferred from the Gravity Recovery and Climate Experiment (GRACE). *Water Resour. Res.*, **39**(8), 1223, doi:10.1029/2002WR001808.

SYED, T. H., FAMIGLIETTI, J. S., CHEN, J., RODELL, M., SENEVIRATNE, S. I., VITERBO, P., & WILSON, C. R. 2005. Total basin discharge for the Amazon and Mississippi River basins from GRACE and a land-atmosphere water balance. *Geophys. Res. Lett.*, **32**, doi:10.1029/2005GL024851.

SYED, T. H., FAMIGLIETTI, J. S., ZLOTNICKI, V., & RODELL, M. 2007. Contemporary estimates of Pan-Arctic freshwater discharge from GRACE and reanalysis. *Geophys. Res. Lett.*, **34**, doi:10.1029/2007GL031254.

SYED, T. H., FAMIGLIETTI, JAMES S., & CHAMBERS, DON P. 2009. GRACE-Based Estimates of Terrestrial Freshwater Discharge from Basin to Continental Scales. *Journal of Hydrometeorology*, **10**(1), 22–40, doi:10.1175/2008JHM993.1.

TAPLEY, B. D., BETTADPUR, S., WATKINS, M., & REIGBER, C. 2004. The gravity recovery and climate experiment: Mission overview and early results. *Geophys. Res. Lett.*, **31**(May), L09607, doi:10.1029/2004GL019920.

TASCHETTO, ANDRÉA S., & ENGLAND, MATTHEW H. 2009. An analysis of late twentieth century trends in Australian rainfall. *International Journal of Climatology*, **29**(6), 791–807, doi:10.1002/joc.1736.

TAYLOR, KARL E. 2001. Summarizing multiple aspects of model performance in a single diagram. *J. Geophys. Res.*, **106**, 7183–7192, doi:10.1029/2000JD900719.

TRENBERTH, K. E. 1998. Atmospheric Moisture Recycling: Role of Advection and Local Evaporation. *Journal of Climate*, **12**, 1368–1381.

TRENBERTH, K. E., & GUILLEMOT, C. J. 1998. Evaluation of the atmospheric moisture and hydrological cycle in the NCEP/NCAR reanalyses. *Climate Dynamics*, **14**, 213–231, doi:10.1007/s003820050219.

TRENBERTH, K. E., SMITH, L., QIAN, T., DAI, A., & FASULLO, J. 2007. Estimates of the global water budget and its annual cycle using observational and model data. *J. Hydrometeor*, **8**, 758–769, doi:10.1175/JHM600.1. doi:10.1175/JHM600.1.

UPPALA, SAKARI, DEE, DICK, KOBAYASHI, SHINYA, BERRISFORD, PAUL, & SIMMONS, ADRIAN. 2008. Towards a climate data assimilation system: status update of ERA-Interim. *ECMWF Newsletter*, **115**, 12–18.

UPPALA, S.M., KALLBERG, P.W., SIMMONS, A.J., ANDRAE, U., DA COSTA BECHTOLD, V., FIORINO, M., GIBSON, J.K., HASELER, J., HERNANDEZ, A., KELLY, G.A., LI, X., ONOGI, K., SAARINEN, S., SOKKA, N., ALLAN, R.P., ANDERSSON, E., ARPE, K., BALMASEDA, M.A., BELJAARS, A.C.M., VAN DE BERG, L., BIDLOT, J., BORMANN, N., CAIRES, S., CHEVALLIER, F., DETHOF, A., DRAGOSAVAC, M., FISHER, M., FUENTES, M., HAGEMANN, S., HOLM, E., HOSKINS, B.J., ISAKSEN, L., JANSSEN, P.A.E.M., JENNE, R., MCNALLY, A.P., MAHFOUF, J-F., MORCRETTE, J-J., RAYNER, N.A., SAUNDERS, R.W., SIMON, P., STERL, A., TRENBERTH, K.E., UNTCH, A., VASILJEVIC, D., VITERBO, P., & WOOLLEN, J. 2005. The ERA-40 re-analysis. *Quart. J. Roy. Meteor. Soc.*, **131**, 2961–3012, doi:10.1256/qj.04.176.

WAHR, J., MOLENAAR, M., & BRYAN, F. 1998. Time variability of the Earth's gravity field: Hydrological and oceanic effects and their possible detection using GRACE. *J. Geophys. Res.*, **103**(B12), 30,205–30,229, doi:10.1029/98JB02844.

WANG, WEI, & SEAMAN, NELSON L. 1997. A Comparison Study of Convective Parameterization Schemes in a Mesoscale Model. *Month. Weather Rev.*, **125**(2), 252–278, doi:10.1175/1520-0493(1997)125<0252:ACSOCP>2.0.CO;2.

WANG, WEI, BRUYERE, CINDY, DUDA, MICHAEL, DUDHIA, JIMY, GILL, DAVE, LIN, HUI-CHUAN, MICHALAKES, JOHN, RIZVI, SYED, & ZHANG, XIN. 2009 (04). *WRF ARW Version 3 Modeling System User's Guide, April 2009*. National Center for Atmospheric Research (NCAR).

WATKINS, MICHAEL, & YUAN, DAH-NING. 2007. *JPL Level-2 Processing Standards Document for Product Release 04*. Technical information. Jet Propulsion Laboratory, NASA. `http://isdc.gfz-potsdam.de/`, visited 2010/01/27.

WERTH, DAVID, & AVISSAR, RONI. 2004. The Regional Evapotranspiration of the Amazon. *Journal of Hydrometeorology*, **5**(1), 100–109, doi:10.1175/1525-7541(2004)005<0100:TREOTA>2.0.CO;2.

YU, ZHONGBO, POLLARD, DAVID, & CHENG, LI. 2006. On continental-scale hydrologic simulations with a coupled hydrologic model. *Journal of Hydrology*, **331**(1-2), 110–124, doi:10.1016/j.jhydrol.2006.05.021.

A

Regional Simulations Overview

Table A.1 gives an overview on the simulations performed with the regional atmospheric model WRF. The first column depicts the short name that is derived from the setup of the model. These names are used for the data storage directory tree. The second column shows the simulation period. SST, cumulus and FDDA represent the physics that were selected in a regional atmospheric simulation. The last column contains the type of driving data for a run. Table A.2 lists the output variable that are stored for each regional simulations.

Table A.1.: Regional simulations, model runs for different domains (**Ama**zon, **Sah**ara, **Sib**eria, **Aus**tralia) and different model configurations.

Domain & setup	Stretch	SST	Cumulus	FDDA	Driving
amaEI	2001-01 – 2005-12	constant	Kain-Fritsch	no	EI
amaEIsst	2001-01 – 2007-01	variant	Kain-Fritsch	no	EI
amaEIsstKFfdda	2001-01 – 2006-12	variant	Kain-Fritsch	yes	EI
amaEIsstBMJ	2001-01 – 2006-12	variant	Betts-Miller-Janjic	no	EI
amaEIsstBMJfdda	2001-01 – 2002-12	variant	Betts-Miller-Janjic	yes	EI
amaEIsstBMJfddaMOIST	2001-01 – 2001-12	variant	Betts-Miller-Janjic	moist	EI
amaEIsstBMJfddaTEMP	2001-01 – 2001-12	variant	Betts-Miller-Janjic	temp	EI
amaEIsstBMJfddaWIND	2001-01 – 2001-12	variant	Betts-Miller-Janjic	wind	EI
amaNNRP	2001-01 – 2006-12	constant	Kain-Fritsch	no	NNRP
amaNNRPsst	2001-01 – 2007-12	variant	Kain-Fritsch	no	NNRP
amaNNRPsstKFfdda	2001-01 – 2007-12	variant	Kain-Fritsch	yes	NNRP
amaNNRPsstBMJ	2001-01 – 2007-12	variant	Betts-Miller-Janjic	no	NNRP
sahExtEIsst	2001-01 – 2007-01	variant	Kain-Fritsch	no	EI
sahExtEIsstKFfdda	2001-01 – 2007-01	variant	Kain-Fritsch	yes	EI
sahExtEIsstKFfddaALB	2004-01 – 2004-12	variant	Kain-Fritsch	yes	EI
sahExtEIsstBMJ	2002-01 – 2006 12	variant	Betts-Miller-Janjic	no	EI
sahExtEIsstBMJfdda	2002-01 – 2002 02	variant	Betts-Miller-Janjic	yes	EI
sahNNRP	2001-01 – 2006-12	constant	Kain-Fritsch	no	NNRP
sahExtNNRPsst	2001-01 – 2007-01	variant	Kain-Fritsch	no	NNRP
sahExtNNRPsstKFFdda	2001-01 – 2007-01	variant	Kain-Fritsch	no	NNRP
sahExtNNRPsstBMJ	2001-01 – 2006-12	variant	Betts-Miller-Janjic	no	NNRP
sibEI	2001-05 – 2007-01	constant	Kain-Fritsch	no	EI
sibEIsst	2001-05 – 2007-01	variant	Kain-Fritsch	no	EI
sibEIsstKFfdda	2001-05 – 2007-01	variant	Kain-Fritsch	yes	EI
sibNNRP	2001-01 – 2007-12	constant	Kain-Fritsch	no	NNRP
sibNNRPsst	2001-05 – 2007-01	variant	Kain-Fritsch	no	NNRP
sibExtNNRPsstKFFdda	2001-05 – 2007-01	variant	Kain-Fritsch	yes	NNRP
ausEIsst	2001-01 – 2006-12	variant	Kain-Fritsch	no	EI
ausEIsstKFfdda	2001-01 – 2006-12	variant	Kain-Fritsch	yes	EI
ausEIsstBMJ	2001-01 – 2006 12	variant	Betts-Miller-Janjic	no	EI
ausNNRPsst	2001-01 – 2006-12	variant	Kain-Fritsch	no	EI
ausNNRPsstKFfdda	2001-01 – 2006-12	variant	Kain-Fritsch	yes	EI
ausNNRPsstBMJ	2001-01 – 2006 12	variant	Betts-Miller-Janjic	no	NNRP

Table A.2.: Regional model (WRF-ARW) – recorded variables. x=west–east, y=north–south, z=bottom–top, t=time, cumulative = 6-hourly sum, continuous = instantaneous field

Field name	WRF name	Dims	Unit	Mode	File prefix
potential evaporation	POTEVP	xyt	W m^{-2}	cumulative	hydrology
soil water content	SH2O	xyzt	m^3 m^{-3}	instantaneous	hydrology
total soil moisture	SMSTOT	xyt	m^3m^{-3}	instantaneous	hydrology
surface runoff	SFROFF	xyt	mm	cumulative	hydrology
base runoff	UDROFF	xyt	mm	cumulative	hydrology
actual evaporation	SFCEVP	xyt	mm	cumulative	hydrology
snow mass	SNOW	xyt	kg m^{-2}	instantaneous	hydrology
canopy water	CANWAT	xyt	kg m^{-2}	instantaneous	hydrology
convective precipitation	RAINC	xyt	mm	cumulative	hydrology
non conv. precipitation	RAINNC	xyt	mm	cumulative	hydrology
non conv. snowfall	SNOWNC	xyt	mm	cumulative	hydrology
non conv. graupel	GRAUPELNC	xyt	mm	cumulative	hydrology
vertical level height	RDZW	xyzt	m^{-1}	instantaneous	grid
moisture flux divergence	VIMFD	xyt	kg m^{-2} s^{-1}	instantaneous	mfdiv
moisture flux divergence	CIMFD	xyt	kg m^{-2} s^{-1}	cumulative	mfidv
west-east wind	U	xyzt	m s^{-1}	instantaneous	energy
south-north wind	V	xyzt	m s^{-1}	instantaneous	energy
bottom-top wind	W	xyzt	m s^{-1}	instantaneous	energy
heat flux	HFX	xyt	W m^{-2}	instantaneous	energy
upward moisture flux at the surface	QFX	xyt	kg m^{-2} s^{-1}	instantaneous	energy
latent heat flux	LH	xyt	W m^{-2}	instantaneous	energy
ac. upw. heat flux at the sfc.	ACHFX	xyt	W m^{-2}	instantaneous	energy
ac. upw. latent heat flux at the sfc.	ACLHF	xyt	W m^{-2}	instantaneous	energy
pertubation dry air mass in column	MU	xyt	Pa	instantaneous	pressure
base state dry air mass in column	MUB	xyt	Pa	instantaneous	pressure
inverse dry air density	ALT	xyzt	m^3 kg^{-1}	instantaneous	pressure
2m temperature	T2	xyt	K	instantaneous	pressure
2m potential temperature	TH2	xyt	K	instantaneous	pressure
surface pressure	PSFC	xyz	Pa	instantaneous	pressure
specific humidity vapor	QVAPOR	xyzt	kg kg^{-1}	instantaneous	pressure
specific humidity clouds	QCLOUD	xyzt	kg kg^{-1}	instantaneous	pressure
specific humidity rain	QRAIN	xyzt	kg kg^{-1}	instantaneous	pressure
specific humidity ice	QICE	xyzt	kg kg^{-1}	instantaneous	pressure
specific humidity snow	QSNOW	xyzt	kg kg^{-1}	instantaneous	pressure
model top pressure	P_TOP	t	Pa	constant	pressure

B

Study Regions Overview

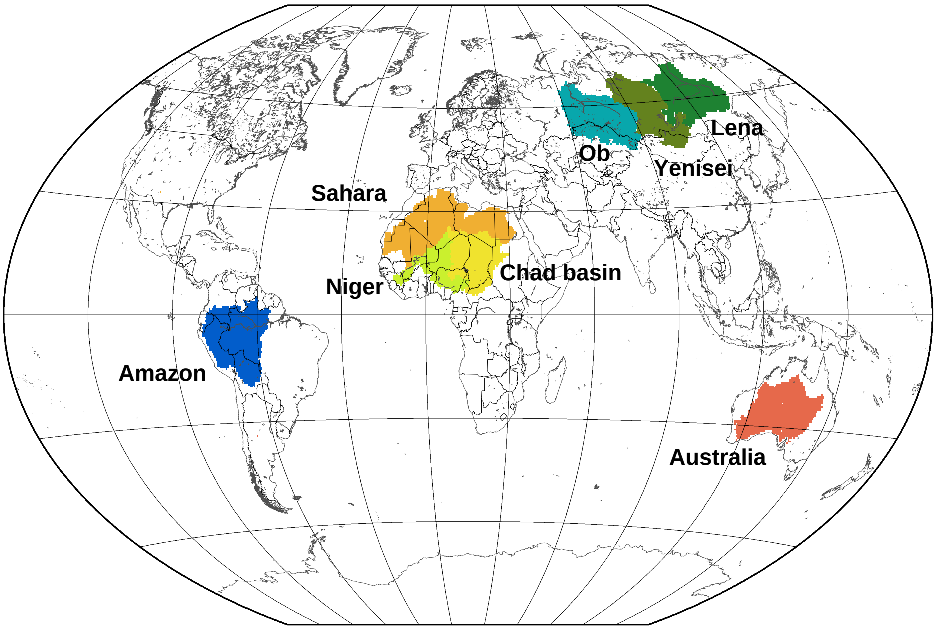

Figure B.1.: Global distribution of the selected study domains.

Figure B.1 illustrates the global distribution of the study regions. The hydrological basins were selected according to the criteria size and availability of discharge data. The minimum size was defined with 1,000,000 km^2. With regard to the GRACE mission, discharge data is mandatory for the period 2003-2007. Table B.1 lists the basins and their properties for the different regional model domains.

Table B.1.: Runoff data available from the Global Runoff Data Center. Catchments with sufficient size and available discharge data are marked green and are selected for the comparison with the GRACE solutions. For comparison: one derived GRACE pixel has a resolution of about $160,000\,\text{km}^2$

Domain	**Basin**	**Area (km^2)**	**Discharge Data**	**Database ID**
Amazonian domain				
	Amazon River	4,672,876	1975 - 2007	295
Australian domain				
	Australian Plane	3,880,436	zero discharge	357/367
	Murray	1,022,767	1985 - 2000	383
	Burdekin	132,686	1975 - 2000	369
	Fitzroy (east)	126,986	1975 - 2001	377
Saharan domain				
	Sahara basin	5,271,752	zero discharge	192/228
	Lake Chad	3,180,752	zero discharge	235
	Nile	3,050,401	no data	229
	Niger	2,100,508	1975 - 2006	241
	Senegal River	417,107	no data	256
	Volta	403,975	no data	263
	Euphrates	328,298	no data	173
Siberian domain				
	Ob	2,926,321	1975 - 2007	35
	Yenisei	2,454,961	1975 - 2007	12
	Lena	2,417,932	1975 - 2007	6
	Kathanga	265,581	1975 - 1994	3
	Yana	220,949	1975 - 2007	7
	Olenek	199,723	1975 - 2003	5
	Taz	126,775	1975 - 1996	36

Table B.2.: Overview on the 10 largest study regions. These are used for the analysis of the inter-variability of the three different GRACE solutions. All considered areas are larger than 2,000,000 km^2.

Region	**Area (km^2)**	**Region**	**Area (km^2)**
Lena	2,417,932	Saudi Arabian desert	2,398,132
Yenisei	2,454,961	Northern Sahara	3,466,292
Ob	2,926,321	Lake Chad	3,180,752
Kaspian Sea	2,159,436	Amazon	4,672,876
Gobi desert	2,099,470	Western Australian Basin	2,036,603

C

Data Processing

Computation of Monthly Moisture Convergence Fields

According to (Barry, 1968; Palmén & Holopainen, 1962), in a geographic coordinate system, the horizontal divergence of moisture flux is computed with

$$\nabla_h \cdot \underbrace{v_h\, q}_{\substack{\text{horizontal}\\ \text{moisture flux}}} = \frac{\partial(uq)}{\partial x} + \frac{\partial(vq)}{\partial y} - \underbrace{\frac{vq\tan\phi}{R}}_{\substack{\text{correction for}\\ \text{meridian convergence}}} \tag{C.1}$$

∇_h denotes the horizontal divergence operator ($1/m$), v_h the horizontal wind vector (m/s), and q the specific humidity (kg/kg). The third term of equation C.1 accounts for the meridian convergence at a certain latitude ϕ. R depicts the radius of the earth (m).

In order to obtain an equivalent rate for $P-E$, the vertical integral of $\nabla_h \cdot v_h q$ is considered. If air pressure p (Pa) is deployed for the vertical coordinate the moisture convergence for a point is defined with

$$-\nabla \cdot \vec{Q} \equiv -\frac{1}{g}\nabla \cdot \int_{p=0}^{p=p_{sfc}} \vec{v}_h\, q\, dp \tag{C.2}$$

$\vec{Q}$ represents the vertical integral of moisture flux (kg/ms), g the gravity acceleration of the earth (m/s^2). Finally, $-\nabla \cdot \vec{Q}$ yields the convergence (or negative divergence) of the vertical integral of horizontal moisture flux (kg/m^2s).

NCAR/NCEP reanalysis NCAR/NCEP provides on-line data access to its NNRP. Typically, global fields can be obtained for a number of different pressure levels and for the surface layer. Data on model levels is available with higher detail but only available on special request and implies shipping with physical storage devices. Hence, the six-hourly fields on pressure levels are taken for the computation of $-\nabla \cdot \vec{Q}$ (and also for the driving of the regional atmospheric model). Instead of specific humidity, only relative humidity is obtainable. Therefore, other variables are needed for a conversion. The list of variables comprises east-west (u) and north-south (v) wind, temperature (T) in Kelvin, relative humidity (φ), and surface elevation (h) for a height correction of the vertical integration.

Table C.1.: Available pressure levels for NNRP variables

Variable	Pressure	levels	(hPa)						
u,v,T	1000	925	850	700	600	500	400	300	250
		200	150	100	70	50	30	20	10
φ	1000	925	850	700	600	500	400	300	

As shown in table C, relative humidity data is only archived for the lowest eight pressure layers of the atmosphere. Thus, the computation only accounts for this subset. Processes above 250 hPa are neglected. For the computation of $-\nabla \cdot \vec{Q}$ this is not problematic as the moisture content in the upper atmospheric layers is usually negligible.

The NNRP data contains only the relative humidity. Relative (φ) and specific (q) humidity can be converted by the use of the vapor pressure (e). φ is defined as the ratio of the vapor pressure with the saturation vapor pressure (e_s)

$$\varphi = \frac{e}{e_s} \tag{C.3}$$

The specific humidity is defined with

$$q = \frac{\frac{R_a}{R_v}\, e}{p - (1 - \frac{R_a}{R_v})\, e} \tag{C.4}$$

with R_a and R_v denoting the gas constants of dry air 287.0587 $J\,kg^{-1}\,K^{-1}$ and of water vapor 461.525 $J\,kg^{-1}\,K^{-1}$, respectively. p is the air pressure in units of Pa. In order to solve equation C.3 for the vapor pressure e, the saturation vapor pressure must be known. e_s is known to vary with temperature and thus with height. This relationship can be approximated with the Clausius Clapeyron Equation. The saturation vapor pressure of water over a liquid (and not icy) surface is given by

$$e_s = e_{s0}\ \exp\left[\frac{A_h}{R_v}\left(\frac{1}{T_0} - \frac{1}{T}\right) + \frac{B_h}{R_v}\ \ln\left(\frac{T_0}{T}\right)\right]. \tag{C.5}$$

e_{s0} is the known saturation vapor pressure at temperature T_0. A_h and B_h are constants with respective values of $3.1483910^6\ J/kg$ and $2370\,Jkg^{-1}K^{-1}$ (Jacobson, 1999).

As illustrated in figure C.1, the horizontal components of the moisture flux are computed at the respective edges with adjacent cells. This gives the fluxes in the four cardinal directions. With positive sign, the fluxes are orientated from west to east and from north to south, respectively.

$$\overline{qu_E} = \frac{qu_{x,y} + qu_{x-1,y}}{2}$$
$$\overline{qu_W} = \frac{qu_{x,y} + qu_{x+1,y}}{2}$$
$$\overline{qv_N} = \frac{qv_{x,y} + qv_{x,y+1}}{2}$$
$$\overline{qv_S} = \frac{qv_{x,y} + qv_{x,y-1}}{2}$$

The grid cells close to the poles are not considered as this information is not needed within this study. For the discrete mesh, the convergence is determined with

$$\nabla \cdot \vec{q} = \frac{qu_E - qu_W}{dy} + \frac{qv_S - qv_N}{dx} - \frac{0.5(qv_S + qv_N)\tan\phi}{R}. \tag{C.6}$$

For the NCAR/NCEP data, the meridional wind is defined from north to south. The correction for meridian convergence is given by the third term of equation C.6.

The vertical integration is done by summing up the different pressure weighted levels. For an arbitrary grid cell the vertical sum is obtained with

$$-\nabla \cdot \vec{Q} = -\sum_{k=p_{sfc}}^{k=p_0} \nabla \cdot \vec{q}(k)\, \frac{p_k - p_{k-1}}{g}\, c \qquad c = \begin{cases} 0 & \text{if } p < p_b \\ 1 & \text{if } p \geq p_b \end{cases} \tag{C.7}$$

The gravity acceleration (g) is assumed constant for all layers, with 9.81 m/s^2. Pressure layer that are below the normal pressure (p_b) of the surface elevation are neglected. The normal pressure is assessed with

$$p_b = 1013 - 1.23gh0.01 \tag{C.8}$$

with h denoting the terrain elevation in m;

The monthly mean fields for the computation of $-\nabla \cdot \vec{Q}$ are derived from the six-hourly NNRP data with the Climate Data Operators (CDO) from Max-Plank Institute, Hamburg.

ECMWF ERA-INTERIM reanalysis For the ECMWF ERA-INTERIM reanalysis, readily computed fields of $\nabla \cdot \vec{Q}$ are obtained from the *ecaccess* system. For every month the fields consist of four synoptic times, 00, 06,12, and 18 hours of GMT. The final monthly data sets are averaged and interpolated from 0.75 °× 0.75 ° to a 0.5 °× 0.5 ° mesh, using the CDO toolbox.

Regional atmospheric model WRF For the regional atmospheric model, the computation of $-\nabla \cdot \vec{Q}$ is realized similarly to the NNRP approach. Different to the NNRP reanalysis, the wind fields are available on a staggered grid. Therefore, only the specific humidity is derived as

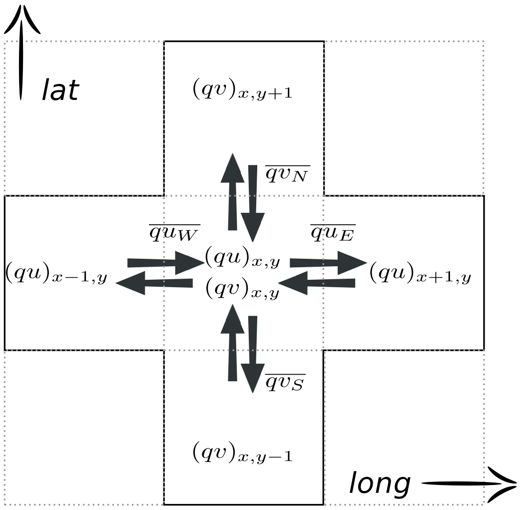

Figure C.1.: Computation of the west-east and north-south moisture flux components from specific humidity and wind(u, v) for a horizontal pressure layer.

two cell mean between adjacent cells. With WRF, the vertical integration is performed along a metric z-coordinate. Therefore, equation C.2 changes to

$$-\nabla \cdot \vec{Q} = -\nabla \int_{z=z_{top}}^{z=z_{sfc}} v_h \rho q \, dz \tag{C.9}$$

with ρ describing the dry air density in kg/m^3. The regional model uses an equidistant geographic projection. Therefore, no correction term for meridian convergence is necessary. The vertically integrated moisture flux convergence is archived as six-hourly instantaneous and temporal aggregated field. The catchment averaged time-series are prepared from monthly means.

Lebenslauf

Benjamin Fersch	geboren 19.08.1980 in Dachau
Juni 2000	Abitur, Viscardigymnasium Fürstenfeldbruck
2001-2007	Studium Hydrologie, Universität Freiburg im Breisgau
Januar 2007	Diplom Hydrologie Thema der Diplomarbeit: “Wechselwirkung von Galeriwäldern und alluvialen Aquiferen”
Seit Februar 2007	Wissenschaftlicher Mitarbeiter am Karlsruher Institut für Technologie (KIT), Institut für Meteorologie und Klimaforschung (IMK-IFU), Garmisch-Partenkirchen